Effect of Cellulose Nanocrystals on the Rheology, Curing Behavior, and Fracture Performance of Phenol-Formaldehyde Resol Resin

Jung Ki Hong

Thesis submitted to the faculty of the
Virginia Polytechnic Institute and State University
in partial fulfillment of the requirements for the degree of

Master of Science
In
Forest Products

Maren Roman, Chair
Charles E. Frazier
Scott H. Renneckar

November 17, 2009
Blacksburg, VA

Keywords: cellulose nanocrystals, phenol formaldehyde resin, rheology, viscosity, differential scanning calorimetry, dynamic mechanical analysis, fracture testing

Effect of Cellulose Nanocrystals on the Rheology, Curing Behavior, and Fracture Performance of Phenol-Formaldehyde Resol Resin

Jung Ki Hong

ABSTRACT

The purpose of this research was to determine the effects of cellulose nanocrystals (CNCs), as potential additives, on the properties and performance of phenol–formaldehyde (PF) adhesive resin. The steady-state viscosity of a commercial PF resol resin and three CNC–resin mixtures, containing 1–3 wt % CNCs, based on solids content, was measured with a rheometer as a function of shear rate. The viscosity of the PF resin itself was independent of shear rate. The viscosity–shear rate curves of the CNC–resin mixtures showed two regions, a shear thinning region at lower shear rates and a Newtonian region at higher shear rates. The low-shear-rate viscosity of the resin was greatly increased by the CNCs. The structure of the CNC–resin mixtures under quiescent conditions was analyzed by polarized light microscopy. The mixtures contained CNC aggregates, which could be disrupted by ultrasound treatment. The curing progressions of the resin and CNC–resin mixtures were analyzed by non-isothermal differential scanning calorimetry (DSC). The DSC curves showed two exotherms followed by an endotherm. The energy of activation for the first exotherm was reduced by the CNCs whereas the energy of activation for the second exotherm was not affected by the CNCs. Increasing CNC contents caused higher degrees of reaction conversion during the first curing stage and a greater loss of sample mass, attributed to formaldehyde release during resin cure. For analysis of the mechanical properties during and after cure, sandwich-type test specimens were prepared from southern yellow pine strips and the resin and CNC–resin mixtures. The mechanical properties of the test specimens were measured as a function of time and temperature by dynamic mechanical analysis (DMA). The time to incipient storage modulus increase decreased and the rate of relative storage modulus increase increased with increasing CNC content. The ultimate sample stiffness increased with increasing CNC content for CNC contents between 0 and 2 wt %, which was attributed to

mechanical reinforcement of the resin by the CNCs. At a CNC content of 3 wt %, the ultimate sample stiffness was lower than at a CNC content of 2 wt % and the second tan δ maximum occurred earlier in the experiment, indicating an earlier onset of vitrification. The lower ultimate sample stiffness was attributed to premature quenching of the curing reactions through CNC-induced depression of the vitrification point. For analysis of the fracture performanc, double cantilever beam test specimens were prepared from southern yellow pine beams and the resin and CNC–resin mixtures, using different hot-pressing times. Fracture energies were measured by mode I cleavage tests. Bondline characteristics were analyzed by light microscopy. At a hot-pressing time of 10 min, the fracture energy decreased with increasing CNC content, whereas it stayed constant for CNC contents between 1 and 3 wt % at a hot-pressing time of 8 min. The bondlines of resin mixtures containing CNCs exhibited voids, whereas those of the pure resin did not. CNCs had both benefitial and detrimental effects on the properties and performace of PF resin.

ACKNOWLEDGMENTS

First of all, I would like to express profound gratitude to my advisor, Dr. Maren Roman. Her patience, trust, and encouragement became a cornerstone for me in troubled times during the completion of this work. Undoubtedly, without her contribution and guidance, this work would not be finished. I would also like to express sincere gratitude to my committee members, Dr. Charles E. Frazier and Dr. Scott Renneckar. Dr. Frazier has provided me with scientific guidance and encouragement. His rich experience and deep insight cannot be compared with any textbook. I am grateful for discussions with Dr. Renneckar and for his kind advice on this work. Furthermore, I would like to thank Dr. Kevin Edgar and Dr. Audrey Zink-Sharp for assisting and sharing their knowledge and facilities. Their continuous support enabled me to complete this work successfully. I cannot help but admire their enthusiasm for academic development.

I would like to thank my fellow graduate students and group members for their help and invaluable discussions during this study. The appreciations are extended to the staffs in the Department of Wood Science and Forest Products, Linda Caudill, Rick Caudill, David Jones, Kenneth Albert, Debbie Garnand, and Angela Riegel, for their kind assistance.

This project was funded in part through the Wood-Based Composites Center (WBC) at Virginia Tech. I would like to express my appreciation to the Center. It has been a great pleasure to be a WBC fellow. The project was furthermore supported in part by the Sustainable Engineered Materials Institute, USDA/CSREES under Grant No. 2005-35504-16088, and by the U.S. Department of Transportation in combination with the Southeastern Sun Grant Center, for which I am also grateful. Support in form of material donations by Dynea North America, now Arclin (Dr. Bruce Broline) and Tembec, Inc. (Dr. Derek Budgell) for this study are also gratefully acknowledged.

Last but not least, this work is dedicated to my family. Their everlasting love, support and sacrifice became the driving force in my life.

TABLE OF CONTENTS

LIST OF FIGURES

Chapter 2

Chapter 3

Chapter 4

Chapter 5

Chapter 6

LIST OF TABLES

Chapter 6

CHAPTER 1

INTRODUCTION

An ever-increasing demand for forest products is challenging related industries to raise the utilization efficiency of raw materials under the constraints of limited natural resources and environmental preservation. Wood-based composites are among the most important products of today's forest products industry because they can not only enhance the utilization of timber resources but also offer several advantages over solid wood. Thus, constant efforts to improve manufacturing processes and the performance of wood-based composites has led to remarkable advances over the past decades. Progress in the area of wood-based composites depends on the cutting edge of adhesive technology because wood adhesives play a critical role in achieving the desired properties of wood-based composites. For example, phenol–formaldehyde (PF) resins have been extensively used as exterior-grade wood adhesives since the early 1900's because of their high rigidity, durability, chemical resistance, and dimensional stability. Despite unremitting efforts to develop the performance and quality of existing adhesives, further improvements in various aspects are still needed in order to meet the requirements of contemporary technologies.

In recent years, nanotechnology has attracted tremendous attention and its applications are being studied in various fields. Since the advent of nanotechnology, existing adhesives and potential methods for their improvement are considered from a new perspective. Moreover, along with nanotechnology, renewable natural resources have regained interest by academia and industry. For instance, nanoparticles of cellulose, termed cellulose nanocrystals (CNCs), have a broad range of potential applications by

virtue of their unique properties, such as low cost, compared to other nanoparticles, biodegradability, lack of toxicity, and ease of topochemical modification. The goal of this research is to evaluate CNCs as potential performance-enhancing additives for PF wood adhesive resins. CNCs are promising candidates as PF resin additives because cellulose, the main component of wood, is commonly believed to catalyze resin cure. In addition to potentially discovering a new PF resin additive, the research has the potential to contribute to our understanding of the effect of cellulose on the cure and properties of PF wood adhesive resins. The specific objectives of this research are to:

1. Determine the effects of CNCs on the liquid-state properties of PF resins, in particular resin rheology;
2. Determine the effects of CNCs on the cure kinetics of PF resins;
3. Determine the effects of CNCs on the mechanical properties of PF resins during and after cure; and
4. Determine the effects of CNCs on the fracture performance of PF resins.

The research results are reported in four chapters, namely Chapters 3 through 6, written in manuscript format. Chapter 2 reviews the relevant literature and Chapter 7 presents the overall conclusions.

CHAPTER 2

LITERATURE REVIEW

2.1. PHENOL–FORMALDEHYDE ADHESIVE RESINS

Phenol–formaldehyde (PF) resin, the first synthetic polymer, is one of the most widely used thermosetting resins. Since its commercialization in the early 1900's by Dr. Leo Baekeland, PF resin has played a vital role in various industries, including the construction, automotive, electrical, and appliance industries, by virtue of its versatility [1-4].

Based on the type of catalyst and the formaldehyde (F) to phenol (P) molar ratio, PF resins can be divided into two classes, resols and novolaks. Resols are formulated with an excess of formaldehyde ($F/P > 1$) under alkali-catalyzed condition. On the other hand, novolaks are formulated with an excess of phenol ($F/P < 1$) under acid-catalyzed condition. The properties of the PF resins are determined by several parameters, including the F/P molar ratio, type of catalyst, reaction time and temperature, water content, and the type and amount of other additives [2].

The main application of PF resol resins is as exterior-grade wood binder in wood-based composites, such as plywood, oriented strandboard (OSB), fiberboard, and engineered lumber products [5]. In 2002, approximately 27% of the total 2 million metric tons of PF resin solids were consumed by the North American wood composites industry [6]. For exterior-grade wood-based composites, resols are the preferred adhesive resin because they endow high rigidity, durability, chemical resistance, and dimensional stability. In addition, resols are a soluble adhesive with good wetting properties on wood substrates [7, 8].

2.1.1. Cure chemistry

Generally, PF resol resins for wood-based composites are synthesized with an F/P molar ratio of 1.6–2.5 at a pH of 9–12 and at temperatures below 100 °C [9, 10]. As alkali catalyst, sodium hydroxide is most commonly used for the synthesis of PF resol resins. In addition, commercial PF resols usually contain 10–20 wt % post-added urea based on the resin solids [9-11]. The addition of urea is common in the manufacture of commercial OSB PF resols because urea not only reduces the resin cost but also scavenges free formaldehyde monomer. Also, urea improves flow properties, accelerates cure of the resin during hot pressing, and enhances functionality of the resin [9, 12].

The cure of the PF resol resins proceeds via step-growth polymerization by means of heating under alkaline condition, leading to insoluble and infusible, three dimensionally-crosslinked polymer networks. The reaction sequence for resol synthesis can be divided into three steps: addition of formaldehyde to phenol, chain growth or prepolymer formation, and crosslinking or curing of the prepolymer. Phenols are highly reactive under alkaline conditions and readily form phenoxide ions, which are resonance stabilized, as shown in Figure 2.1.

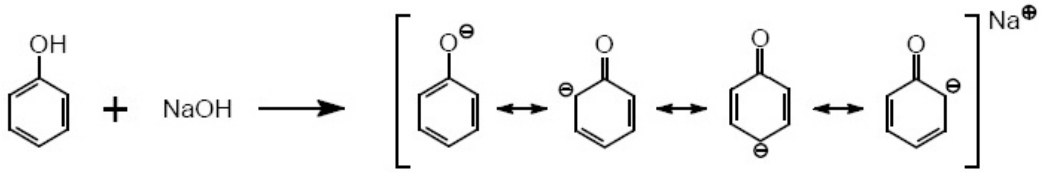

Figure 2.1. Formation and resonance stabilization of phenoxide ions under alkaline conditions.

Formaldehyde addition occurs via electrophilic attack [13] of the tri-functional phenoxide ion by formaldehyde, present as methylene glycol in aqueous solutions, in the ortho or para position [14, 15]. As illustrated in Figure 2.2, substitution of the ortho or para hydrogen atom under elimination of water yields 2- and 4-hydroxymethylphenols (HMPs), respectively. Subsequent attack on the remaining active sites gives di- and tri-substituted HMPs.

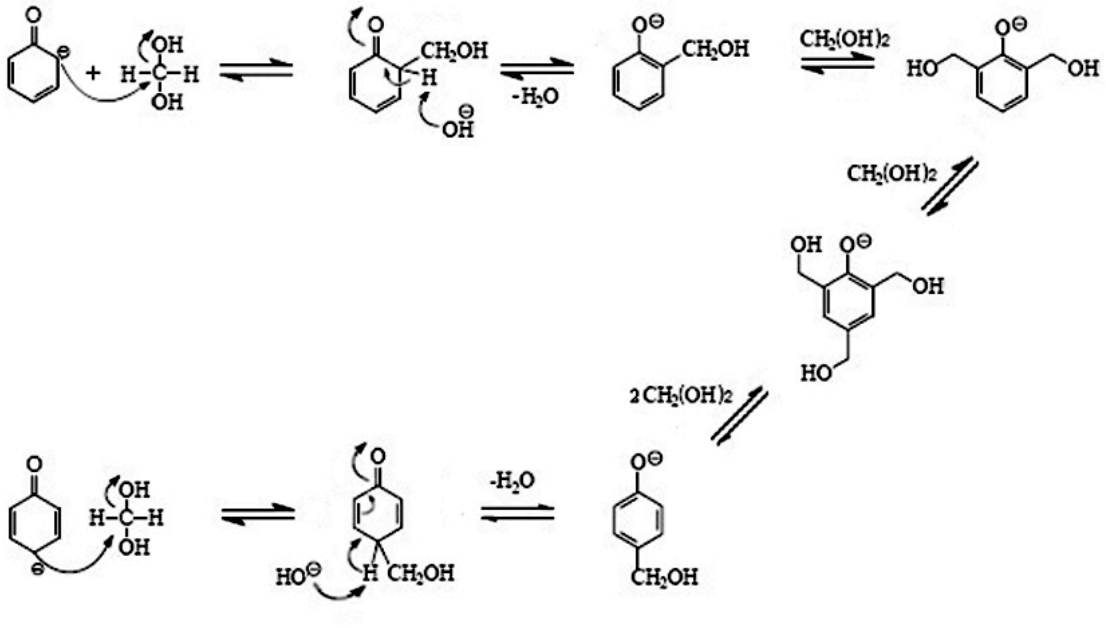

Figure 2.2. Formation of mono-, di- and tri-substituted hydroxymethylphenols in addition reactions.

After HMP formation, condensation reactions among the HMPs result in chain growth and finally crosslinking. As shown in Figure 2.3, the condensation of HMPs proceeds by means of quinone methide intermediates, which are strong electrophiles and react with active ortho or para hydrogens of nearby mono- and di-substituted HMPs to form methylene bridges under elimination of water [13, 16, 17].

Based on research by Baekeland and Lebach [18, 19], three HMP condensation stages can be distinguished: resole, resitol, and resite. The A stage (resole) represents an early stage during condensation, characterized by HMP monomers and dimers. The B stage (resitol) is characterized by a higher degree of condensation and some crosslinking. Commercial PF resols used for the wood-based composites are typically condensed to the resitol stage with the exact molecular weights and distributions depending on the application of the resol. At the C stage (resite), resols are highly crosslinked and comprise infusible and insoluble, three-dimensional molecular networks.

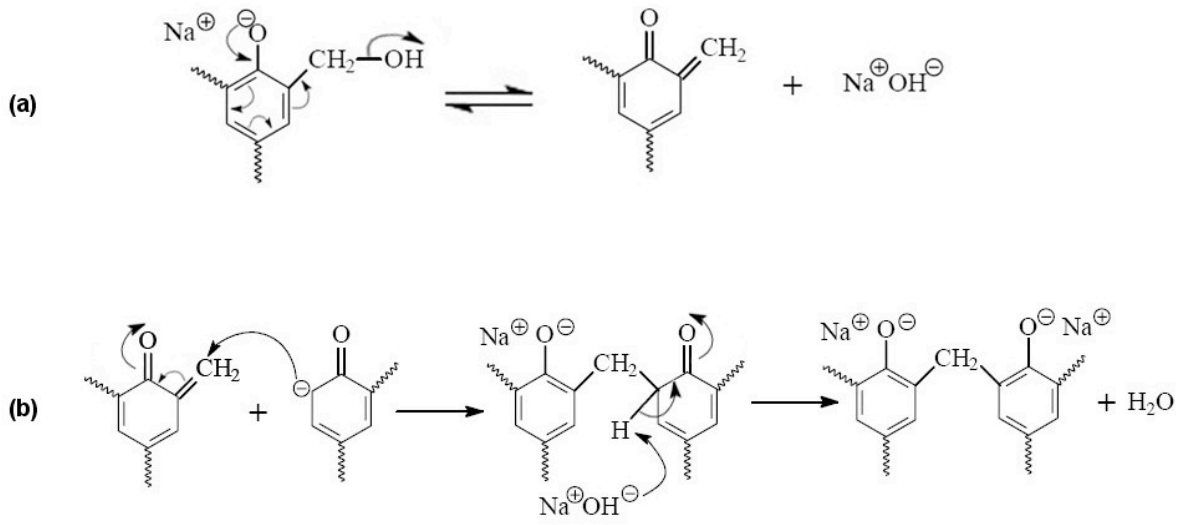

Figure 2.3. Formation of quinine methide intermediates (a) and formation of methylene bridges via quinine methide intermediates (b) during hydroxymethylphenol condensation reactions. (Reprinted from ref 17; fair use; Copyright 1946 John Wiley & Sons, Ltd)

2.1.2. Effect of wood/cellulose on cure kinetics

The curing behavior of PF resol resins in the manufacture of wood-based composite differs from that observed under laboratory conditions. Additional crosslinking mechanisms not observed in laboratory test methods have been proposed, such as the formation of ether bridges between phenoxide ions and HMPs (Figure 2.4(a)), crosslinking between methylene bridges by free formaldehyde (Figure 2.4(b)), and condensation reactions between methylene carbons and HMPs (Figure 2.4(c)) [20, 21].

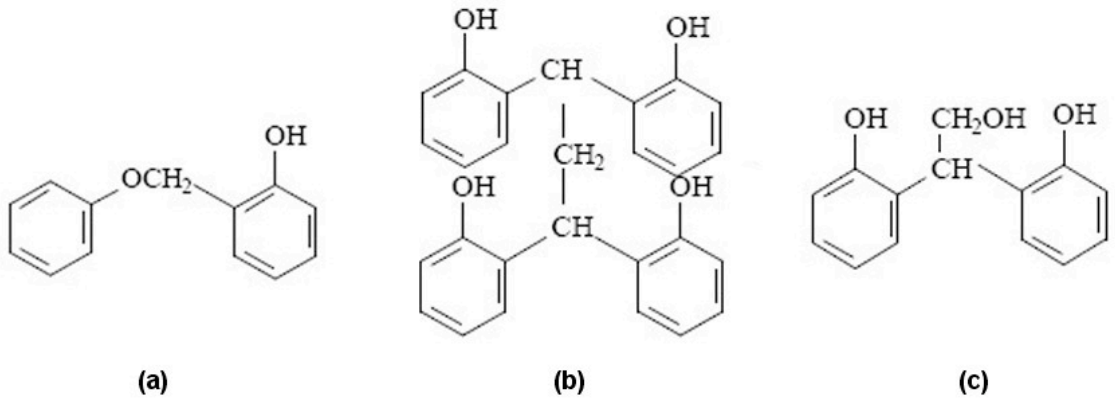

Figure 2.4. Proposed unusual crosslink structures formed in the curing reactions of PF resols. (Reprinted from ref 21; fair use; Copyright 1984 American Chemical Society)

In addition, it is well established that the adhesion of PF resins to wood substrates is not due to covalent bonds between the resin and the substrate but to hydrogen bonds and secondary intermolecular interactions [15, 22-24]. Regarding wood-based composites manufacturing conditions, covalent bonding between PF resins and wood is negligible because covalent bonding occurs at significantly higher temperatures and longer cure times than generally used in wood-based composites manufacturing [15, 25].

Many research efforts have been made to elucidate the effects of wood on the curing behavior of PF resins because those effects translate directly to the manufacture and properties of wood-based composites [26-32]. The interaction between wood and PF resins complicates the curing process. As a result, and because of the complex nature of wood, conflicting research results have been reported.

It is generally accepted that the cure kinetics and hardening process of PF resins are influenced by the presence of wood [27]. Wood has been shown to have catalytic activity and to lower the activation energy of the polycondensation reactions [28, 29, 33, 34]. In other words, resin polymerization and crosslinking occur faster in the presence of wood than in its absence. Some studies, on the other hand, have shown that certain wood species retard the curing reactions through their acidity by lowering the pH of the resin and thereby increasing the activation energy of the polycondensation reactions [27, 31].

Other studies have indicated that the wood carbohydrates, such as cellulose and hemicellulose, are responsible for the decrease in activation energy caused by wood, provided that the resin has molecular contact with the wood substrate [35]. Chemical reactions between the PF resin and the wood substrate have not been observed, but secondary interactions, such as hydrogen bonding and van der Waals forces, have been detected [31] and have been proposed to be responsible for the catalytic activity of wood. Figure 2.5. shows potential hydrogen bonds between a cellulose molecule and PF resin [8].

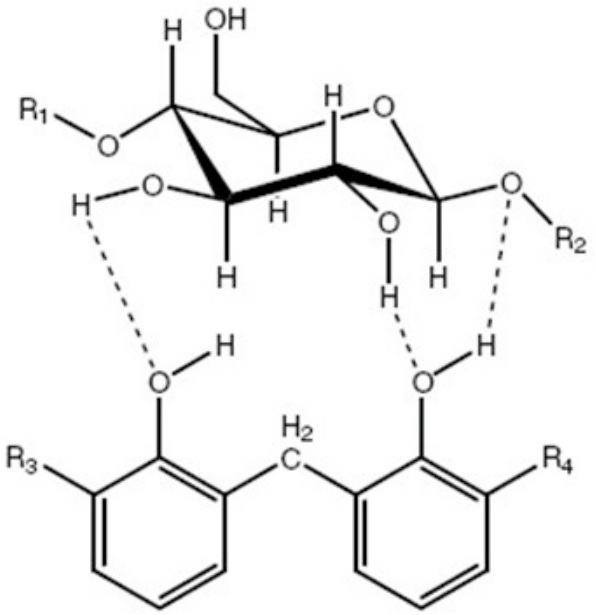

Figure 2.5. Hydrogen bonds between a cellulosic segment and a phenol-formaldehyde polymer. (Reprinted from ref 8; fair use; Copyright 2005 CRC Press)

With respect to the formation of hydrogen bonds between the wood carbohydrates and the PF resins, the number of accessible hydroxyl groups on the surface of the wood substrate is believed to be a crucial parameter. Thus, carbohydrate nanoparticles, having a large surface area with numerous exposed hydroxyl groups, when used as an additive in PF resins, are likely to have a noticeable effect on resin cure.

2.2. CELLULOSE NANOCRYSTALS

Cellulose is one of the main components of plant cell walls and, as such, a well-studied, abundant natural polymer. It was discovered by Anselme Payen in 1838 [36]. It has a chemical formula of $(C_6H_{10}O_5)_n$ and is a linear polysaccharide of D-glucopyranose repeat units joined by β-1,4-glucosidic linkages (Figure 2.6). The average chain length, or degree of polymerization (DP), ranges from several hundred to ten thousand depending on the cellulose origin. For example, cellulose from wood pulp has a DP in the range of 300 to 1700, whereas cotton and bacterial cellulose have DPs in the range of 800 to 10,000 [37]. Through parallel alignment and intermolecular hydrogen bonds, cellulose molecules form highly-crystalline microfibrils with high mechanical strength, as well as thermal and chemical stability.

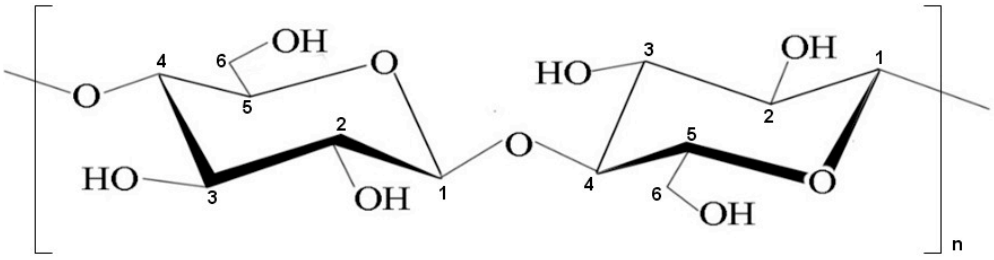

Figure 2.6. Molecular structure of cellulose (n = (DP–2)/2).

Considering the current efforts toward environmental sustainability, cellulose has many advantages compared to petroleum-based materials: Cellulose is biodegradable, derived from renewable resources, biocompatible, nontoxic, and inexpensive. Cellulose and cellulose derivatives have been used extensively in the manufacture of paper, pharmaceuticals, foods, textiles and cosmetics [37].

Although cellulose has been used for centuries in many industrial applications, nanoscale cellulose materials, such as cellulose nanocrystals, are only recently gaining attention, following the advent of nanotechnology. The unique properties of cellulose nanocrystals, such as their rod-like shape, high surface area-to-volume ratio, high stiffness, tendency to form liquid crystalline phases, and ease of chemical modification, make them interesting candidates for both fundamental and applied research in academia

and industry. Current development efforts of nanotechnologies based on cellulose nanocrystals are likely to result in a range of new applications for cellulose.

2.2.1. Preparation and properties

As mentioned above, cellulose molecules assemble in nature into microfibrils (Figure 2.7). The β-1,4-glucosidic linkages in a cellulose molecule are susceptible to acid-catalyzed cleavage, leading to the degradation of the molecule. The acidic degradation of cellulose microfibrils has been studied since the mid 1900's [38].

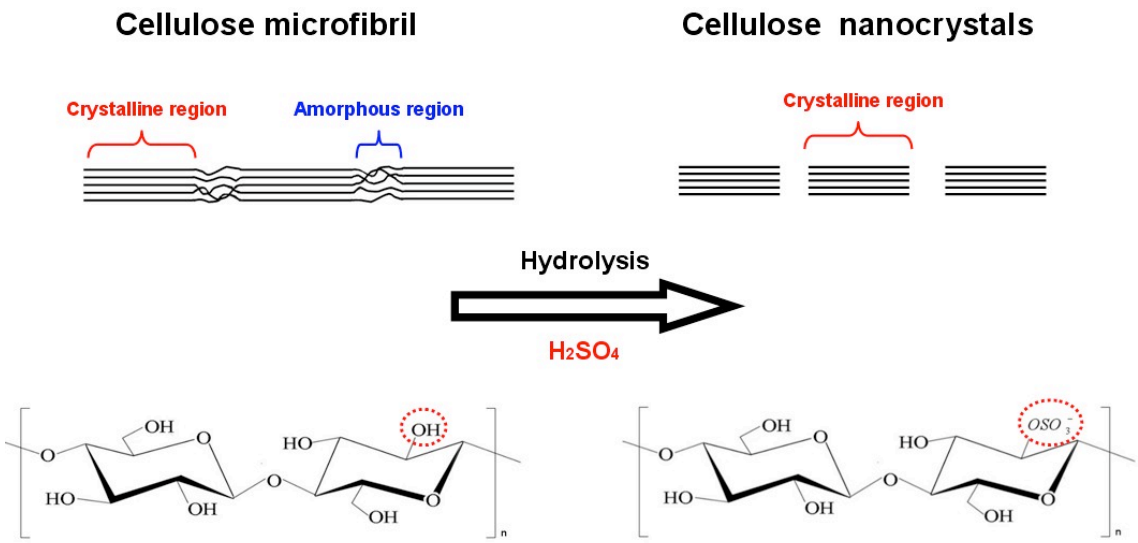

Figure 2.7. The two effects of sulfuric acid during the acid-catalyzed hydrolysis of cellulose: Fragmentation of the cellulose microfibrils, due to the preferred degradation of the amorphous regions, and esterification of some of the hydroxyl groups on the surface of the fragments.

These microfibrils contain highly-ordered, crystalline regions separated by regions in which the chain packing is slightly less dense, commonly termed 'amorphous regions'. Due to the slightly lower density, the amorphous regions are more accessible to chemicals and therefore more susceptible to acidic degradation than the crystalline

regions. As a consequence, acidic degradation of cellulose microfibrils leads to breakdown of the microfibrils into short, rigid, highly-crystalline microfibril fragments, nowadays referred to as cellulose nanocrystals (CNCs) [38, 39]. Under certain hydrolysis conditions, CNCs form stable colloidal suspensions [40].

The properties of the CNCs depend on the cellulose source as well as the hydrolysis conditions, such as acid type and concentration, hydrolysis temperature, and hydrolysis time. Most commonly, sulfuric or hydrochloric acid is used for the hydrolysis, depending on the purpose of the CNCs and desired properties. The main difference between CNCs prepared by sulfuric-acid hydrolysis and hydrochloric-acid hydrolysis is the resulting surface charge. Sulfuric acid hydrolysis introduces sulfate groups on the surface of the CNCs (Figure 2.7), whereas hydrochloric acid does not [41-49]. These negatively charged sulfate groups cause electrostatic stabilization of the aqueous CNC suspension. However, decomposition reaction catalyzed by these sulfate groups may influence the thermal stability of the CNCs [50]. It has been reported that the thermal stability of CNCs decreases with increasing sulfate content [50]. Although CNCs prepared by hydrochloric-acid hydrolysis are more thermally stable than those prepared by sulfuric-acid hydrolysis, they are generally not preferred because they tend to aggregate due to the lack of repulsive electrostatic forces between the particles [43].

The negative surface charge and rod-like shape of CNCs cause aqueous CNC suspensions to form colloidal liquid-crystalline phases [40, 41, 43, 51-53]. At low concentrations (< 1 wt %), CNCs are randomly oriented and the CNC suspension is isotropic. However, above a critical concentration, the CNCs become ordered with respect to their orientation and assemble into a chiral-nematic (cholesteric) structure [40]. Because CNCs are polydisperse in terms of length, CNC suspensions exhibit a biphasic concentration regime in which the isotropic and anisotropic phase coexist. At very high concentrations (>15 wt%), CNC suspensions are entirely chiral-nematic. The width and location of the biphasic concentration regime is primarily governed by length of the rod-like nanoparticles, which is in turn affected by the hydrolysis conditions [42, 54-56].

The orientational order and alignment of CNCs in liquid-crystalline suspensions has implications for the rheology of these suspensions. It has been reported that aqueous

suspensions of CNCs have three distinct shear-viscosity regimes [57]. At low shear rates, anisotropic CNC suspensions are shear thinning due to the rearrangement of ordered domains in the suspension. At high shear rates , CNC suspensions are also shear thinning, but here the shear-thinning behavior is due to the breakdown of domains and alignment of individual CNCs. At intermediate shear rates, CNC suspensions exhibit a Newtonian plateau during which the domains are aligned in the shear direction [58].

As is common for liquid-crystalline phases, chiral-nematic CNC suspensions exhibit interesting optical properties and iridescent colors. The optical properties of anisotropic CNC suspensions can be retained in solid films by slow evaporation of the liquid under conditions that preserve the alignment of the CNCs in the suspension [40, 59, 60]. The iridescent properties of solid CNC films have been found to be governed by the dimensions of the chiral-nematic structure and the texture of the CNC suspension [59].

The average dimensions of CNCs differ widely with cellulose source. For instance, CNCs from wood cellulose are approximately 100-300 nm in length and 3-5 nm in width [61], CNCs from cotton cellulose are 200-350 nm in length and 5 nm in width [61], and CNCs from bacterial cellulose are 100 nm to several micrometer in length and 30-50 nm in width [62, 63]. Besides the cellulose source, the hydrolysis conditions govern the final dimensions of the CNCs. Longer hydrolysis times have been found to cause a decrease in average length [64].

By reason of their high strength and stiffness, CNCs with a high aspect ratio, i.e. length-to-width ratio, have attracted interest as reinforcing additives in polymer composites. The Young's modulus of CNCs has been estimated to 150 GPa, and the bending strength to 10 GPa [65, 66]. It has been reported that a small amount of tunicate whiskers (< 10%) significantly improved the stiffness of latex films [67] and the reinforcement effect has been attributed to a rigid, hydrogen-bonded network. Furthermore, CNCs have been found to influence both the melting temperature and crystallization behavior of the polymer matrix [63, 68, 69].

2.3. CHARACTERIZATION OF THERMOSETTING WOOD ADHESIVES

PF resins are thermosetting resins. The terms “thermo” and “setting” indicate that application of heat causes these materials to solidify and “set” into a final shape through polymerization. The resulting polymer has a crosslinked, three-dimensional network structure and an infinite molecular weight. As opposed to thermoplastic polymers, which are reversibly molded into shapes from a polymer melt, thermosetting polymers undergo irreversible chemical reactions during solidification. The chemical reactions lead to molecular chain growth, branching, and crosslinking. Thermoset cure involves two steps, gelation and vitrification. Gelation marks the incipient formation of a crosslinked network. The gel point is a distinct characteristic of a thermoset at which it looses its ability to flow. The viscosity at the gel point is unmeasurable because the polymer begins to exhibit characteristics of solids. Vitrification occurs when the glass transition temperature, T_g, of the polymer has risen to the cure temperature. At the vitrification point, the polymer transforms from a liquid or rubbery material into a brittle glass.

Several studies have been performed to characterize PF resin cure in terms of gelation and vitrification events and the results of these studies are commonly reported in form of time-temperature-transformation (TTT) cure diagrams [70-73]. The TTT cure diagram (Figure 2.8), developed by Gillham, provides an overview of the cure behavior of a thermosetting material [74]. It describes the required time and temperature to achieve certain events during curing. Three critical temperatures have been defined along the temperature axis of the diagram: the glass transition temperature of the completely unreacted material, T_{g0}, the temperature at which gelation and vitrification coincide, ${}_{gel}T_g$, and the glass transition temperature of the completely cured network, $T_{g\infty}$. The diagram is constructed by plotting the times to gelation and vitrification during isothermal cure against the cure temperature for different cure temperatures.

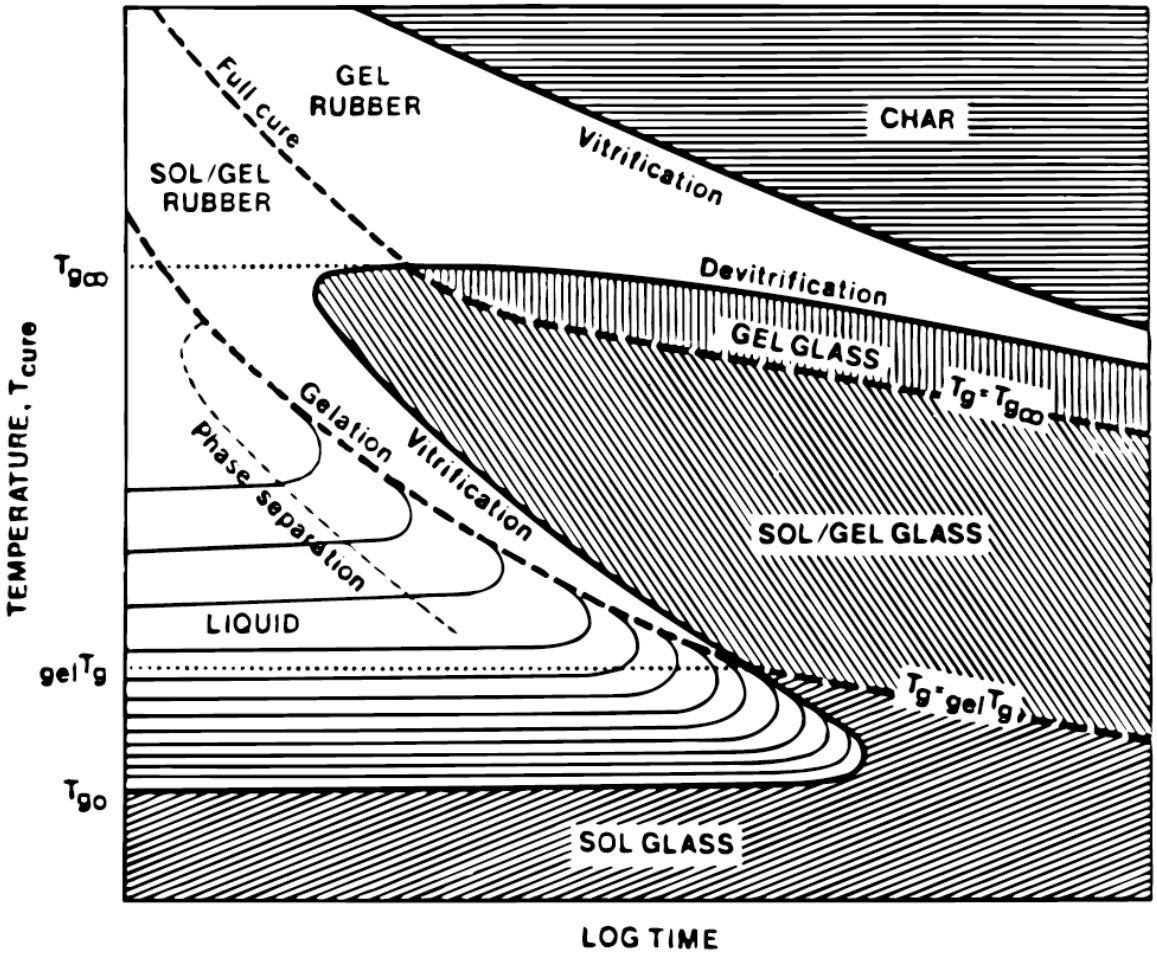

Figure 2.8. Schematic time–temperature–transformation (TTT) isothermal cure diagram. (Reprinted from ref 75; fair use; Copyright 1997 Society of Chemical Industry)

2.3.1. Viscosity and flow behavior

The viscosity and flow behavior of a wood adhesive resin are important factors in its performance because they affect the spreading of the resin on the wood surface and the penetration of the resin into the wood cavities. In the manufacture of wood-based composites, the adhesive is applied by different methods, including spraying, roller coating, and brushing. Each method requires a different resin viscosity for optimal spreading of the resin. Furthermore, a low viscosity promotes deep penetration into the

wood cavities, and therefore mechanical interlocking, whereas a high viscosity demotes it. Excessive penetration, however, can result in a starved bondline and poor joint strength. Thus, the optimum viscosity depends on the method of resin application and desired depth of penetration. PF resins are typically Newtonian liquids, which means that their viscosity is independent of shear rate. However, the rheological properties of commercial PF resins may be altered by resin additives, fillers, and extenders.

Rheology is the study of the deformation and flow of materials [76]. Rheological studies provide important information for polymer processing. The rheological properties of a given liquid can be described in terms of viscosity, shear rate, shear stress, and shear strain. The viscosity is one of the most important parameters and plays an crucial role in the flow behavior of a fluid. The viscosity, η, is the ratio of shear stress, τ, to shear rate, $\dot{\gamma}$

$$\eta = \frac{\tau}{\dot{\gamma}} \qquad [2.1]$$

For Newtonian fluids, the viscosity remains constant with increasing or decreasing shear rate (Figure 2.9). If the viscosity of the fluid is a function of shear rate, the flow behavior is called non-Newtonian (Figure 2.9).

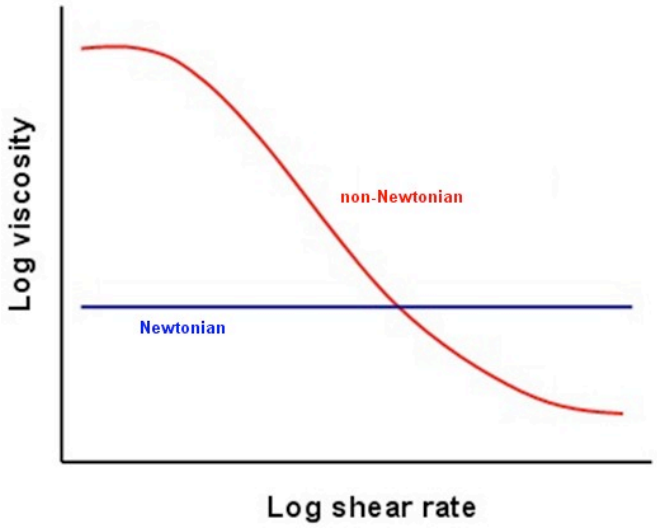

Figure 2.9. Typical Newtonian and non-Newtonian flow behavior on a log scale.

Three types of non-Newtonian flow behavior can be distinguished: shear-thinning, shear-thickening, and viscoplastic. A shear-thinning (or pseudoplastic) fluid shows a decrease in viscosity with increasing shear rate. Fluids that show the opposite behavior are called shear-thickening (or dilatant). A viscoplastic fluid, also called a Bingham plastic, exhibits Newtonian flow behavior when the applied shear stress exceeds a yield stress, τ_0. The shear stress versus shear rate curves for the different types of flow behavior are illustrated in Figure 2.10(a). Figure 2.10(b) shows the viscosity–shear rate curve for a shear-thinning fluid exhibiting a zero shear Newtonian plateau. η_0 and η_∞ are the zero shear viscosity and infinite shear rate viscosity, respectively.

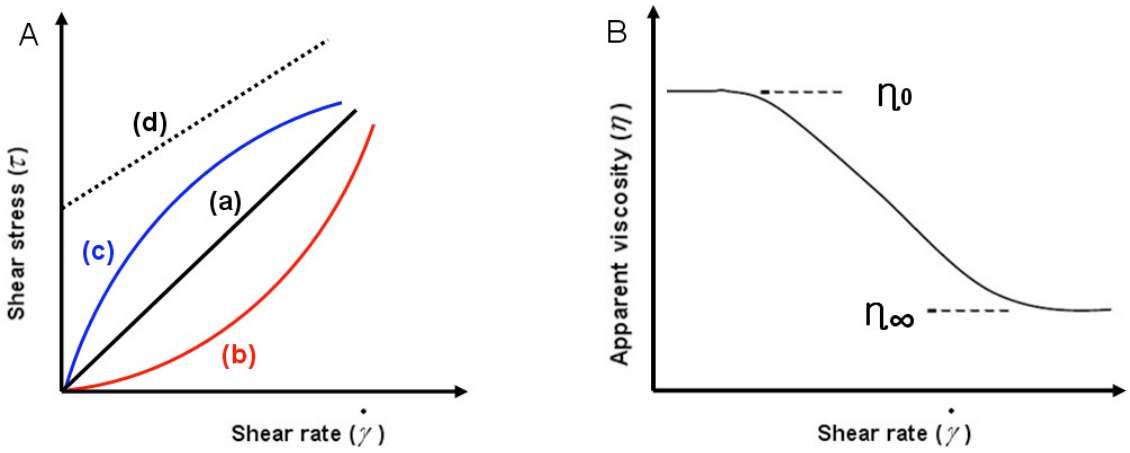

Figure 2.10. A. Four basic flow types of liquids: (a) Newtonian, (b) Shear-thickening, (c) Shear-thinning, (d) Bingham plastic; B. Schematic diagram of typical shear-thinning behavior.

For simplicity, the viscosity of PF resins is often measured with a viscometer. However, viscometers cover only a limited number of shear rates. Steady state flow measurements with a rheometer can provide viscosity values for a broad range of shear rates. The cone and plate geometry (Figure 2.11), where a liquid is sandwiched between a bottom plate and a rotating cone, has the advantage that it provides a uniform shear rate across the entire cone surface [77]. Accurate determination of the viscosity and flow behavior of a PF resin are essential for quality control in wood adhesive manufacturing.

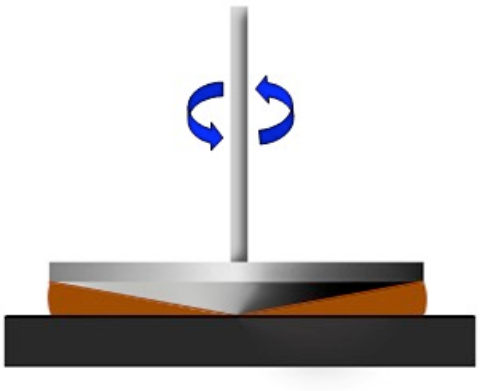

Figure 2.11. Schematic illustration of a steady-state flow experiment using a rheometer with cone and plate geometry. The liquid is sandwiched between the bottom plate and the cone, which rotates at a set rate.

2.3.2. Cure kinetics

Differential scanning calorimetry (DSC) is a thermal analysis technique that can be used to study the curing process of thermosetting polymer systems. DSC is able to measure enthalpy or heat capacity changes in a sample subjected to a controlled thermal profile. DSC measurements can provide not only information about phase transitions in polymers, such as the glass transition, crystallization, and melting, but also about the rate of chemical conversion during thermoset cure [78].

DSC has been extensively used to study the cure kinetics of PF resol resins [72, 79-86]. PF resols typically exhibit two exothermic peaks during a DSC dynamic temperature scan. However, the interpretation of these two peaks is controversial. In most reports, the first peak has been attributed to the addition reactions between free formaldehyde and the phenolic rings and the second peak to the condensation reactions [83-85]. A few studies, however, have attributed the first peak to HMP formation and condensation and the second peak to the formation and decomposition of dimethylene ether bridges between phenolic moieties [86].

In recent years, DSC has also been used to study the influence of wood on the cure kinetics of PF resins [31, 87, 88]. Wood was found to accelerate the addition reactions

but retard the condensation reactions [31]. Because DSC does not provide information about the changes in the chemical structure during cure, the molecular mechanisms by which wood affects resin cure cannot be determined by DSC alone. Analysis of the reaction kinetics by DSC, however, can provide valuable information about the curing processes. Several methods have been developed for the determination of kinetic parameters, such as the activation energy, E_a, frequency factor, Z, and rate constant, k, by DSC, such as the Borchart–Daniels method, the isoconversional method (ASTM-E698), the isothermal method, and model-free methods [89, 90]. The method described by ASTM-E698 has the advantage that it allows analysis of reactions with irregular baselines or multiple exothermic peaks because it is based on peak temperatures, measured at different heating rates, which are not affected significantly by the shape of the baseline [91, 92]. The ASTM-E698 approach for the determination of reaction kinetics assumes Arrhenius behavior and first order reaction kinetics. Moreover, it requires determination of the peak temperatures at a minimum of three different heating rates, generally chosen to lie between 1 and 10 °C/min [93].

2.3.3. Changes in mechanical properties during cure

Dynamic mechanical analysis (DMA) is a technique that can be used to characterize the mechanical properties of viscoelastic materials as a function of frequency, time, and temperature. DMA measures the elastic and viscous response of the material upon application of a sinusoidal force. The elastic response is reported as the storage modulus, *E'* or *G'*, depending on the mode of deformation, and the viscous response is reported as the loss modulus, *E"* or *G"*. The ratio of loss to storage modulus, *E"*/*E'* or *G"*/*G'*, is a quantity called tan δ, which is a measure for the energy dissipated by the material during deformation. The study of gelation and vitrification processing in thermosetting resins, specifically epoxy resins, by DMA was pioneered by Gillham in the early 1970's using a torsional braid system [94]. DMA was found to be very sensitive to changes in the mechanical properties of thermosetting polymers associated with gelation and vitrification processes. Events related to the gelation or vitrification of the resin are

generally detected in both the storage modulus and tan δ traces. As a result, DMA has been widely used to characterize thermosetting resins during cure [72, 73, 95-101].

The challenge of measuring the mechanical properties of thermosetting resins during cure is that the resin is initially liquid and therefore lacks mechanical integrity. Thus, many studies have employed fiberglass braids or wood pieces of different geometry as substrates to support the liquid resin prior to gelation. [28, 29, 33, 73, 102-105]. Because of the hygroscopic and viscoelastic nature of wood, and natural variations in the wood structure, fiberglass braid substrates tend to yield more reproducible results than wood substrates. Wood substrates, on the other hand, have the advantage that they more realistically emulate the curing conditions during wood-based composites manufacture and are able to provide information about the effect of wood on resin cure. Consequently, many studies of the curing behavior of PF resins have employed impregnated wood strips [102] or sandwich-type specimens, consisting of a layer of resin between two wood strips [34, 106]. One has to keep in mind, however, that the mechanical properties of these specimens are not those of the resin alone but of the whole specimen, i.e. that changes in the mechanical properties of the wood substrate have to be taken into account when interpreting of the results.

2.3.4. Fracture behavior

An assembly consisting of two objects bonded by an adhesive is called an adhesive joint. The two objects that are bonded by the adhesive are called adherends. Adhesive joints are characterized by their strength under tensile and shear loading and by their fracture toughness, i.e. their resistance to crack propagation. The fracture toughness determines the load-bearing capacity of a structure in the presence of flaws and can be measured with cleavage tests. In a cleavage test, a cracked body is stressed in one of three modes, depicted in Figure 2.12, and the load required to propagate the crack is measured.

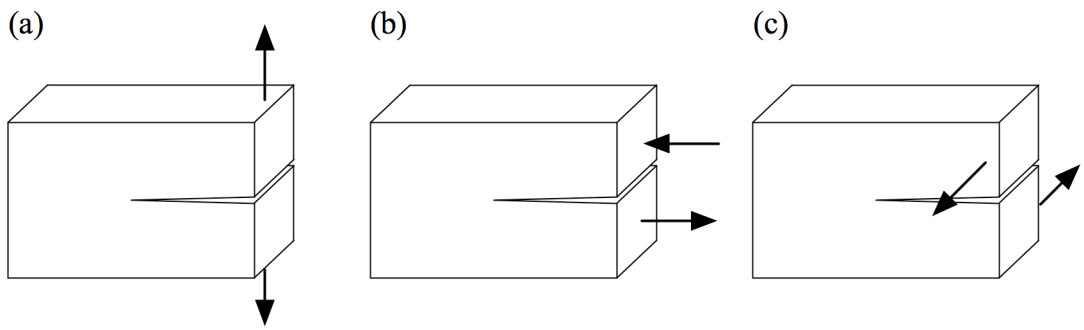

Figure 2.12. Mode of loading in cleavage tests: (a) mode I, tensile (opening), (b) mode II, in-plane shear, (c) mode III, anti-plane (transverse) shear or tear.

For some types of adhesive joints, standard test methods have been developed by ASTM International, originally known as the American Society for Testing and Materials (ASTM). For adhesive joints involving wood adherends, however, available standards are limited to the evaluation of joint strength under shear [107-110] and tensile loading [111]. The performance of wood adhesive joints is traditionally assessed by a combination of the joint strength under shear loading (ASTM D905 or D906) and the percentage of wood failure in the tested joints (ASTM D5266, [112]). Adhesive joints are generally strongest under shear loading and weakest under cleavage loading [113]. Under shear loading, the strength of the joint often exceeds that of the wood. As a consequence, the load values for joint failure depend more on the strength of the wood than on the adhesive or cohesive strength of the adhesive. In other words, joint strength tests under shear loading are often limited by the strength of the wood and do not provide much information on the strength of the joint other than that it is higher than the strength of the adherend.

The shortcomings of the traditional approach to evaluating wood adhesive joints and the advantages of cleavage tests were recognized as early as 1965 by Stanger and Blomquist [113], who showed in a comparison of the conventional block shear test, the cross-lap tension test, and a cleavage test that the latter produced a lower percentage of wood failure and was therefore more sensitive to bondline properties. In the mid and late 1970s, cleavage testing of wood adhesive joints was further advanced by several groups through the application of linear elastic fracture mechanics (LEFM) [114-121].

LEFM predicts the conditions for crack propagation in a stressed material under the assumption that the material is isotropic and linear elastic, i.e. that it obeys Hooke's law. It is based on two interrelatable approaches. The energy balance approach by Griffith [122] stipulates that crack propagation occurs when the elastic or strain energy that is released by the propagation of the crack is sufficient to overcome the energy required for the formation of the new fracture surfaces. It further stipulates that below a critical crack length a_c, the crack only propagates when the stress is increased, but above this critical crack length, crack propagation is spontaneous and catastrophic. For plane stress loading and unit specimen thickness, the critical stress level σ_c, at which crack propagation occurs for a given crack length a is given by:

$$\sigma_c^{\,2} = \frac{2E\gamma}{\pi a} \qquad [2.1]$$

where E is the elastic modulus and γ the surface energy of the material. Griffith's model, which applies only to highly brittle materials, was subsequently extended independently by Irwin [123] and Orowan [124] to materials that exhibit plastic flow near the crack tip. Irwin and Orowan argued that in a material that exhibits plastic flow near the crack tip, the energy required for the formation of new fracture surfaces is negligible, and that for crack propagation to occur, the released strain energy has to be greater than the energy dissipated through plastic flow near the crack tip. According to Irwin and Orowan, catastrophic failure occurs at a critical strain energy release rate (SERR), G_c, often referred to as fracture energy. G_c is related to σ_c, a, and E through

$$G_c = \frac{\pi a \sigma_c^{\,2}}{E} \qquad [2.2]$$

For a cracked body of thickness b that exhibits linear elastic behavior away from the crack tip, eq 2.x may be expessed as

$$G_c = \frac{P_c^2}{2b}\left(\frac{\partial C}{\partial a}\right) \qquad [2.3]$$

where P_c is the critical load required for crack propagation and C is the compliance, i.e. the ratio of displacement or deformation to applied load.

The stress intensity factor approach by Irwin [125] introduces a parameter K, called the stress intensity factor, that describes the stress field ahead of the crack tip. Irwin argued that crack propagation occurs when the stess intensity factor exceeds a critical value K_c, termed fracture toughness, which represents a material property for given test conditions. For mode I loading of a crack located away from the edge in a finite plate, the fracture toughness is given by

$$K_{Ic} = Y\sigma_c\sqrt{\pi a} \qquad [2.4]$$

where the subscript I indicates mode I loading and Y is a factor accounting for specimen geometry. For plane stress conditions, K_{Ic} and the critical SERR for mode I loading, G_{Ic}, are related through

$$G_{Ic} = \frac{K_{Ic}^{\ 2}}{E} \qquad [2.5]$$

In their first study [114], published in 1974, Komatsu *et al.* measured the fracture energy G_c of wood–epoxy joints using balanced double lap joint specimens, as shown in Figure 2.13. The specimens were tested under tensile lap shear loading and the compliance for different crack lengths was determined from load–displacement curves. To obtain G_c values that were indipendent of crack length, the authors had to apply a mathematical correction for the dependence of the specimen compliance on the length of the bondline.

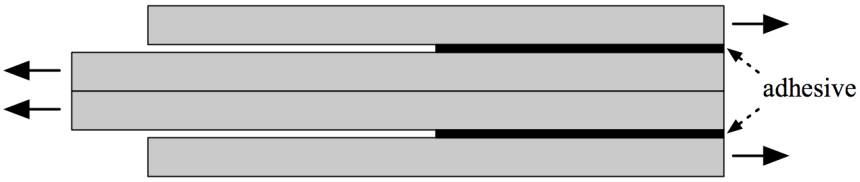

Figure 2.13. Specimen geometry used by Komatsu *et al.* in their first study. (Reprinted from ref 115; fair use; Copyright 1974 Kyoto University)

In their subsequent study, Komatsu *et al.* evaluated mode I cleavage loading and the simpler double cantilever beam (DCB) geometry, schematically shown in Figure 2.14(a) [115, 116]. The authors used the compliance method for the determination of G_{Ic} values and, in the second part of the study [116], accounted for the non-linear elastic behavior of the test specimens.

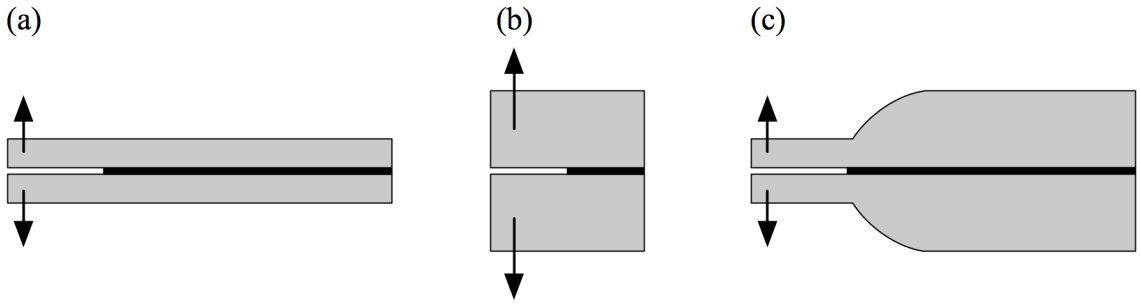

Figure 2.14. Specimen geometries for mode I cleavage tests: (a) double cantilever beam, (b) compact tension, (c) contoured double cantilever beam.

Almost concurrently with Komatsu *et al.*, White [117, 118] and White and Green [119] evaluated a different approach. These authors used the compact tension test to measure the fracture toughness K_I of wood–resorcinol resin joints. The compact tension specimen geometry is schematically shown in Figure 2.14(b). In a compact tension test, the critical load P_c is determined from load–displacement curves and K_{Ic} is calculated from the P_c values, the specimen dimensions, and the crack lengths. The compact tension test for application to wood–adhesive joints was also evaluated by Ruedy [126] and Kyokong *et al.* [127].

In 1979, Ebewele *et al.* [120, 121] reported a method for G_{Ic} determination that was based on the contoured double cantilever beam (CDCB) geometry, schematically shown in Figure 2.14(c). The CDCB geometry is designed to yield a constant $\partial C/\partial a$ (see eq 2.3). The advantage of CDCB specimens over DCB specimens is that they require only P_c to be measured, whereas DCB specimens require the simultaneous measurement of P_c and a. The disadvantage of CDCB specimens is that they are more difficult to prepare and that they may require calibration.

More recently, Gagliano and Frazier have evaluated a method for G_{Ic} determination that uses the simpler DCB geometry and the compliance method in combination with the corrected beam theory for data analysis [128-130]. The method involves cyclical loading of the test specimen and measurement of the crack length with a CCD camera and 10 × magnification. The method was found to be sensitive to adhesive parameters and a simplification with respect to the method by Ebewele *et al.*

Since the introduction of LEFM into wood–adhesive joint evaluation, cleavage tests have been used to study many different factors in joint performance, including resin penetration [117, 118], bonding pressure [117, 118], earlywood vs. latewood [117-119], grain orientation [117, 118, 120, 126], wood surface preparation [117, 119, 121, 131], wood species [117, 119, 126], bondline thickness [120, 126], wood surface aging [121, 131-133], moisture content [131], resin composition [134], cure time [120, 134-136], cure temperature [134], resin aging [136], type of filler [137], temperature [138, 139], and resin droplet diameter and spacing [129].

2.4. REFERENCES

[1] Baekeland, L. H. Condensation Product and Method of Making Same. U.S. Patent 942,809, Dec. 7, 1909.

[2] Knop, A.; Scheib, W. Chemistry and Application of Phenolic Resins. Springer: Heidelberg, Germany, 1979.

[3] Shafizadeh, J. E.; Guionnet, S.; Tillman, M. S.; Seferis, J. C. Synthesis and characterization of phenolic resole resins for composite applications. Journal of Applied Polymer Science 1999, 73, 505-514.

[4] Pasch, H.; Schrod, M. Preparation and analysis of phenol-formaldehyde resins by high-throughput techniques. Eindhoven, Netherlands, Jun, 2003; pp 224-230.

[5] Knop, A.; Pilato, L. Phenolic Resins. Springer: Heidelberg, Germany, 1985.

[6] Sellers, T. Production Numbers Reveal Worldwide Emphasis of Wood Adhesives. Panel World 2004, 45, 34-36.

[7] Marra, A. A. Technology of Wood Bonding: Principles in Practice. Van Nostrand Reinhold: New York, 1992.

[8] Frihart, C. R. Wood Adhesion and Adhesives. In: Handbook of Wood Chemistry and Wood Composites; Rowell, R. M., Ed.; CRC Press: Boca Raton, FL, 2005.

[9] Sellers, T. Plywood and Adhesive Technology. Marcel Dekker: New York, 1985.

[10] Kim, M. G.; Nieh, W. L.; Sellers, T.; Wilson, W. W.; Mays, J. W. Polymer-Solution Properties of a Phenol Formaldehyde Resol Resin by Gel-Permeation Chromatography, Intrinsic-Viscosity, Static Light-Scattering, and Vapor-Pressure Osmometric Methods. Industrial & Engineering Chemistry Research 1992, 31, 973-979.

[11] Kim, M. G.; Watt, C.; Davis, C. R. Effects of urea addition to phenol-formaldehyde resin binders for oriented strandboard. Journal of Wood Chemistry and Technology 1996, 16, 21-34.

[12] Pizzi, A. Phenolic Resin Wood Adhesives. In: Wood Adhesives Chemistry and Technology; Pizzi, A., Ed.; Marcel Dekker: New York, 1983.

[13] Lin-Gibson, S.; Riffle, J. S. Chemistry and Properties of Phenolic Resins and Networks. In: Synthetic methods in step-growth polymers; Rogers, M. E., Long, T., Eds.; John Wiley & Sons: Hoboken, NJ, 2003; pp 375-430.

[14] Winkelman, J. G. M.; Voorwinde, O. K.; Ottens, M.; Beenackers, A. A. C. M.; Janssen, L. P. B. M. Kinetics and chemical equilibrium of the hydration of formaldehyde. Chemical Engineering Science 2002, 57, 4067-4076.

[15] Pizzi, A. Advanced Wood Adhesives Technology. Marcel Dekker: New York, 1994.

[16] Higuchi, M.; Urakawa, T.; Morita, M. Condensation reactions of phenolic resins. 1. Kinetics and mechanisms of the base-catalyzed self-condensation of 2-hydroxymethylphenol. Polymer 2001, 42, 4563-4567.

[17] Jones, T. T. Some preliminary investigations of the phenolformaldehyde reaction. Journal of the Society of Chemical Industry 1946, 65, 264-275.

[18] Lebach, H. Über Resinit. Angewandte Chemie 1910, 22, 1598-1601.

[19] Baekeland, L. H.; Bender, H. L. Phenol resins and resinoids. Journal of Industrial and Engineering Chemistry 1925, 17, 225-37.

[20] Zinke, A. The chemistry of phenolic resins and the process leading to their formation. Journal of Applied Chemistry 1951, 1, 257-66.

[21] Maciel, G. E.; Chuang, I. S.; Gollob, L. Solid-state carbon-13 NMR study of resol-type phenol-formaldehyde resins. Macromolecules 1984, 17, 1081-1087.

[22] Pizzi, A.; Eaton, N. J. A conformational analysis approach to phenol-formaldehyde resins adhesion to wood cellulose. Journal of Adhesion Science and Technology 1987, 1, 191-200.

[23] Pizzi, A. A Molecular Mechanics Approach to the Adhesion of Urea Formaldehyde Resins to Cellulose. 2. Amorphous vs Crystalline Cellulose-I. Journal of Adhesion Science and Technology 1990, 4, 589-595.

[24] Pizzi, A.; De Sousa, G. On the Resolution of Dihydroxydiphenylmehtanes on Achiral Crystalline Cellulose-II-Correlation of Experimental and Calculated Results. Chemical Physics 1992, 164, 203-216.

[25] Johns, W. E. The Chemical Bonding of Wood. In: Wood Adhesives Chemistry and Technology; Pizzi, A., Ed.; Marcel Dekker: New York, 1989; Vol. 2.

[26] Chow, S. Z. Kinetic study of the polymerization of phenol-formaldehyde resin in the presence of cellulosic materials. Wood Science 1969, 1, 215-221.

[27] Mizumachi, H.; Morita, H. Activation energy of the curing reaction of phenolic resin in the presence of woods. Wood Science 1975, 7, 256-260.

[28] Lu, X.; Pizzi, A. Curing conditions effects on the characteristics of thermosetting adhesives-bonded wood joints - Part 1: Substrate influence on TTT and CHT curing diagrams of wood adhesives. Holz als Roh- und Werkstoff 1998, 56, 339-346.

[29] Pizzi, A.; Lu, X.; Garcia, R. Lignocellulosic substrates influence on TTT and CHT curing diagrams of polycondensation resins. Journal of Applied Polymer Science 1999, 71, 915-925.

[30] Lee, S. Y.; Wu, Q. L.; Strickland, B. The influence of flake chemical properties and zinc borate on gel time of phenolic resin for oriented strandboard. Wood and Fiber Science 2001, 33, 425-436.

[31] He, G.; Riedl, B. Curing kinetics of phenol formaldehyde resin and wood-resin interactions in the presence of wood substrates. Wood Science and Technology 2004, 38, 69-81.

[32] He, G.; Yan, N. Effect of wood on the curing behavior of commercial phenolic resin systems. Journal of Applied Polymer Science 2005, 95, 185-192.

[33] Onic, L.; Bucur, V.; Ansell, M. P.; Pizzi, A.; Deglise, X.; Merlin, A. Dynamic thermomechanical analysis as a control technique for thermoset bonding of wood joints. International Journal of Adhesion and Adhesives 1998, 18, 89-94.

[34] Garcia, R.; Pizzi, A. Crosslinked and entanglement networks in thermomechanical analysis of polycondensation resins. Journal of Applied Polymer Science 1998, 70, 1111-1119.

[35] Pizzi, A.; Mtsweni, B.; Parsons, W. Wood-induced catalytic activation of PF adhesives autopolymerization vs PF wood covalent bonding. Journal of Applied Polymer Science 1994, 52, 1847-1856.

[36] Payen, A. Mémoire sur la composition du tissu propre des plantes e du ligneux. Comptes Rendus Hebdomadaires des Seances de l'Academie des Sciences 1838, 7, 1052–1056.

[37] Klemm, D.; Heublein, B.; Fink, H. P.; Bohn, A. Cellulose: Fascinating biopolymer and sustainable raw material. Angewandte Chemie-International Edition 2005, 44, 3358–3393.

[38] Rånby, B. G. The colloidal properties of cellulose micelles. Discussions of the Faraday Society 1951, 11, 158-64, discussion 208-213.

[39] Battista, O. A.; Coppick, S.; Howsmon, J. A.; Morehead, F. F.; Sisson, W. A. Level-off degree of polymerization. Relation to polyphase structure of cellulose fibers. Industrial & Engineering Chemistry 1956, 48, 333-335.

[40] Revol, J. F.; Bradford, H.; Giasson, J.; Marchessault, R. H.; Gray, D. G. Helicoidal self-ordering of cellulose microfibrils in aqueous suspension. International Journal of Biological Macromolecules 1992, 14, 170-172.

[41] Marchessault, R. H.; Morehead, F. F.; Walter, N. M. Liquid crystal systems from fibrillar polysaccharides. Nature 1959, 184, 632-633.

[42] Dong, X. M.; Kimura, T.; Revol, J.-F.; Gray, D. G. Effects of Ionic Strength on the Isotropic-Chiral Nematic Phase Transition of Suspensions of Cellulose Crystallites. Langmuir 1996, 12, 2076-2082.

[43] Araki, J.; Wada, M.; Kuga, S.; Okano, T. Flow properties of microcrystalline cellulose suspension prepared by acid treatment of native cellulose. Colloids and Surfaces, A: Physicochemical and Engineering Aspects 1998, 142, 75-82.

[44] Bercea, M.; Navard, P. Shear Dynamics of Aqueous Suspensions of Cellulose Whiskers. Macromolecules 2000, 33, 6011–6016.

[45] Araki, J.; Kuga, S. Effect of Trace Electrolyte on Liquid Crystal Type of Cellulose Microcrystals. Langmuir 2001, 17, 4493-4496.

[46] De Souza Lima, M. M.; Borsali, R. Static and dynamic light scattering from polyelectrolyte microcrystal cellulose. Langmuir 2002, 18, 992-996.

[47] Beck-Candanedo, S.; Roman, M.; Gray, D. G. Effect of Reaction Conditions on the Properties and Behavior of Wood Cellulose Nanocrystal Suspensions. Biomacromolecules 2005, 6, 1048-1054.

[48] Montanari, S.; Rountani, M.; Heux, L.; Vignon, M. R. Topochemistry of carboxylated cellulose nanocrystals resulting from TEMPO-mediated oxidation. Macromolecules 2005, 38, 1665-1671.

[49] Bordel, D.; Putaux, J. L.; Heux, L. Orientation of native cellulose in an electric field. Langmuir 2006, 22, 4899-4901.

[50] Roman, M.; Winter, W. T. Effect of Sulfate Groups from Sulfuric Acid Hydrolysis on the Thermal Degradation Behavior of Bacterial Cellulose. Biomacromolecules 2004, 5, 1671-1677.

[51] Dong, X. M.; Revol, J.-F.; Gray, D. G. Effect of microcrystallite preparation conditions on the formation of colloid crystals of cellulose. Cellulose 1998, 5, 19-32.

[52] Revol, J. F.; Godbout, L.; Dong, X. M.; Gray, D. G.; Chanzy, H.; Maret, G. Chiral nematic suspensions of cellulose crystallites; phase separation and magnetic field orientation. Liquid Crystals 1994, 16, 127-134.

[53] Araki, J.; Wada, M.; Kuga, S.; Okano, T. Birefringent glassy phase of a cellulose microcrystal suspension. Langmuir 2000, 16, 2413-2415.

[54] Onsager, L. The effects of shapes on the interaction of colloidal particles. Annals of the New York Academy of Sciences 1949, 51, 627-659.

[55] Stroobants, A.; Lekkerkerker, H. N. W.; Odijk, T. Effect of electrostatic interaction on the liquid crystal phase transition in solutions of rodlike polyelectrolytes. Macromolecules 1986, 19, 2232-2238.

[56] Speranza, A.; Sollich, P. Simplified Onsager theory for isotropic-nematic phase equilibria of length polydisperse hard rods. Journal of Chemical Physics 2002, 117, 5421-5436.

[57] Orts, W. J.; Godbout, L.; Marchessault, R. H.; Revol, J. F. Shear-Induced Alignment of Liquid-Crystalline Suspensions of Cellulose Microfibrils. In: Flow-Induced Structure in Polymers; Nakatani, A. I., Dadmun, M. D., Eds.; ACS Symposium Series 597; American Chemical Society: Washington, DC, 1994; pp 335-348.

[58] De Souza Lima, M. M.; Borsali, R. Rodlike cellulose microcrystals: Structure, properties, and applications. Macromolecular Rapid Communications 2004, 25, 771-787.

[59] Sugiyama, J.; Chanzy, H.; Maret, G. Orientation of Cellulose Microcrystals by Strong Magnetic Fields. Macromolecules 1992, 25, 4232-4234.

[60] Roman, M.; Gray, D. G. Parabolic Focal Conics in Self-Assembled Solid Films of Cellulose Nanocrystals. Langmuir 2005, 21, 5555-5561.

[61] Fengel, D.; Wegener, G. Wood: Chemistry, Ultrastructure, Reactions. Walter De Gruyter: New York, 1984.

[62] Tokoh, C.; Takabe, K.; Fujita, M.; Saiki, H. Cellulose synthesized by Acetobacter xylinum in the presence of acetyl glucomannan. Cellulose 1998, 5, 249-261.

[63] Grunert, M.; Winter, W. T. Nanocomposites of cellulose acetate butyrate reinforced with cellulose nanocrystals. Journal of Polymers and the Environment 2002, 10, 27–30.

[64] Dong, X. M.; Revol, J.-F.; Gray, D. G. Effect of microcrystallite preparation conditions on the formation of colloid crystals of cellulose. Cellulose 1998, 5, 19–32.

[65] Sturcova, A.; Davies, G. R.; Eichhorn, S. J. Elastic Modulus and Stress-Transfer Properties of Tunicate Cellulose Whiskers. Biomacromolecules 2005, 6, 1055–1061.

[66] Helbert, W.; Cavaillé, J. Y.; Dufresne, A. Thermoplastic nanocomposites filled with wheat straw cellulose whiskers. Part I: Processing and mechanical behavior. Polymer Composites 1996, 17, 604–611.

[67] Favier, V.; Chanzy, H.; Cavaillé, J. Y. Polymer Nanocomposites Reinforced by Cellulose Whiskers. Macromolecules 1995, 28, 6365–6367.

[68] Roman, M.; Winter, W. T. Cellulose nanocrystals for thermoplastic reinforcement: Effect of filler surface chemistry on composite properties. In: Cellulose Nanocomposites: Processing, Characterization, and Properties; ACS Symposium Series; American Chemical Society: Washington, 2006; Vol. 938, pp 99–113.

[69] Dufresne, A.; Vignon, M. R. Improvement of starch film performances using cellulose microfibrils. Macromolecules 1998, 31, 2693-2696.

[70] Palmese, G. R.; Gillham, J. K. Time-temperature-transformation (TTT) cure diagrams: Relationship between Tg and the temperature and time of cure for a polyamic acid/polyimide system. Journal of Applied Polymer Science 1987, 34, 1925-1939.

[71] Young, R. H.; Kopf, P. W.; Salgado, O. Curing Mechanisms of Phenolic Resins. Tappi 1981, 64, 127-130.

[72] Steiner, P. R.; Warren, S. R. Rheology of Wood-Adhesive Cure by Torsional Braid Analysis. Holzforschung 1981, 35, 273-278.

[73] Kim, M. G.; Nieh, W. L. S.; Meacham, R. M. Study on the Curing of Phenol-Formaldhehyde Resol Resins by Dynamic Mechanical Analysis. Industrial & Engineering Chemistry Research 1991, 30, 798-803.

[74] Wisanrakkit, G.; Gillham, J. K.; Enns, J. B. The glass transition temperature (Tg) as a parameter for monitoring the cure of an amine/epoxy system at constant heating rates. Journal of Applied Polymer Science 1990, 41, 1895-1912.

[75] Gillham, J. K. The TBA torsion pendulum: a technique for characterizing the cure and properties of thermosetting systems. Polymer International 1997, 44, 262-276.

[76] Vinogradov, G. V.; Malkin, A. Y. Rheology of Polymers. Springer: New York, 1980.

[77] Rosen, S. L. Fundamental Principles of Polymeric Materials. Wiley: New York, 1993.

[78] Prime, R. B. Thermosets. In: Thermal Characterization of Polymeric Materials; Turi, E. A., Ed.; Academic Press: New York, 1997.

[79] Park, B.-D.; Riedl, B.; Bae, H.-J.; Kim, Y. S. Differential scanning calorimetry of phenol-formaldehyde (PF) adhesives. Journal of Wood Chemistry and Technology 1999, 19, 265-286.

[80] Šebenik, A.; Vizovišek, I.; Lapanje, S. Determination of kinetic parameters for the reaction between phenol and formaldehyde by differential scanning calorimetry. European Polymer Journal 1974, 10, 273-278.

[81] Christiansen, A. W.; Gollob, L. Differential scanning calorimetry of phenol-formaldehyde resols. Journal of Applied Polymer Science 1985, 30, 2279-2289.

[82] Wang, X. M.; Riedl, B.; Christiansen, A. W.; Geimer, R. L. Differential scanning calorimetry of the effects of temperature and humidity on phenol-formaldehyde resin cure. Polymer 1994, 35, 5685-5692.

[83] King, P. W.; Mitchell, R. H.; Westwood, A. R. Structural analysis of phenolic resole resins. Journal of Applied Polymer Science 1974, 18, 1117-1130.

[84] Kenny, J. M.; Pisaniello, G.; Farina, F.; Puzziello, S. Calorimetric analysis of the polymerization reaction of a phenolic resin. Thermochimica Acta 1995, 269/270, 201-211.

[85] Vick, C. B.; Christiansen, A. W. Cure of Phenol-Formaldehyde Adhesive in the Presence of CCA-Treated Wood by Differential Scanning Calorimetry. Wood and Fiber Science 1993, 25, 77-86.

[86] Holopainen, T.; Alvila, L.; Rainio, J.; Pakkanen, T. T. Phenol-formaldehyde resol resins studied by 13C-NMR spectroscopy, gel permeation chromatography, and differential scanning calorimetry. Journal of Applied Polymer Science 1997, 66, 1183-1193.

[87] He, G. B.; Riedl, B.; Ait-Kadi, A. Model-free kinetics: Curing behavior of phenol formaldehyde resins by differential scanning calorimetry. Journal of Applied Polymer Science 2003, 87, 433-440.

[88] He, G. B.; Riedl, B.; Aït-Kadi, A. Curing process of powdered phenol-formaldehyde resol resins and the role of water in the curing systems. Journal of Applied Polymer Science 2003, 89, 1371-1378.

[89] Jang, W. A Review of DSC Kinetic Models. DuPont Instruments, Thermal Analyzers 1989, 15.

[90] Vyazovkin, S. Alternative description of process kinetics. Thermochimica Acta 1992, 211, 181-187.

[91] Schneider, N. S.; Sprouse, J. F.; Hagnauer, G. L.; Gillham, J. K. DSC and TBA studies of the curing behavior of two dicy-containing epoxy resins. Polymer Engineering and Science 1979, 19, 304-312.

[92] Maas, T. A. M. M. Optimalization of processing conditions for thermosetting polymers by determination of the degree of curing with a differential scanning calorimeter. Polymer Engineering & Science 1978, 18, 29-32.

[93] Ozawa, T. Kinetic analysis of derivative curves in thermal analysis. Journal of Thermal Analysis and Calorimetry 1970, 2, 301-324.

[94] Babayevsky, P. G.; Gillham, J. K. Epoxy thermosetting systems. Dynamic mechanical analysis of the reactions of aromatic diamines with the diglycidyl ether of bisphenol A. Journal of Applied Polymer Science 1973, 17, 2067-88.

[95] Myers, G. E.; Christiansen, A. W.; Geimer, R. L.; Follensbee, R. A.; Koutsky, J. A. Phenol-Formaldehyde Resin Curing and Bonding in Steam-Injection Pressing. I. Resin Synthesis, Characterization, and Cure Behavior. Journal of Applied Polymer Science 1991, 43, 237-250.

[96] Christiansen, A. W.; Follensbee, R. A.; Geimer, R. L.; Koutsky, J. A.; Myers, G. E. Phenol-Formaldehyde Resin Curing and Bonding in Steam-Injection Pressing. 2. Differences Between Rates of Chemical and Mechanical Responses to Resin Cure. Holzforschung 1993, 47, 76-82.

[97] Lorenz, L. F.; Christiansen, A. W. Interactions of Phenolic Resin Alkalinity, Moisture-Content, and Cure Behavior. Industrial & Engineering Chemistry Research 1995, 34, 4520-4523.

[98] Kuzak, S. G.; Shanmugam, A. Dynamic mechanical analysis of fiber-reinforced phenolics. Journal of Applied Polymer Science 1999, 73, 649-658.

[99] Umemura, K.; Takahashi, A.; Kawai, S. Durability of isocyanate resin adhesives for wood I: Thermal properties of isocyanate resin cured with water. Journal of Wood Science 1998, 44, 204-210.

[100] Umemura, K.; Takahashi, A.; Kawai, S. Durability of isocyanate resin adhesives for wood. II. Effect of the addition of several polyols on the thermal properties. Tokyo, Japan, Jun 19-20, 1997; pp 1807-1814.

[101] Follensbee, R. A.; Koutsky, J. A.; Christiansen, A. W.; Myers, G. E.; Geimer, R. L. Development of Dynamic Mechanical Methods to Characterize the Cure State of Phenolic Resol Resins. Journal of Applied Polymer Science 1993, 47, 1481-1496.

[102] Laborie, M.-P. G. Investigation of the Wood/Phenol-Formaldehyde Adhesive Interphase Morphology. Dissertation, Virginia Polytechnic Institute and State University, Blacksburg, VA, 2002.

[103] Zanetti, M.; Pizzi, A. Variation of acetal effect on performance of phenol-formaldehyde resin adhesives. Journal of Applied Polymer Science 2004, 91, 2058-2060.

[104] Lee, S. M.; Kim, M. G. Effects of urea and curing catalysts added to the strand board core-layer binder phenol-formaldehyde resin. Journal of Applied Polymer Science 2007, 105, 1144-1155.

[105] Wang, J. W.; Laborie, M. P. G.; Wolcott, M. P. Application of beam mechanics to sensing the cure development of wood-phenolic joints by dynamic mechanical analysis. Thermochimica Acta 2007, 465, 18-24.

[106] He, G. B.; Yan, N. Influence of the synthesis conditions on the curing behavior of phenol-urea-formaldehyde resol resins. Journal of Applied Polymer Science 2005, 95, 1368-1375.

[107] ASTM Standard D905 - 08e1, Standard Test Method for Strength Properties of Adhesive Bonds in Shear by Compression Loading, ASTM International, West Conshohocken, PA, 2008, DOI: 10.1520/D0905-08E01, www.astm.org.

[108] ASTM Standard D906 - 98(2004), Standard Test Method for Strength Properties of Adhesives in Plywood Type Construction in Shear by Tension Loading, ASTM International, West Conshohocken, PA, 2004, DOI: 10.1520/D0906-98R04, www.astm.org.

[109] ASTM Standard D2339 - 98(2004), Standard Test Method for Strength Properties of Adhesives in Two-Ply Wood Construction in Shear by Tension Loading, ASTM International, West Conshohocken, PA, 2004, DOI: 10.1520/D2339-98R04, www.astm.org.

[110] ASTM Standard D7247 - 07ae1, Standard Test Method for Evaluating the Shear Strength of Adhesive Bonds in Laminated Wood Products at Elevated Temperatures, ASTM International, West Conshohocken, PA, 2007, DOI: 10.1520/D7247-07AE01, www.astm.org.

[111] ASTM Standard D4688 - 99(2005), Standard Test Method for Evaluating Structural Adhesives for Finger Jointing Lumber, ASTM International, West Conshohocken, PA, 2005, DOI: 10.1520/D4688-99R05, www.astm.org.

[112] ASTM Standard D5266 - 99(2005), Standard Practice for Estimating the Percentage of Wood Failure in Adhesive Bonded Joints, ASTM International, West Conshohocken, PA, 2005, DOI: 10.1520/D5266-99R05, www.astm.org.

[113] Stanger, A. G.; Blomquist, R. F. Block shear, cross-lap tension, and glueline cleavage methods of testing glued joints. Forest Products Journal 1965, 15, 468-474.

[114] Komatsu, K.; Sasaki, H.; Maku, T. Evaluation of Fracture Toughness for Wood-Epoxy Adhesive System under External Shear Force. Wood Research: Bulletin of the Wood Research Institute, Kyoto University 1974, 57, 10-22.

[115] Komatsu, K.; Sasaki, H.; Maku, T. Strain Energy Release Rate of Double Cantilever Beam Specimen with Finite Thickness of Adhesive Layer. Wood Research: Bulletin of the Wood Research Institute, Kyoto University 1976, 59/60, 80-92.

[116] Komatsu, K.; Sasaki, H.; Maku, T. Estimating Fracture Toughness from Nonlinear Load-Deflection Relation. Wood Research: Bulletin of the Wood Research Institute, Kyoto University 1976, 61, 25-43.

[117] White, M. S. Influence of resin penetration on the fracture toughness of wood-adhesive bonds. Ph.D. dissertation, Virginia Polytechnic Institute and State University, Blacksburg, VA, 1975.

[118] White, M. S. Influence of resin penetration on the fracture toughness of wood adhesive bonds. Wood Science 1977, 10, 6-14.

[119] White, M. S.; Green, D. W. Effect of Substrate on the Fracture-Toughness of Wood-Adhesive Bonds. Wood Science 1980, 12, 149-153.

[120] Ebewele, R.; River, B.; Koutsky, J. Tapered Double Cantilever Beam Fracture Tests of Phenolic-Wood Adhesive Joints. Part I. Development of Specimen Geometry; Effects of Bondline Thickness, Wood Anisotropy and Cure Time on Fracture Energy. Wood and Fiber 1979, 11, 197-213.

[121] Ebewele, R. O.; River, B. H.; Koutsky, J. A. Tapered Double Cantilever Beam Fracture Tests of Phenolic-Wood Adhesive Joints. Part II. Effects of Surface Roughness, the Nature of Surface Roughness, and Surface Aging on Joint Fracture Energy. Wood and Fiber 1980, 12, 40-65.

[122] Griffith, A. A. The Phenomena of Rupture and Flow in Solids. Philosophical Transactions of the Royal Society of London, Series A: Containing Papers of a Mathematical or Physical Character 1921, 221, 163-198.

[123] Irwin, G. R. Fracture Dynamics. In: Fracturing of Metals; American Society for Metals: Cleveland, OH, 1948; pp 147-166.

[124] Orowan, E. Fracture and Strength of Solids. Report of Progress in Physics 1948, 12, 185-232.

[125] Irwin, G. R. Analysis of stresses and strains near the end of a crack traversing a plate. Journal of Applied Mechanics 1957, 24, 361-364.

[126] Ruedy, T. C. The effect of grain angle orientation on the fracture toughness of wood-adhesive systems. M.S. thesis, Virginia Polytechnic Institute and State University, Blacksburg, VA, 1977.

[127] Kyokong, B.; Keenan, F. J.; Boyd, S. J. Fracture Behavior of Adhesive Joints in Poplar. Wood and Fiber Science 1986, 18, 499-525.

[128] Gagliano, J. M.; Frazier, C. E. Improvements in the fracture cleavage testing of adhesively-bonded wood. Wood and Fiber Science 2001, 33, 377-385.

[129] Conrad, M. P. C.; Smith, G. D.; Fernlund, G. Fracture of discontinuous wood-adhesive bonds. International Journal of Adhesion and Adhesives 2003, 23, 39-47.

[130] Blackman, B. R. K.; Kinloch, A. J. Protocol for the determination of the Mode I adhesive fracture energy, GIc, of structural adhesives using the double cantilever beam (DCB) and tapered double cantilever beam (TDCB) specimens. In: Fracture mechanics testing methods for polymers, adhesives and composites; Pavan, A., Moore, D. R., G., W. J., Eds.; Elsevier: Amsterdam, 2001.

[131] Ebewele, R. O.; River, B. H.; Koutsky, J. A. Wood Processing Variables and Adhesive Joint Performance. Journal of Applied Polymer Science 1986, 32, 2979-2988.

[132] Sernek, M.; Kamke, F. A.; Glasser, W. G. Comparative analysis of inactivated wood surfaces. Holzforschung 2004, 58, 22-31.

[133] Follrich, J.; Muller, U.; Gindl, W. Effects of thermal modification on the adhesion between spruce wood (Picea abies Karst.) and a thermoplastic polymer. Holz Als Roh-Und Werkstoff 2006, 64, 373-376.

[134] Ebewele, R. O.; River, B. H.; Koutsky, J. A. Relationship between Phenolic Adhesive Chemistry, Cure and Joint Performance. Part I. Effects of Base Resin Constitution and Hardener on Fracture Energy and Thermal Effects During Cure. Journal of Adhesion 1982, 14, 189-217.

[135] Mijovic, J. S.; Koutsky, J. A. Effect of Wood Grain Angle on Fracture Properties and Fracture Morphology of Wood-Epoxy Joints. Wood Science 1979, 11, 164-168.

[136] River, B. H.; Scott, C. T.; Koutsky, J. A. Adhesive joint fracture behaviour during setting and aging. Forest Products Journal 1989, 39, 23-28.

[137] Ebewele, R. O.; River, B. H.; Koutsky, J. A. Relationship between Phenolic Adhesive Chemistry and Adhesive Joint Performance: Effect of Filler Type on Fraction Energy. Journal of Applied Polymer Science 1986, 31, 2275-2302.

[138] Lim, W. W.; Mizumachi, H. Fracture toughness of adhesive joints. 2. Temperature and rate dependencies of mode I fracture toughness and adhesive tensile strength. Journal of Applied Polymer Science 1995, 57, 55-61.

[139] Lim, W. W.; Mizumachi, H. Fracture toughness of adhesive joints. 3. Temperature and rate dependencies of mode II fracture toughness and adhesive shear strength. Journal of Applied Polymer Science 1997, 63, 835-841.

CHAPTER 3

EFFECTS OF CELLULOSE NANOCRYSTALS ON PHENOL–FORMALDEHYDE ADHESIVE RESINS—PART I: RESIN RHEOLOGY

3.1. ABSTRACT

The purpose of this study was to determine the effects of cellulose nanocrystals (CNCs) on the liquid-state properties of phenol–formaldehyde (PF) resol resin. First, an aqueous 10 wt % CNC suspension, which separated upon standing into an isotropic and a chiral-nematic phase, was analyzed. The viscosity–shear rate curve of the chiral-nematic fraction exhibited a well-defined Newtonian plateau between two shear thinning regions, characteristic of textured liquid crystals. The biphasic 10 wt % CNC suspension was used to prepare CNC–resin mixtures containing 1–3 wt % CNCs. The steady-state viscosity of the PF resin itself was independent of shear rate over the entire range tested (0.2 and 2878 s^{-1}). The viscosity–shear rate curves of the CNC–resin mixtures showed a shear thinning region at lower shear rates and a Newtonian region at higher shear rates. The low-shear-rate viscosity of the resin was greatly increased by the CNCs. At very low shear rates, a second Newtonian plateau was indicated, characteristic of colloidal suspensions. The structure of the CNC–resin mixtures under quiescent conditions was analyzed by polarized light microscopy. The mixtures contained CNC aggregates, which could be disrupted by ultrasound treatment.

3.2. INTRODUCTION

Phenol–formaldehyde (PF) resins are among the most widely used wood adhesives. Because of their superior water and weather resistance, they are preferred over urea–formaldehyde resins for exterior-grade composite wood products, such as exterior-grade plywood, particleboard, and oriented strandboard (OSB) [1, 2]. One of the drawbacks of PF resins is their need for longer press times [3], compared to urea–formaldehyde resins, and many efforts have been made to accelerate PF resin cure and hardening [4-17].

Nanoparticles have the ability to cause significant property changes in composite materials at very small quantities because of their large specific surface area [18]. A comparatively inexpensive class of nanoparticles that has recently attracted attention as a polymer additive is cellulose nanocrystals (CNCs) [19]. CNCs are obtained by partial acidic degradation of cellulose microfibrils resulting in highly crystalline, nanoscale, rodlike fragments [20-24]. The properties of CNCs are strongly influenced by the cellulose source and the hydrolysis conditions, such as acid type and concentration, reaction temperature and time, and acid-to-cellulose ratio [25-31]. The average length and diameter of wood-derived CNCs, for example, are typically in the ranges 100–150 nm and 4.5–5 nm, respectively [28].

Molecular interactions across the wood–resin interface are known to catalyze the curing processes of PF resins [32-41]. Cellulose, the main component of the wood cell wall, has been found to significantly lower the activation energy of PF autocondensation reactions [42-44]. The catalytic activity of cellulose, in particular crystalline cellulose, has been attributed to the activation of the methylol groups and phenolic ortho and para positions through secondary interactions between cellulose and the methylol and phenol hydroxyl groups, respectively [32]. The ability of cellulose to accelerate PF resin cure makes CNCs an interesting candidate for applications as PF resin additive.

This study, which is the first of a series of studies investigating the effects of CNCs on PF adhesive resin, focuses on the effects of CNCs on resin rheology. The rheological properties of adhesive resins play an important role in the manufacture of composite wood products. Depending on the wood product, the resin is either roll, brush, or spray applied to the substrate, requiring different flow properties for each method [1]. Resin

viscosity governs the spreading of the resin on the wood substrate as well as the penetration of the resin into the wood cavities [45-47]. A certain degree of penetration is desired for mechanical interlocking at the resin–wood interface. However, excessive penetration results in a starved bondline and poor joint performance.

The purpose of this study was to determine the effects of CNCs on the liquid-state properties of PF resol resin. In the first part of the study, we investigated the rheological properties of a 10 wt % CNC suspension in water. The second part focused on the rheological properties of four CNC–resin mixtures, containing 0–3 wt % CNCs, based on solids content.

3.3. EXPERIMENTAL

3.3.1. Materials

Dissolving-grade softwood sulfite pulp (Temalfa 93A-A) was kindly provided by Tembec, Inc. Liquid phenol–formaldehyde resol resin (OSB core resin, 50 wt % solids content) was kindly provided by Dynea North America, now Arclin. The resin was stored frozen in 500 mL units until use. Prior to use, the resin was thawed and thoroughly mixed. Sulfuric acid (95.9%, certified ACS plus) and sodium hydroxide solution (N/10, certified) were purchased from Fisher Scientific and used as received. Deionized water (18.2 MΩ·cm) was generated from tap water with a Millipore Direct-Q 5 Ultrapure Water System.

3.3.2. Methods

3.3.2.1. Synthesis of CNCs

CNCs were prepared by sulfuric acid hydrolysis of dissolving-grade softwood sulfite pulp. Lapsheets of the pulp were cut into small pieces (Figure 3.1(a)) and milled in a Wiley Mini-Mill to pass a 60-mesh screen (Figure 3.1(b)). For the hydrolysis, 500 mL 64 wt % sulfuric acid was prepared by appropriate dilution of 95.9 wt % sulfuric acid with deionized water and added to 50 g milled pulp. The reaction mixture was stirred for 60 min at 45.5 °C in a water bath (Figure 3.1(c)). The hydrolysis was stopped by diluting the mixture with 2500 mL deionized water followed by centrifugation at 4900 rpm and 25 °C for 10 min and discarding of the supernatant. The sediment was redispersed in deionized water and centrifuged again. The sediment of the second centrifugation was transferred to regenerated cellulose dialysis tubing (Spectra/Por 4, molecular weight cut off of 12–14 kDa) and dialyzed for several days against deionized water (Figure 3.1(d)). When the pH of the dialysis water stayed constant, the suspension was filtered through Whatman 541 filter paper. The concentration of the obtained suspension (Figure 3.1(e)) was determined as follows. Aliquots of ~5–6 g were heated in an oven at 80 °C until dry (3–4 h). The concentration, calculated from the weights of the solid residues after

evaporation, was approximately 1 wt %. The suspension was subsequently concentrated to 10 wt % with a rotary evaporator (Büchi Rotavapor R-200) using a water bath temperature of 40 °C.

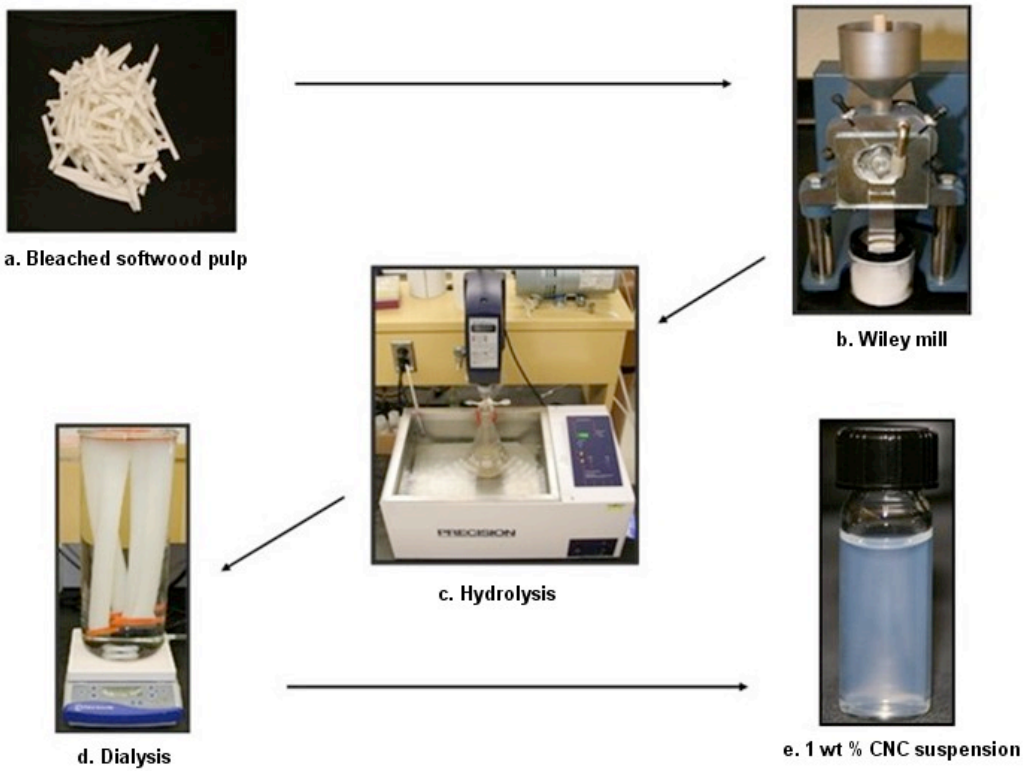

Figure 3.1. Main steps in the preparation of stable CNC suspensions by sulfuric acid hydrolysis of dissolving-grade softwood sulfite pulp.

3.3.2.2. Preparation of CNC–resin mixtures

Four CNC–resin mixtures with CNC contents of 0 wt % (PF0), 1 wt % (PF1), 2 wt % (PF2), and 3 wt % (PF3), based on total solids content, were prepared according to Figure 3.2 by slow addition of different amounts of CNC suspension (10 wt %) and deionized water under stirring (500 rpm). Stirring was continued for 10 min to ensure good mixing.

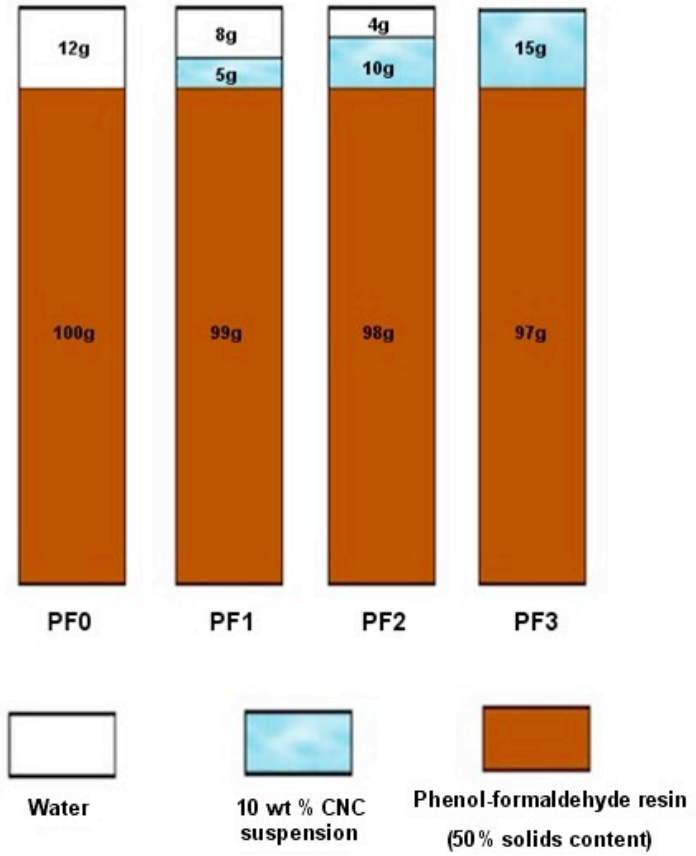

Figure 3.2. Amounts of neat PF resol resin, 10 wt % CNC suspension, and deionized water in the four studied CNC–resin mixtures.

The respective amounts of CNC suspension and deionized water were chosen to maintain an equal solids content in the four resin mixtures (Table 3.1). No fillers, extenders, or any other additives were added in this study.

Table 3.1. Composition and pH values of the four studied CNC–resin mixtures

Resin mixture	Neat resin (g)	10 wt % CNC suspension (g)	Water (g)	CNC content (wt %)	Total solids content (wt %)	pH[a]
PF0	100	0	12	0	44.64	12.30 ± 0.01
PF1	99	5	8	1	44.64	12.30 ± 0.01
PF2	98	10	4	2	44.64	12.29 ± 0.01
PF3	97	15	0	3	44.64	12.27 ± 0.02

a The pH of the 10 wt % CNC suspension was 1.85.

The pH of the resin, an important parameter during resin cure and therefore of influence to the final properties of the resin, was slightly reduced by addition of the acidic CNC suspension (pH 1.85). However, the decrease was less than 0.3% and therefore negligible. The pH of the neat resin (12.3) suggested, that the NaOH concentration was approximately 0.02 N, which is well below the concentration required to swell crystalline cellulose (2.5 N [48]). It is therefore assumed that the CNCs in the resin mixtures stayed intact and did not swell significantly.

3.3.2.3. Atomic force microscopy (AFM)

AFM images were recorded under ambient conditions in AC mode (1 Hz, 512 points/scan) with an Asylum Research MFP3D-Bio atomic force microscope mounted onto an Olympus IX71 inverted fluorescence microscope using standard aluminum-coated silicon probes (Olympus OMCL-AC160TS, nominal tip radius: < 10 nm). AFM samples were prepared by placing one drop (~10 μm) of a dilute (0.001 wt %) CNC suspensions onto a freshly cleaved mica sheet (PELCO, Ted Pella), mounted with epoxy adhesive resin onto a standard microscope slide, and allowing the drop to dry at room temperature.

3.3.2.4. Polarized light microscopy

Polarized light microscopy images were recorded with a Canon EOS 20D digital single-lens reflex camera (8.2 megapixels) mounted onto a Zeiss Axioskop 40 A POL microscope. Analysis of the CNC–resin mixtures was done immediately after preparation of the mixtures or after sonication for 5 min at 30 % output with a Sonics & Materials VC-505 ultrasonic processor (500 watts, 20 kHz). Microscopy samples were prepared by placing one drop of the resin mixture between a standard microscope slide and a cover slip.

3.3.2.5. Conductometric titration

Aqueous sodium hydroxide solution (0.005 N) was added dropwise with a Brinkmann Bottletop Buret (Model 25) at room temperature under nitrogen and stirring to 50 g of a 0.6 wt % CNC suspension in a 100 mL three-neck flask. After each drop, the conductivity of the suspension was measured with a Mettler Toledo SevenMulti S47 pH/conductivity meter with an InLab 730 conductivity probe.

3.3.2.6. Thermogravimetric analysis (TGA)

TGA of the 10 wt % CNC suspension was performed with a TA Instruments TGA Q500. Approximately 20–30 mg of suspension was placed into a platinum TGA sample pan. Thermogravimetric (TG) and derivative TG (DTG) curves between ~25 and 300 °C were recorded in Hi-Res mode using air as purge gas.

3.3.2.7. Rheological measurements

Rheological measurements on the 10 wt % CNC suspension and the resin mixtures were performed using a TA Instruments AR-1000 rheometer equipped with a stainless steel cone-and-plate geometry (40 mm diameter, 2°). After equilibration of the sample on the Peltier plate at 25 °C, the edge of the sample was sealed using silicon oil. The purpose of sealing the sample was to minimize evaporation during the experiment, which would influence the viscosity of the sample. Viscosity–shear rate profiles were measured under steady-state flow conditions between the shear rates 0.2 and 2878 s^{-1}. Ten data points were recorded per decade. The flow experiments of the resin mixtures were conducted immediately after preparation of the mixture.

3.4. RESULTS AND DISCUSSION

3.4.1. Properties of the CNCs and their aqueous suspensions

The obtained aqueous suspension of CNCs was stable, i.e. did not show particle sedimentation, and had a concentration of approximately 1 wt %. The CNC yield was approximately 20%. The morphology and size distribution of the CNCs was analyzed by AFM. Figure 3.3 shows typical AFM amplitude images of the CNCs at two different scan sizes. The particles were elongated and exhibited a wide distribution of lengths. The average dimensions of the CNCs were determined from AFM height images using the image processing capabilities of the AFM software (Wavemetrics IGOR Pro 6). The obtained average length, width, and height were 119.8 ± 68.2 nm, 15.3 ± 14.0 nm, and 3.8 ± 0.6 respectively, in good agreement with previous studies reporting lengths of 100–300 nm and heights of 3–5 nm for similarly prepared CNCs [8, 21]. The width of the particles was not measured in those studies and assumed to be equal to the particle height.

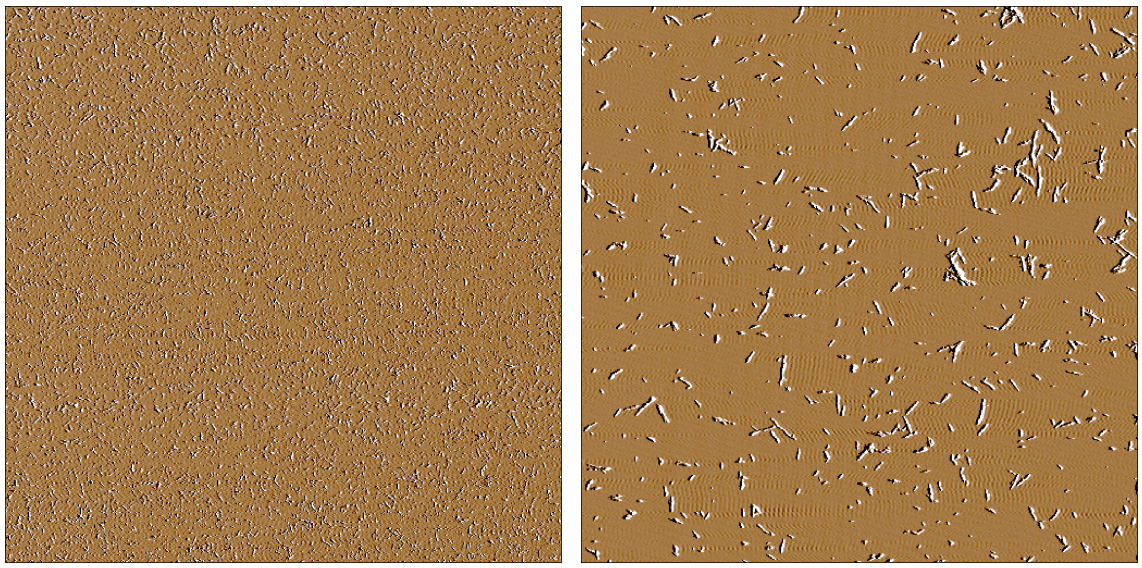

Figure 3.3. AFM amplitude images of CNCs at different scan sizes: 40 µm × 40 µm (left), 10 µm × 10 µm (right).

CNCs prepared by sulfuric acid hydrolysis are known to possess a negative surface charge. The surface charge is the result of partial esterification of the surface hydroxyl groups by sulfuric acid during the hydrolysis. In aqueous suspension, these sulfate groups are dissociated and carry a negative charge, which stabilizes the suspension through electrostatic repulsion among the particles. The sulfate group density in our sample was determined by conductometric titration. Figure 3.4 shows a typical conductometric titration curve. The initial linear decrease in conductivity was due to the neutralization of the H^+ counter ions of the $–OSO_3^-$ groups and substitution with Na^+ ions, which have a lower ionic mobility and therefore molar conductivity. Once the H^+ ions had been neutralized, the conductivity increased upon further addition of NaOH due to the increase in ion concentration. The sulfate group density, calculated from the NaOH volume at the equivalence point (16.4 mL) and the amount of CNCs present in the suspension, was 273 mmol/kg.

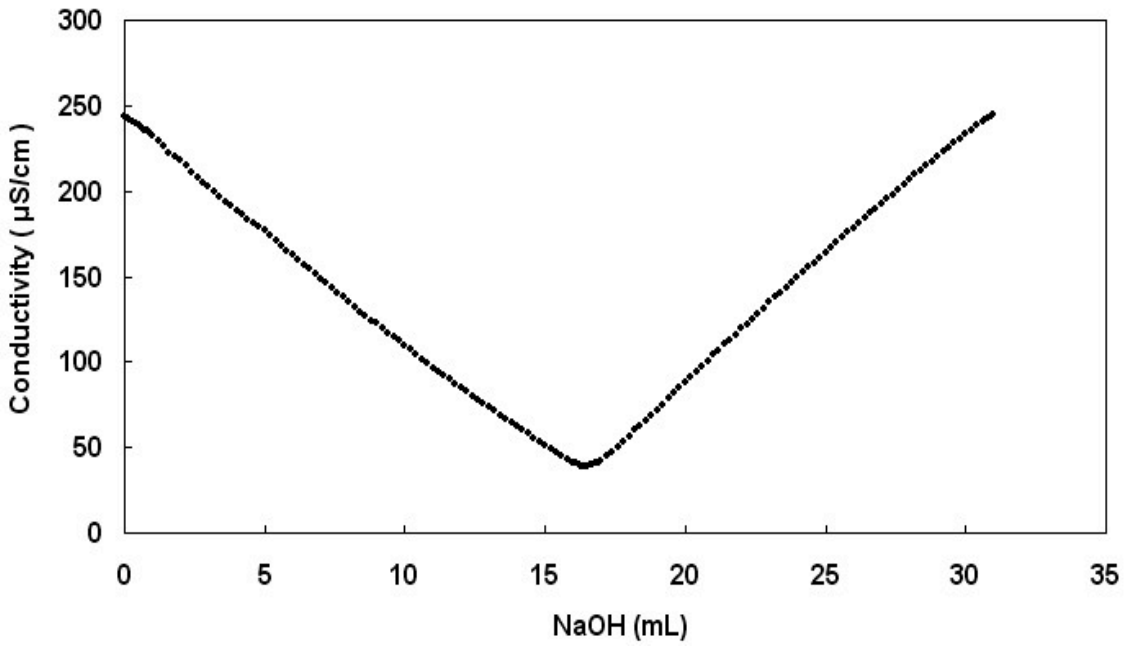

Figure 3.4. Conductometric titration curve obtained by titrating 50 g of a 0.6 wt % CNC suspension with 0.005 N NaOH.

Surface sulfate groups have been shown to be detrimental to the thermal stability of CNCs [49]. The potential application of CNCs in thermosetting adhesive resins requires the particles to be stable at or above the curing temperature of the resin. To assess the thermal stability of the CNCs, we measured their degradation temperature by TGA. Figure 3.5 shows the TG and DTG curves of the CNCs in aqueous 10 wt % suspension. The initial weight loss, from 100% to ~10%, during heating to 120 °C was due to the evaporation of water. Degradation of the nanoparticles occurred between 140 and 225 °C, with a maximum weight loss rate at 162 °C. The observed degradation temperature was much lower than those reported by Roman and Winter [49], of which the lowest was 226 °C for a sulfate group density of 73 mmol/kg. The difference could be due to the almost four times higher sulfate group density in our sample (273 mmol/kg). However, the experimental differences with respect to the cellulose starting material, TGA sample preparation, and TGA heating rate are also a likely cause for the observed difference.

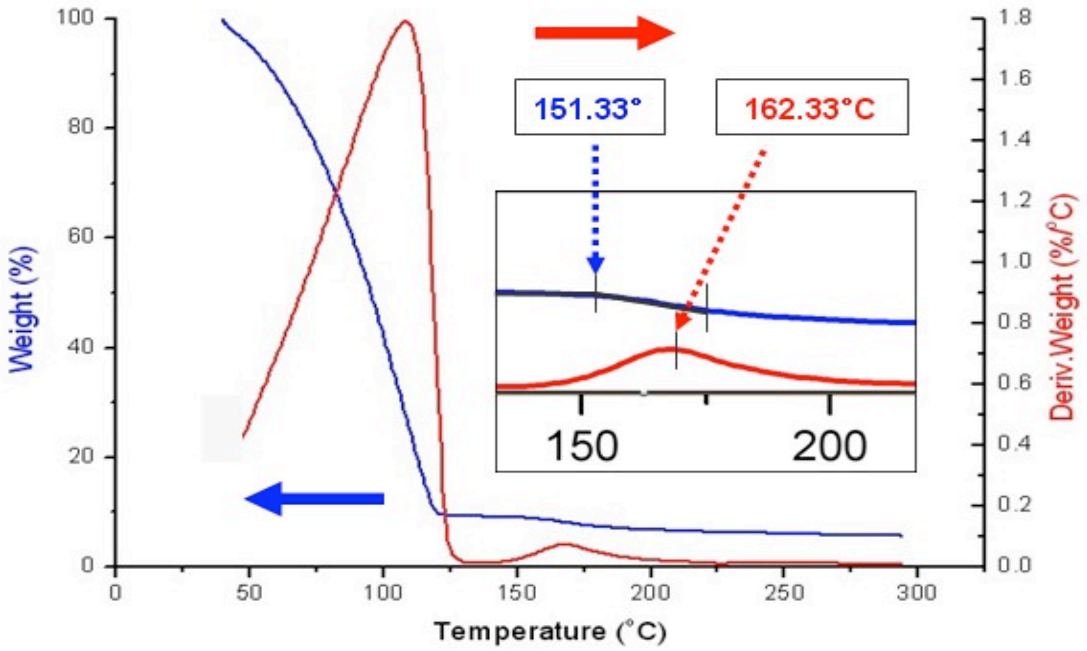

Figure 3.5. TG and DTG curves of a 10 wt % CNC suspension obtained by sulfuric acid hydrolysis of bleached softwood pulp (Hi-Res mode in air).

Before addition to the PF resin, the CNC suspension was concentrated to 10 wt % in order to minimize dilution of the resin. Figure 3.6 illustrates the appearance of the CNC suspension before and after concentration. At a concentration of 10 wt %, the suspension exhibited liquid crystalline optical properties, as illustrated in Figure 3.6 right. The formation of liquid crystalline phases by CNC suspensions has been studied extensively [27, 28, 50-64].

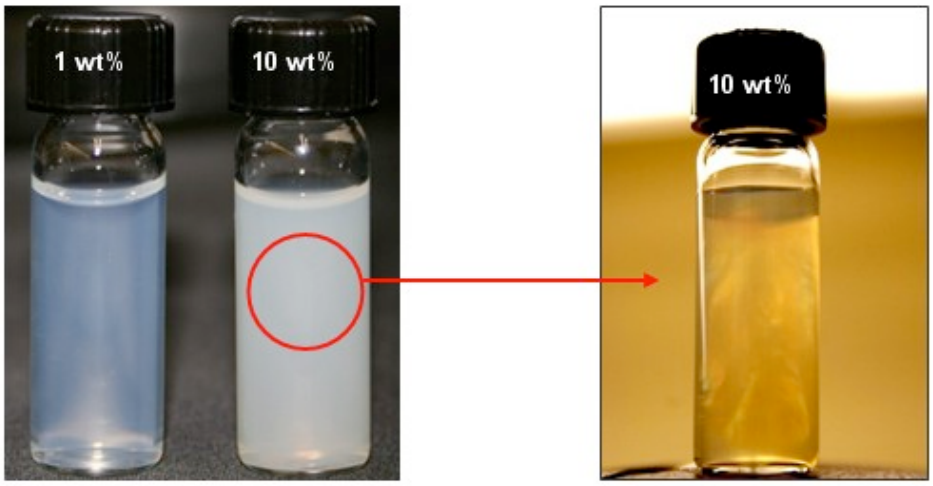

Figure 3.6. CNC suspension at 1 and 10 wt % (left) and liquid crystalline optical properties of 10 wt % suspension (right).

Liquid crystalline phases of CNC suspensions most commonly have a chiral nematic structure [27, 51-56, 59, 64-66]. A chiral nematic structure is a quasi-layered structure in which the anisometric, elongated molecules or, in this case, nanoparticles are oriented parallel to each other within the pseudo-layers, and the preferred orientation of each pseudo-layer is rotated slightly with respect to the adjacent one, resulting in a helicoidal arrangement of the particles. The driving force for alignment of the rod-like particles within the pseudo-layers are excluded volume effects and an increase in translational entropy at the expense of the orientational entropy of the system [67]. The rod density at which alignment occurs depends on the aspect ratio, i.e. ratio of length to diameter, of the rods. Consequently, in a polydisperse system with a distribution of

lengths, alignment of the rod-like particles occurs over a concentration range and is headed off by the longest rods with the shorter rods following at higher concentrations. A concentration of 10 wt % in our CNC suspension was above the limit for alignment of the longer CNCs but below the limit of the shorter ones. As a result, the suspension separated upon standing into an upper isotropic phase, with random orientation of the CNCs, and a lower chiral-nematic phase, containing the longer CNCs (Figure 3.7 left). The chiral-nematic fraction of the suspension exhibited the typical iridescence properties (Figure 3.7 right).

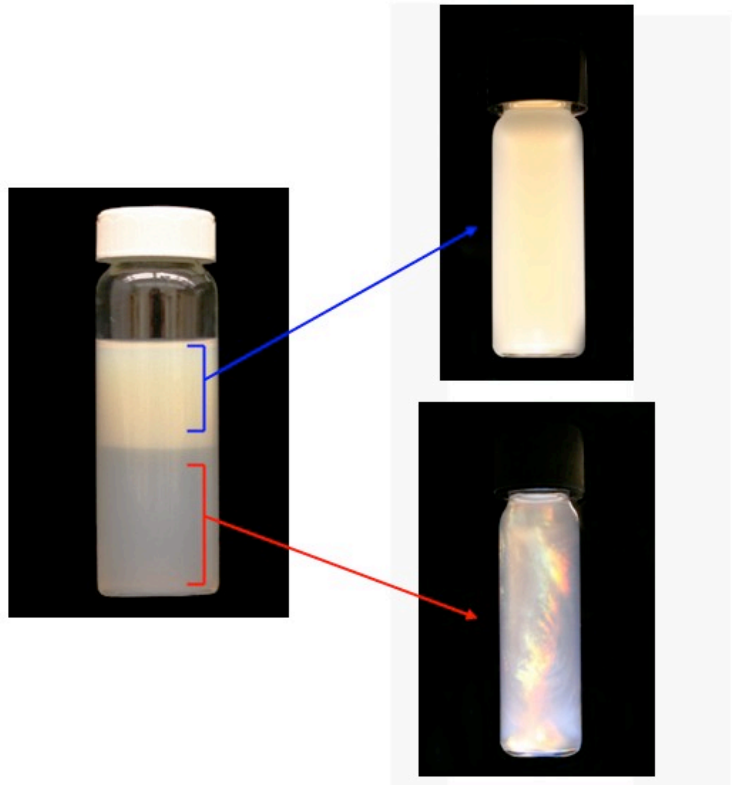

Figure 3.7. Biphasic 10 wt % CNC suspension (left), isotropic fraction (top right), and chiral-nematic fraction (bottom right).

To understand the effect of CNCs on the rheological behavior of the resin, we analyzed the rheological properties of the 10 wt % CNC suspension. Figure 3.8 shows the steady-state shear viscosity of the biphasic 10 wt % CNC suspension and of the isotropic and chiral-nematic fractions as a function of shear rate.

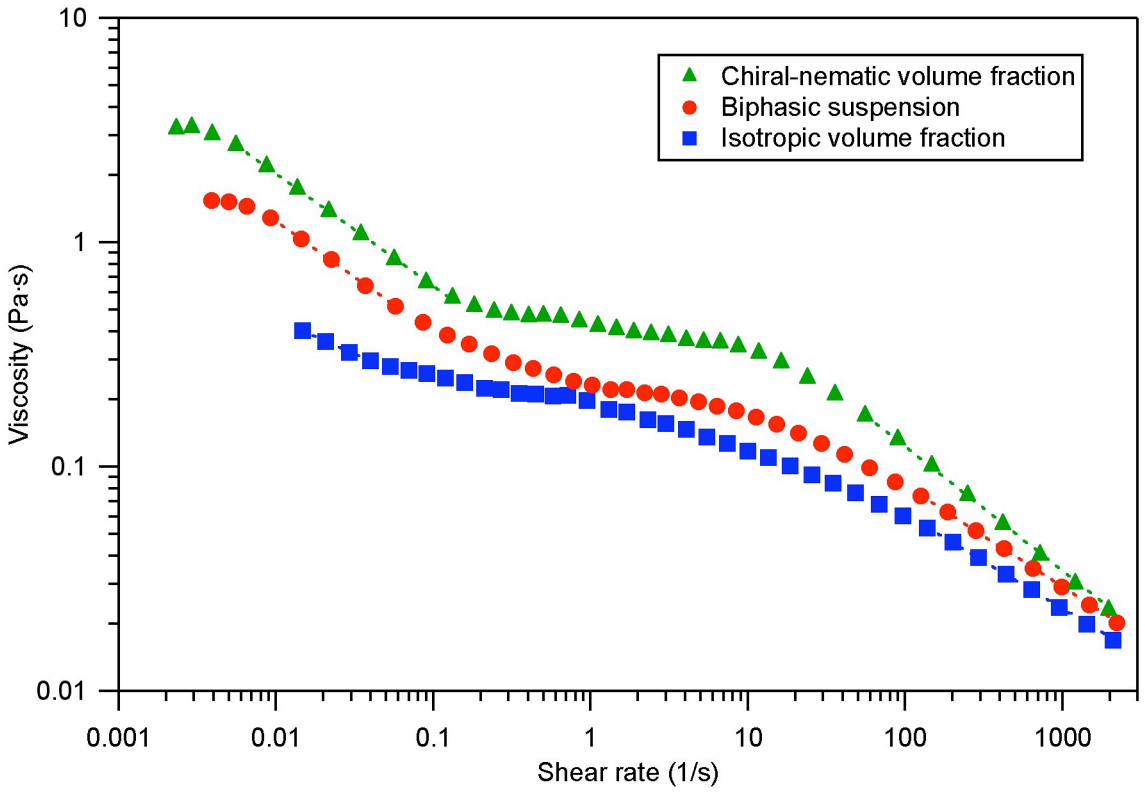

Figure 3.8. Steady-state viscosity vs. shear rate curves for the biphasic 10 wt % CNC suspension and its isotropic and chiral-nematic fractions. The dashed lines are power law fits.

The viscosity–shear rate curve of the chiral-nematic fraction (green curve in Figure 3.8) showed three distinct regions. At low (< 0.1 s^{-1}) and high (> 10 s^{-1}) shear rates, the suspension exhibited shear thinning, i.e. the viscosity decreased with increasing shear rate. At intermediate shear rates, the suspension exhibited a Newtonian plateau where the viscosity was independent of shear rate. Similar viscosity curves were observed by Orts *et al.* for softwood-derived CNCs of 280 nm length at a concentration of 5 wt % [68, 69] and by De Souza Lima and Borsali for cotton-derived CNCs at a concentration of 2.7 wt % (length not specified) [70].

This type of viscosity curve, consisting of a Newtonian plateau sandwiched between two shear-thinning regions, has been controversially proposed by Onogi and Asada to be universal for liquid crystalline systems [71]. Liquid crystalline polymers, in

particular, have been found to frequently exhibit at least two of the three flow regions. The rheology of liquid crystalline polymers and theoretical models for the underlying mechanisms have been reviewed by several authors [72-74]. The dynamical phenomena responsible for Region II, Onogi and Asada's terminology for the Newtonian plateau, and Region III, the high-shear shear-thinning region, are fairly well understood and predicted by current theories. In Region II, shear forces are believed to cause only minor deformations but no major changes in the fluid's microstructure. The shear-thinning behavior of Region III is commonly accepted to be due to the alignment of the rod-like molecules or, in this case, particles with the shear direction. Alignment of CNCs with the direction of shear at the transition from Region II to Region III has been demonstrated in small angle scattering studies [68, 69, 75]. Region I, the low-shear shear-thinning region, is the least understood of the three viscosity regions. It is commonly believed to be due to a complex supramolecular microstructure, or texture, disruptable by shear forces. The viscosity–shear rate behavior in Region I has been reported to strongly depend on the shear history of the sample, possibly explaining why it is only observed in some studies and not in others. The microstructure responsible for Region I is often described as a polydomain structure, consisting of finite domains with a more or less defect-free structure. Yet, the exact nature of these domains and their boundaries is ill defined. An alternative concept, based on a network of local defects (disclinations) in the liquid crystalline structure, sensitive to shear forces, is gaining broader acceptance [76, 77].

Theoretical models, based on the suspension-like concept of finite domains suspended in a medium, have been able to qualitatively describe the flow behavior of textured liquid crystalline systems [74]. Suspension-like behavior was discernible in Figure 3.8 in the curves of the biphasic suspension and chiral-nematic fraction by a rudimentary low-shear-rate Newtonian plateau.

A comparison of the three curves in Figure 3.8 revealed that the three viscosity regions were best defined in the chiral-nematic fraction, containing the longest CNCs. For the isotropic fraction, containing shorter CNCs, Region I and II were less obvious and Region III extended to lower shear rates (~1 s^{-1}). At low and intermediate shear rates, the viscosity of the chiral-nematic fraction was significantly higher than that of the

isotropic fraction. The viscosity values of the three suspensions at a shear rate of 1 s^{-1} are listed in Table 3.2. At this shear rate the viscosity of the chiral-nematic fraction was more than twice as high as that of the isotropic fraction. However, due to the more pronounced shear thinning in Region III, the viscosity of the chiral-nematic fraction approached that of the isotropic fraction at the highest shear rates. The biphasic suspension exhibited a behavior intermediate between those shown by the isotropic and chiral-nematic fractions.

The shear thinning behavior of Regions I and III can be fitted by a simple power law of the form

$$\eta = K\dot{\gamma}^{n-1} \qquad [3.1]$$

where K is the consistency coefficient, $\dot{\gamma}$ is the shear rate, and n is the flow index. K represents the predicted viscosity at a shear rate of 1 s^{-1}. The flow index takes on values between 0 to 1 and is a measure for the extent of deviation from Newtonian behavior, with $n = 1$ representing the Newtonian limit. Several authors reported a flow index of 0.5 for liquid crystalline polymers for Region I [78-80]. The K and n values for the three suspensions for Regions I and III are listed in Table 3.2. The n values for the biphasic suspension and chiral-nematic fraction were both 0.50, in good agreement with the literature. The n values for the isotropic fraction were higher than those for the other two suspensions indicating a smaller deviation from Newtonian behavior.

Table 3.2. Consistency coefficient and flow index values for the biphasic CNC suspension and its chiral-nematic and isotropic fractions in the high and low shear flow regions, and viscosity values at a shear rate of 1 s^{-1}

Suspension	Viscosity at 1 s^{-1} (Pa·s)	Consistency coefficient K (Pa·s^n)		Flow index n	
		Low shear rates	High shear rates	Low shear rates	High shear rates
Chiral-nematic	0.43	0.20 ± 0.00	1.57 ± 0.04	0.50 ± 0.00	0.45 ± 0.01
Biphasic	0.23	0.13 ± 0.00	0.66 ± 0.01	0.50 ± 0.01	0.55 ± 0.00
Isotropic	0.19	0.11 ± 0.00	0.43 ± 0.01	0.69 ± 0.01	0.58 ± 0.00

3.4.2. Properties of the resin mixtures

Four CNC–resin mixtures with CNC contents of 0–3 wt %, based on total solids content, were prepared by addition of the 10 wt % CNC suspension, containing both fractions, after homogenization by shaking, to the resin. Figure 3.9 shows the steady-state shear viscosity, η, of the four resin mixtures as a function of shear rate. The neat resin (PF0) exhibited Newtonian behavior over the entire range of shear rates. In contrast, the resin mixtures containing CNCs exhibited a shear-thinning region at low shear rates and a Newtonian region at high shear rates.

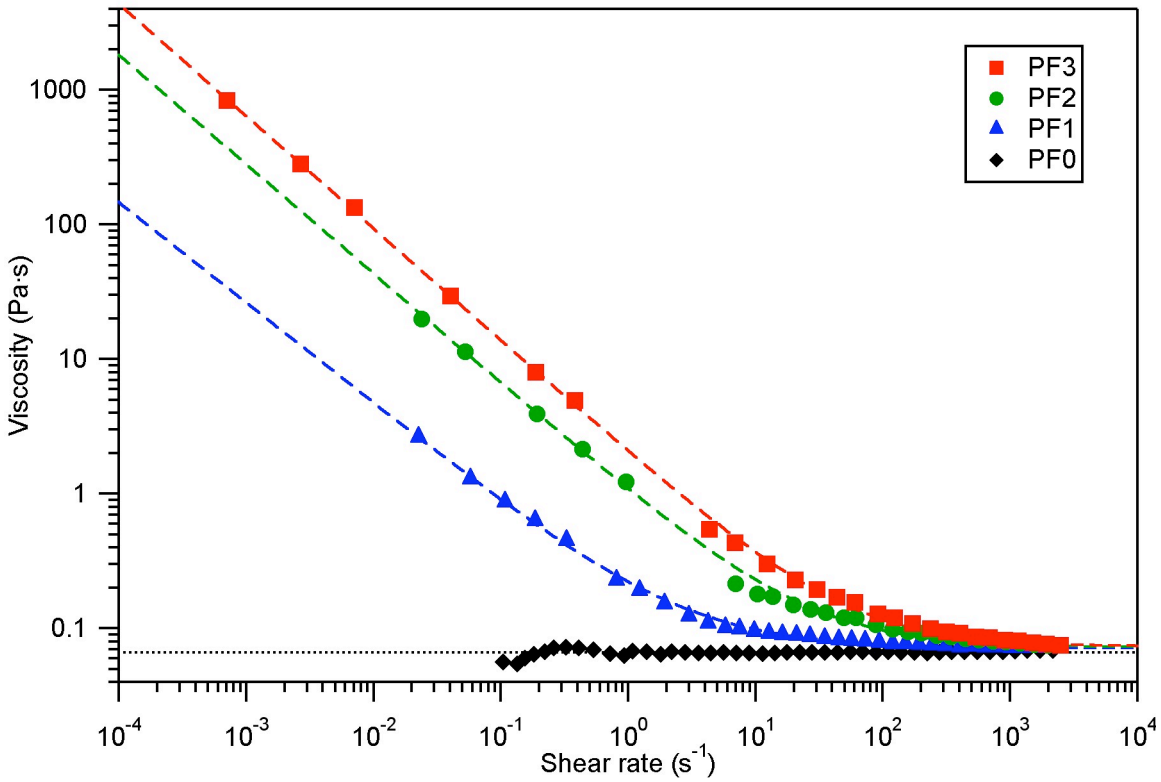

Figure 3.9. Steady-state viscosity of the four resin mixtures as a function of shear rate. The dashed lines are fits of the Sisko model. The dotted line is a zero slope linear fit of the PF0 data.

The flow behavior of the resin mixtures containing CNCs was well described by the Sisko model [81] (dashed lines in Figure 3.9):

$$\eta = \eta_\infty + K_S\dot{\gamma}^{n_S-1} \quad [3.1]$$

where η_∞ is the infinite shear rate viscosity, K_S is the consistency coefficient, $\dot{\gamma}$ is the shear rate, and n_S is the flow index. K_S represents the difference between the viscosity at 1 s^{-1} and η_∞. The values for the three parameters of the Sisko model obtained for the different resin mixtures are listed in Table 3.3.

Table 3.3. Sisko model parameters with standard deviations

Resin mixture	Infinite shear rate viscosity η_∞ (Pa·s)	Consistency coefficient K_S (Pa·s^n)	Flow index n_S
PF0[1]	0.066[1] ± 0.000	–[1]	–[1]
PF1	0.071 ± 0.003	0.15 ± 0.00	0.25 ± 0.01
PF2	0.072 ± 0.008	1.03 ± 0.02	0.19 ± 0.01
PF3	0.073 ± 0.024	2.02 ± 0.04	0.17 ± 0.01

[1] Fitted with a linear model of zero slope ($\eta = \eta_\infty$).

The infinite shear rate viscosity was statistically the same for all four resin mixtures, which meant that the viscosity of the resin mixtures containing CNCs approached that of PF0 at high shear rates. The flow index decreased with increasing CNC content, indicating a more pronounced deviation from Newtonian behavior at higher CNC contents. It should be noted that at shear rates below approximately 1 s^{-1}, the viscosity of PF1 exceeded that of the 10 wt % CNC suspension despite the approximately twenty times lower CNC concentration. At a shear rate of 0.01 s^{-1}, the viscosity of PF3 exceeded that of PF0 by almost two orders of magnitude.

Figure 3.10 shows the shear rate dependence of the shear stress for the four resin mixtures. For PF0, that dependence was well described by the Newton model (black dotted line in Figure 3.10). For PF3, the shear rate dependence of the shear stress was fitted by two models: the Bingham model (dashed line) and the Ostwald–de Waele model (dash-dotted line).

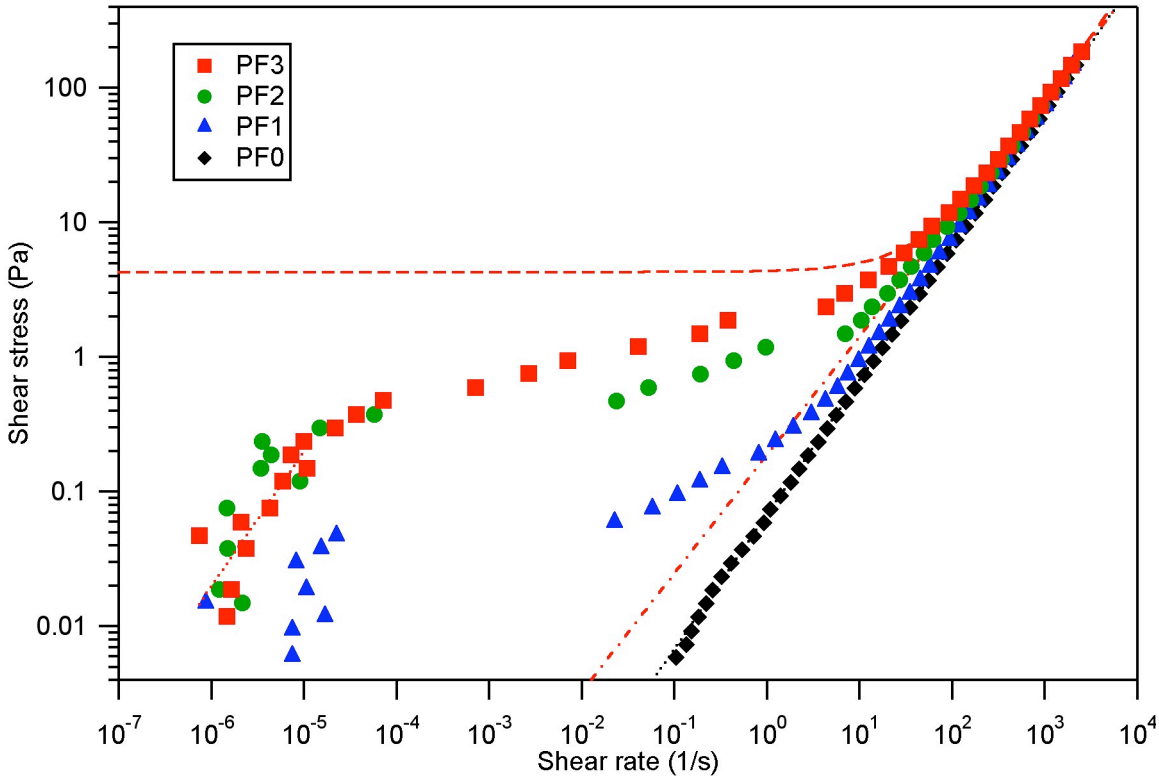

Figure 3.10. Shear rate dependence of the shear stress for the four resin mixtures. The dotted lines are fits of the Newton model. The dashed line is a fit of the Bingham model to the high-shear data for PF3 (> 0.01 s^{-1}). And the dash-dotted line is a fit of the Ostwald–de Waele model to the high-shear data for PF3 (> 0.01 s^{-1}).

The Bingham model [82] is simply the Newton model with the addition of a yield stress τ_0:

$$\tau = \tau_0 + \eta_p \dot{\gamma} \qquad [3.2]$$

The factor η_p is the Bingham plastic viscosity. The Ostwald–de Waele model [83, 84] is a simple power law and describes shear-thinning ($n < 1$), shear-thickening ($n > 1$), and Newtonian ($n = 1$) fluids that do not exhibit a yield stress:

$$\tau = K\dot{\gamma}^n \qquad [3.2]$$

Both models were able to predict the behavior at high shear rates (> 100 s^{-1}) but failed to correctly describe the behavior at low shear rates. The same was true in the case of PF1 and PF2. The fitted curves for PF1 and PF2 have been omitted for clarity. Thus, the resin mixtures containing CNCs exhibit a more complex flow behavior than a simple Bingham or Ostwald–de Waele fluid.

When looking at the data in Figure 3.10, three regions become apparent: a Newtonian region at high shear rates, a power-law region at intermediate shear rates, and a third region at low shear rates. The Newtonian region and the power-law region have already been identified in the viscosity curves of the resin mixtures (Figure 3.8). The third region, which has been omitted in Figure 3.9, could be another Newtonian region; however, the data is too noisy to be conclusive. A fit of the Newton model to the PF3 data at low shear rates is shown in Figure 3.10 (red dotted line). A low-shear Newtonian region is frequently observed for colloidal suspensions, and polymer melts and solutions [85]. In this region, the shear rate is too low to disrupt the structure of the fluid.

The structure of the resin mixtures under quiescent conditions was studied by polarized light microscopy. Polarized light microscopy enables the distinguishing of optically isotropic regions in the sample, which appear black, from optically anisotropic regions, which appear bright. CNCs are too small to be seen by optical microscopy. However, aggregates of CNCs may be seen if they have an anisotropic structure, i.e. if they have a preferred orientation of CNCs. Figure 3.11 (a) shows micrographs of the resin mixtures PF1, PF2, and PF3 immediately after preparation of the mixtures. The resin mixtures exhibited bright areas, indicating optically anisotropic regions, most likely due to ordered aggregates of CNCs. The bright areas appeared to be more numerous at higher CNC content. In contrast, the 10 wt % CNC suspension appeared completely homogeneous (not shown), indicating that the aggregates in the resin mixtures had formed upon addition of the CNC suspension to the resin.

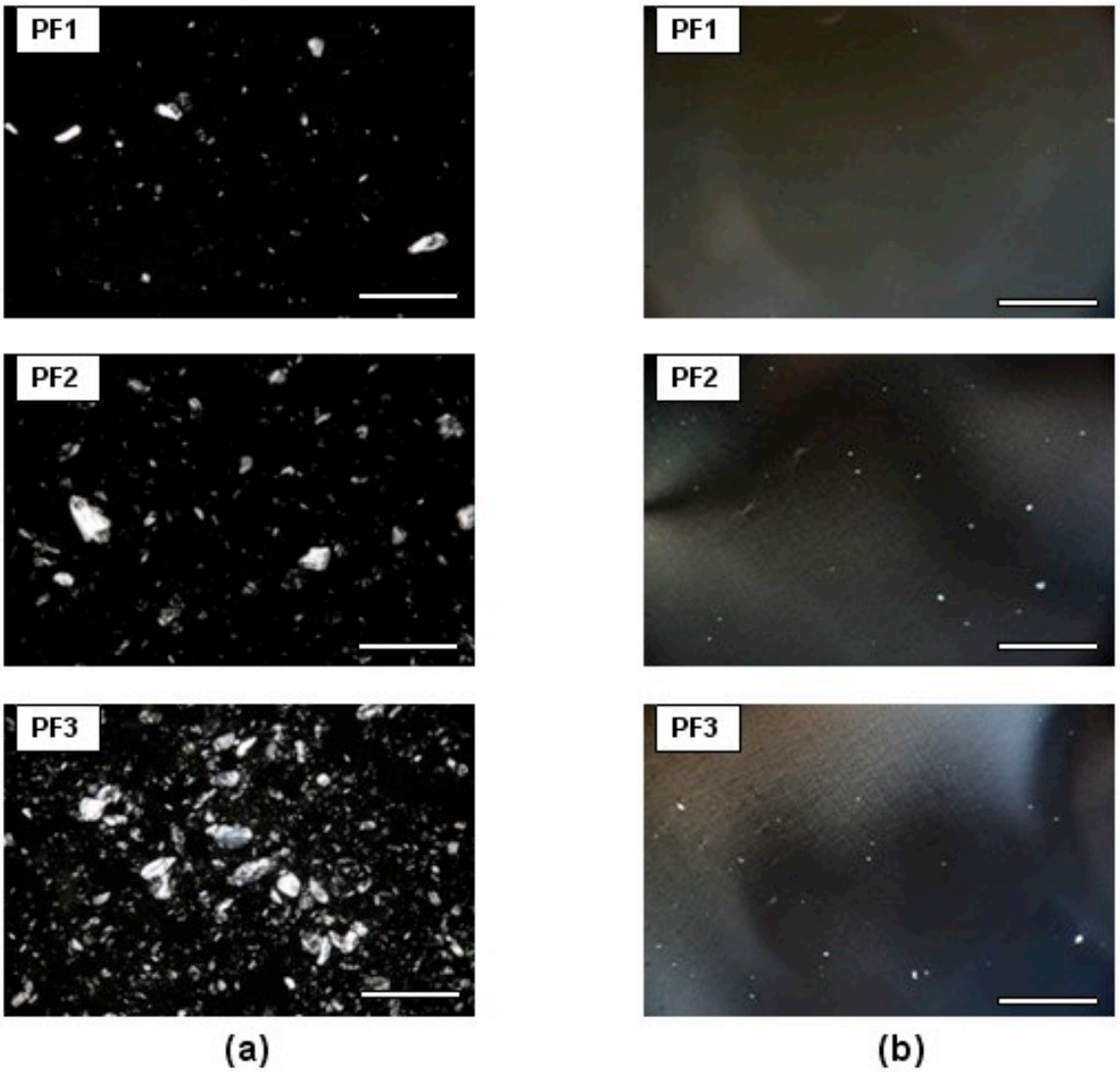

Figure 3.11. Polarized-light microscopy images of the resin mixtures PF1, PF2, and PF3 immediately after preparation of the mixture (a) and after a 5 min. ultrasound treatment (b). (Scale bar: 0.5 mm)

The bright areas in the images were quantified using image processing software (Wavemetrics Igor Pro 6) and the results of this analysis are shown in Figure 3.12 and Table 3.4. The image analysis confirmed that both the number of bright areas and the total bright area in the micrographs increased with the CNC content. In the image of PF3, bright areas accounted for 26.2% of the image.

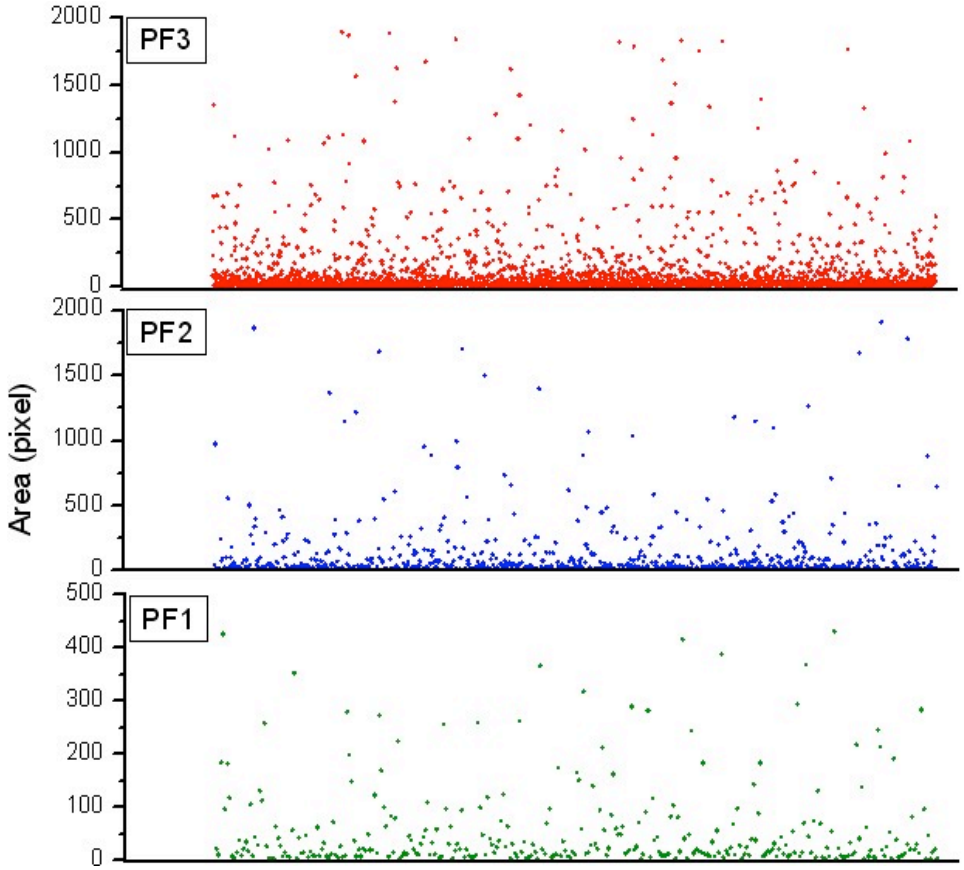

Figure 3.12. Sizes of the individual bright areas in the polarized light micrographs of the resin mixtures PF1, PF2, and PF3. Each data point represents one area delineated by the image analysis software. Data points are spread artificially along the x-axis for clarity.

Table 3.4. Statistical data from the analysis of the polarized light micrographs of the resin mixtures PF1, PF2, and PF3

	PF1	PF2	PF3
Number of individual bright areas	329	804	2,626
Average size of bright areas (pixel)	144.9	194.9	198.3
Total bright area (pixel)	47,807	156,894	521,045
Total bright area (%)[a]	2.4	7.9	26.2

[a] The size of the original images was (1,728 × 1,152) pixels

The CNC aggregates manifested themselves in form of “gel beads”, visible in thin layers of the resin under low-shear conditions. To investigate the nature of these aggregates, we subjected the resin mixtures to a 5 min ultrasound treatment. After the treatment, aggregates were no longer observed (Figure 3.11 (b)), indicating that ultrasound could overcome the forces holding these aggregates together. The texture, discernible in the images of PF2 and PF3 after ultrasound treatment, indicated a certain degree of structure in the sonicated resin mixtures.

3.5. CONCLUSIONS

With respect to the objective of this study, the conclusions are:

- Addition of CNCs causes a transition from Newtonian to non-Newtonian flow behavior in the resin;
- CNC-containing resins are shear thinning at low shear rates but exhibit Newtonian behavior at high shear rates;
- CNCs cause a strong increase in the low-shear-rate viscosity of the resin, and the effect is enhanced with increasing CNC content;
- The flow behavior of CNC containing resins differs strongly from that of a biphasic aqueous CNC suspension;
- CNC containing resins possibly exhibit Newtonian flow behavior at very low shear rates, characteristic of colloidal suspensions;
- CNC-containing resins are heterogeneous in nature and exhibit CNC aggregates, which can be disrupted by ultrasound treatment.

3.6. REFERENCES

[1] Pizzi, A. Phenolic Resin Adhesives. In: Handbook of Adhesives Technology; 2nd ed.; Pizzi, A., Mittal, K. L., Eds.; Marcel Dekker: New York, 2003; pp 541-571.

[2] Gardziella, A.; Pilato, L.; Knop, A. Phenolic Resins: Chemistry, Applications, Standardization, Safety and Ecology. 2nd ed.; Springer: Heidelberg, Germany, 1999.

[3] Dunky, M. Adhesives in the Wood Industry. In: Handbook of Adhesives Technology; 2nd ed.; Pizzi, A., Mittal, K. L., Eds.; Marcel Dekker: New York, 2003; pp 887-956.

[4] Pizzi, A.; Stephanou, A. Phenol-Formaldehyde Wood Adhesives under Very Alkaline Conditions. 2. Esters Curing Acceleration, Its Mechanism and Applied Results. Holzforschung 1994, 48, 150-156.

[5] Tohmura, S.; Higuchi, M. Acceleration of the cure of phenolic resin adhesives .6. Cure-accelerating action of propylene carbonate. Mokuzai Gakkaishi 1995, 41, 1109-1114.

[6] Pizzi, A.; Garcia, R.; Wang, S. On the networking mechanisms of additives-accelerated phenol-formaldehyde polycondensates. Journal of Applied Polymer Science 1997, 66, 255-266.

[7] Zhao, C. H.; Pizzi, A.; Garnier, S. Fast advancement and hardening acceleration of low-condensation alkaline PF resins by esters and copolymerized urea. Journal of Applied Polymer Science 1999, 74, 359-378.

[8] Park, B. D.; Riedl, B.; Hsu, E. W.; Shields, J. Differential scanning calorimetry of phenol-formaldehyde resins cure-accelerated by carbonates. Polymer 1999, 40, 1689-1699.

[9] Zhao, C. H.; Pizzi, A.; Kuhn, A.; Garnier, S. Fast advancement and hardening acceleration of low condensation alkaline phenol-formaldehyde resins by esters and

copolymerized urea. II. Esters during resin reaction and effect of guanidine salts. Journal of Applied Polymer Science 2000, 77, 249-259.

[10] Lorenz, L. F.; Conner, A. C.; Fpp, F. P. P. Accelerated cure of phenol-formaldehyde by the addition of cure accelerators: Studies with model compounds. S Lake Tahoe, Nv, Jun 22-23, 2000; pp 391-395.

[11] Park, B. D.; Riedl, B. C-13-NMR study on cure-accelerated phenol-formaldehyde resins with carbonates. Journal of Applied Polymer Science 2000, 77, 1284-1293.

[12] Park, B. D.; Riedl, B.; Hsu, E. W.; Shields, J. Application of cure-accelerated phenol-formaldehyde (PF) adhesives for three-layer medium density fiberboard (MDF) manufacture. Wood Science and Technology 2001, 35, 311-323.

[13] Conner, A. H.; Lorenz, L. F.; Hirth, K. C. Accelerated cure of phenol-formaldehyde resins: Studies with model compounds. Journal of Applied Polymer Science 2002, 86, 3256-3263.

[14] Kamo, N.; Okamura, H.; Higuchi, M.; Morita, M. Condensation reactions of phenolic resins V: cure-acceleration effects of propylene carbonate. Journal of Wood Science 2004, 50, 236-241.

[15] Dukarska, D.; Lecka, J. Optimization of the process of pressing particleboards by means of modifying phenol-formaldehyde resin with amide polymers. Holz Als Roh-Und Werkstoff 2006, 64, 403-409.

[16] Kamo, N.; Tanaka, J.; Higuchi, M.; Kondo, T.; Morita, M. Condensation reactions of phenolic resins - VII: catalytic effect of sodium bicarbonate for the condensation of hydroxymethylphenols. Journal of Wood Science 2006, 52, 325-330.

[17] Lei, H.; Pizzi, A.; Despres, A.; Pasch, H.; Du, G. B. Ester acceleration mechanisms in phenol-formaldehyde resin adhesives. Journal of Applied Polymer Science 2006, 100, 3075-3093.

[18] Paul, D. R.; Robeson, L. M. Polymer nanotechnology: Nanocomposites. Polymer 2008, 49, 3187-3204.

[19] Samir, M. A. S. A.; Alloin, F.; Dufresne, A. Review of recent research into cellulosic whiskers, their properties and their application in nanocomposite field. Biomacromolecules 2005, 6, 612-626.

[20] Rånby, B. G.; Ribi, E. Über den Feinbau der Zellulose. Experientia 1950, 6, 12-14.

[21] Rånby, B. G. The colloidal properties of cellulose micelles. Discussions of the Faraday Society 1951, 11, 158-64, discussion 208-213.

[22] Rånby, B. G. The cellular micelles. Tappi Journal 1952, 35, 53-58.

[23] Immergut, E. A.; Rånby, B. G. Heterogeneous acid hydrolysis of native cellulose fibers. Industrial & Engineering Chemistry 1956, 48, 1183-1189.

[24] Battista, O. A.; Coppick, S.; Howsmon, J. A.; Morehead, F. F.; Sisson, W. A. Level-off degree of polymerization. Relation to polyphase structure of cellulose fibers. Industrial & Engineering Chemistry 1956, 48, 333-335.

[25] Rånby, B. G. Physicochemical investigations on animal cellulose (Tunicin). Arkiv för Kemi 1952, 4, 241-248.

[26] Rånby, B. G. Physicochemical investigations on bacterial cellulose. Arkiv för Kemi 1952, 4, 249-255.

[27] Dong, X. M.; Revol, J.-F.; Gray, D. G. Effect of microcrystallite preparation conditions on the formation of colloid crystals of cellulose. Cellulose 1998, 5, 19-32.

[28] Beck-Candanedo, S.; Roman, M.; Gray, D. G. Effect of Reaction Conditions on the Properties and Behavior of Wood Cellulose Nanocrystal Suspensions. Biomacromolecules 2005, 6, 1048-1054.

[29] Araki, J.; Wada, M.; Kuga, S.; Okano, T. Flow properties of microcrystalline cellulose suspension prepared by acid treatment of native cellulose. Colloids and Surfaces, A: Physicochemical and Engineering Aspects 1998, 142, 75-82.

[30] Araki, J.; Wada, M.; Kuga, S.; Okano, T. Influence of surface charge on viscosity behavior of cellulose microcrystal suspension. Journal of Wood Science 1999, 45, 258-261.

[31] Elazzouzi-Hafraoui, S.; Nishiyama, Y.; Putaux, J.-L.; Heux, L.; Dubreuil, F.; Rochas, C. The Shape and Size Distribution of Crystalline Nanoparticles Prepared by Acid Hydrolysis of Native Cellulose. Biomacromolecules 2008, 9, 57-65.

[32] Pizzi, A.; Mtsweni, B.; Parsons, W. Wood-induced catalytic activation of PF adhesives autopolymerization vs PF wood covalent bonding. Journal of Applied Polymer Science 1994, 52, 1847-1856.

[33] Lu, X.; Pizzi, A. Curing conditions effects on the characteristics of thermosetting adhesives-bonded wood joints - Part 1: Substrate influence on TTT and CHT curing diagrams of wood adhesives. Holz als Roh- und Werkstoff 1998, 56, 339-346.

[34] Pizzi, A.; Lu, X.; Garcia, R. Lignocellulosic substrates influence on TTT and CHT curing diagrams of polycondensation resins. Journal of Applied Polymer Science 1999, 71, 915-925.

[35] Pizzi, A.; Zhao, C.; Kamoun, C.; Heinrich, H. TTT and CHT curing diagrams of water-borne polycondensation resins on lignocellulosic substrates. Journal of Applied Polymer Science 2001, 80, 2128-2139.

[36] He, G.; Riedl, B. Curing kinetics of phenol formaldehyde resin and wood-resin interactions in the presence of wood substrates. Wood Science and Technology 2004, 38, 69-81.

[37] He, G.; Yan, N. Effect of wood on the curing behavior of commercial phenolic resin systems. Journal of Applied Polymer Science 2005, 95, 185-192.

[38] He, G.; Yan, N. Effect of wood species and molecular weight of phenolic resins on curing behavior and bonding development. Holzforschung 2005, 59, 635-640.

[39] Johnson, A. C.; Yan, N. Characterizing local curing of liquid phenol-formaldehyde resin on wood surfaces using micro-thermal analysis. Wood Adhesives 2005,

[Proceedings Symposium], San Diego, CA, United States, Nov. 2-4, 2005 2006, 171-175.

[40] Lei, Y.; Wu, Q. Cure kinetics of aqueous phenol-formaldehyde resins used for oriented strandboard manufacturing: effect of wood flour. Journal of Applied Polymer Science 2006, 102, 3774-3781.

[41] Lei, Y.; Wu, Q.; Lian, K. Cure kinetics of aqueous phenol-formaldehyde resins used for oriented strandboard manufacturing: analytical technique. Journal of Applied Polymer Science 2006, 100, 1642-1650.

[42] Chow, S. Z. Kinetic study of the polymerization of phenol-formaldehyde resin in the presence of cellulosic materials. Wood Science 1969, 1, 215-221.

[43] Pizzi, A.; Meikleham, N.; Stephanou, A. Induced accelerated autocondensation of polyflavonoid tannins for phenolic polycondensates. 2. Cellulose effect and application. Journal of Applied Polymer Science 1995, 55, 929-933.

[44] Pizzi, A. Catalytic activation of wood adhesive polycondensation by the adhesion forces to a cellulosic substrate. International Congress on Adhesion Science and Technology, Invited Papers, Festschrift in Honor of Dr. K. L. Mittal on the Occasion of his 50th Birthday, 1st, Amsterdam, Oct. 16-20, 1995 1998, 531-542.

[45] Scheikl, M.; Dunky, M. Measurement of dynamic and static contact angles on wood for the determination of its surface tension and the penetration of liquids into the wood surface. Holzforschung 1998, 52, 89-94.

[46] de Meijer, M.; Thurich, K.; Militz, H. Quantitative measurements of capillary coating penetration in relation to wood and coating properties. Holz Als Roh-Und Werkstoff 2001, 59, 35-45.

[47] Kamke, F. A.; Lee, J. N. Adhesive penetration in wood - A review. Wood and Fiber Science 2007, 39, 205-220.

[48] Dinand, E.; Vignon, M.; Chanzy, H.; Heux, L. Mercerization of primary wall cellulose and its implication for the conversion of cellulose I -> cellulose II. Cellulose 2002, 9, 7-18.

[49] Roman, M.; Winter, W. T. Effect of Sulfate Groups from Sulfuric Acid Hydrolysis on the Thermal Degradation Behavior of Bacterial Cellulose. Biomacromolecules 2004, 5, 1671-1677.

[50] Marchessault, R. H.; Morehead, F. F.; Walter, N. M. Liquid crystal systems from fibrillar polysaccharides. Nature 1959, 184, 632-633.

[51] Revol, J. F.; Bradford, H.; Giasson, J.; Marchessault, R. H.; Gray, D. G. Helicoidal self-ordering of cellulose microfibrils in aqueous suspension. International Journal of Biological Macromolecules 1992, 14, 170-172.

[52] Revol, J. F.; Godbout, L.; Dong, X. M.; Gray, D. G.; Chanzy, H.; Maret, G. Chiral nematic suspensions of cellulose crystallites; phase separation and magnetic field orientation. Liquid Crystals 1994, 16, 127-134.

[53] Dong, X. M.; Kimura, T.; Revol, J.-F.; Gray, D. G. Effects of Ionic Strength on the Isotropic-Chiral Nematic Phase Transition of Suspensions of Cellulose Crystallites. Langmuir 1996, 12, 2076-2082.

[54] Dong, X. M.; Gray, D. G. Induced Circular Dichroism of Isotropic and Magnetically-Oriented Chiral Nematic Suspensions of Cellulose Crystallites. Langmuir 1997, 13, 3029-3034.

[55] Dong, X. M.; Gray, D. G. Effect of counterions on ordered phase formation in suspensions of charged rodlike cellulose crystallites. Langmuir 1997, 13, 2404-2409.

[56] Heux, L.; Chauve, G.; Bonini, C. Nonflocculating and chiral-nematic self-ordering of cellulose microcrystals suspensions in nonpolar solvents. Langmuir 2000, 16, 8210-8212.

[57] Araki, J.; Wada, M.; Kuga, S.; Okano, T. Birefringent glassy phase of a cellulose microcrystal suspension. Langmuir 2000, 16, 2413-2415.

[58] Araki, J.; Kuga, S. Effect of Trace Electrolyte on Liquid Crystal Type of Cellulose Microcrystals. Langmuir 2001, 17, 4493-4496.

[59] Chen, W.; Gray, D. G. Interfacial tension between isotropic and anisotropic phases of a suspension of rodlike particles. Langmuir 2002, 18, 633-637.

[60] Beck-Candanedo, S.; Viet, D.; Gray, D. G. Induced phase separation in cellulose nanocrystal suspensions containing ionic dye species. Cellulose 2006, 13, 629-635.

[61] Beck-Candanedo, S.; Viet, D.; Gray, D. G. Induced Phase Separation in Low-Ionic-Strength Cellulose Nanocrystal Suspensions Containing High-Molecular-Weight Blue Dextrans. Langmuir 2006, 22, 8690-8695.

[62] Beck-Candanedo, S.; Viet, D.; Gray, D. G. Triphase Equilibria in Cellulose Nanocrystal Suspensions Containing Neutral and Charged Macromolecules. Macromolecules 2007, 40, 3429-3436.

[63] Beck-Candanedo, S.; Viet, D.; Gray, D. G. Partitioning of charged and neutral dextran-dye derivatives in biphasic cellulose nanocrystal suspensions. Canadian Journal of Chemistry 2008, 86, 503-511.

[64] Hirai, A.; Inui, O.; Horii, F.; Tsuji, M. Phase Separation Behavior in Aqueous Suspensions of Bacterial Cellulose Nanocrystals Prepared by Sulfuric Acid Treatment. Langmuir 2009, 25, 497-502.

[65] Fleming, K.; Gray, D. G.; Matthews, S. Cellulose crystallites. Chemistry--A European Journal 2001, 7, 1831-1835.

[66] Roman, M.; Gray, D. G. Parabolic Focal Conics in Self-Assembled Solid Films of Cellulose Nanocrystals. Langmuir 2005, 21, 5555-5561.

[67] Onsager, L. The effects of shapes on the interaction of colloidal particles. Annals of the New York Academy of Sciences 1949, 51, 627-659.

[68] Orts, W. J.; Godbout, L.; Marchessault, R. H.; Revol, J. F. Shear-Induced Alignment of Liquid-Crystalline Suspensions of Cellulose Microfibrils. In: Flow-Induced Structure in Polymers; Nakatani, A. I., Dadmun, M. D., Eds.; ACS Symposium Series 597; American Chemical Society: Washington, DC, 1994; pp 335-348.

[69] Orts, W. J.; Godbout, L.; Marchessault, R. H.; Revol, J. F. Enhanced ordering of liquid crystalline suspensions of cellulose microfibrils: A small-angle neutron scattering study. Macromolecules 1998, 31, 5717-5725.

[70] De Souza Lima, M. M.; Borsali, R. Rodlike cellulose microcrystals: Structure, properties, and applications. Macromolecular Rapid Communications 2004, 25, 771-787.

[71] Onogi, S.; Asada, T. Rheology and Rheo-Optics of Polymer Liquid Crystals. In: Rheology, Volume 1: Principles; Astarita, G., Marrucci, G., Nicolais, L., Eds.; International Congress on Rheology. (Proceedings; 8th); Plenum Press: New York, 1980.

[72] Wissbrun, K. F. Rheology of Rod-Like Polymers in the Liquid-Crystalline State. Journal of Rheology 1981, 25, 619-662.

[73] Jamieson, A. M.; Gu, D. F.; Chen, F. L.; Smith, S. Viscoelastic behavior of nematic monodomains containing liquid crystal polymers. Progress in Polymer Science 1996, 21, 981-1033.

[74] Rey, A. D.; Denn, M. M. Dynamical phenomena in liquid-crystalline materials. Annual Review of Fluid Mechanics 2002, 34, 233-266.

[75] Ebeling, T.; Paillet, M.; Borsali, R.; Diat, O.; Dufresne, A.; Cavaille, J. Y.; Chanzy, H. Shear-induced orientation phenomena in suspensions of cellulose microcrystals, revealed by small angle X-ray scattering. Langmuir 1999, 15, 6123-6126.

[76] Moldenaers, P.; Fuller, G.; Mewis, J. Mechanical and Optical Rheometry of Polymer Liquid-Crystal Domain-Structure. Macromolecules 1989, 22, 960-965.

[77] Ernst, B.; Navard, P.; Hashimoto, T.; Takebe, T. Shear-Flow of Liquid-Crystalline Polymer-Solutions as Investigated by Small-Angle Light-Scattering Techniques. Macromolecules 1990, 23, 1370-1374.

[78] Walker, L.; Wagner, N. Rheology of Region-I Flow in a Lyotropic Liquid-Crystal Polymer - The Effects of Defect Texture. Journal of Rheology 1994, 38, 1525-1547.

[79] Walker, L. M.; Wagner, N. J.; Larson, R. G.; Mirau, P. A.; Moldenaers, P. The Rheology of Highly Concentrated PBLG Solutions. Journal of Rheology 1995, 39, 925-952.

[80] Langelaan, H. C.; Gotsis, A. D. The relaxation of shear and normal stresses of nematic liquid crystalline polymers in squeezing and shear flows. Journal of Rheology 1996, 40, 107-129.

[81] Sisko, A. W. The Flow of Lubricating Greases. Industrial & Engineering Chemistry 1958, 50, 1789-1792.

[82] Bingham, E. C. An Investigation of the Laws of Plastic Flow. U.S. Bureau of Standards Bulletin 1916, 13, 309-353.

[83] Ostwald, W. Über die Geschwindigkeitsfunktion der Viskositat disperser Systeme I. Kolloid Zeitschrift 1925, 36, 99-117.

[84] de Waele, A. Viscometry and Plastometry. Journal of the Oil & Colour Chemists Association 1923, 6, 33-88.

[85] Ferguson, J.; Kembłowski, Z. Applied Fluid Rheology. Elsevier: New York, 1991; pp. 147 & 205.

CHAPTER 4

EFFECTS OF CELLULOSE NANOCRYSTALS ON PHENOL–FORMALDEHYDE ADHESIVE RESINS—PART II: CURE KINETICS

4.1. ABSTRACT

The purpose of this study was to determine the effects of cellulose nanocrystals (CNCs) on the cure kinetics of phenol–formaldehyde (PF) resol resin. The curing progressions of four CNC–resin mixtures, containing 0–3 wt % CNCs, based on solids content, were analyzed by non-isothermal differential scanning calorimetry (DSC) using different heating rates between 2 and 10 °C/min. The DSC curves showed two exotherms followed by an endotherm. The energy of activation for the first exotherm, attributed to the condensation of methylolureas, stemming from post-added urea in the commercial resin, was reduced by the CNCs. The greatest reduction was observed at a CNC content of 1 wt %. The energy of activation for the second exotherm, attributed to methylolphenol and methylolurea condensation and methylolation, and possibly the formation of hemiformals, was not affected by the CNCs. Increasing CNC contents caused higher degrees of reaction conversion during the first curing stage and a greater loss of sample mass, attributed to formaldehyde release during resin cure. The total heat of cure was not affected by the CNCs. CNCs were concluded to accelerate the first stage of resin cure (methylolurea condensation) but not the second.

4.2. INTRODUCTION

Phenol–formaldehyde (PF) adhesive resins, extensively used in the wood composites industry, are thermosetting polymers formed by the reaction of phenol with formaldehyde. The curing chemistry of PF resins is known to be affected by wood–resin interactions [1-11]. Several studies on the effect of wood on PF resin cure have found that wood lowers the activation energy of the curing reactions [1-5]. A few studies, on the other hand, have found activation energies to be higher in the presence of wood [5, 6]. The mechanisms by which wood affects the curing reactions are incompletely understood. It has been proposed that the carbohydrate constituents of wood are responsible for its catalytic activity [2]. Cellulose, the main carbohydrate of wood, has been found to lower the activation energy of PF resin curing reactions [1, 2, 12]. The activation energy in the presence of carbohydrates has been suggested to depend on the number of accessible hydroxyl groups [1]. The catalytic activity of cellulose has been attributed to the activation of the methylol groups and phenolic ortho and para positions through secondary interactions of cellulose with the methylol and phenol hydroxyl groups, respectively [2].

Cellulose nanocrystals (CNCs) are highly crystalline, nanoscale, rodlike particles of cellulose, obtained by acidic degradation of purified cellulose starting materials. CNCs derived from wood pulp have average lengths of 100–150 nm and average diameters of 4.5–5 nm [13]. Because of their small size and large specific surface area, CNCs have many accessible hydroxyl groups and are therefore likely to have a significant effect on the curing reactions and properties of PF resins.

The purpose of this study, which is part of a larger investigation of the effects of CNCs on the properties and performance of PF adhesive resin, was to determine the effects of CNCs on PF resin cure kinetics. Small amounts of CNCs (1–3%, based on solids content) were added to a commercial PF resol resin (OSB core resin from Dynea) and the curing of the resin mixtures was analyzed by non-isothermal differential scanning calorimetry (DSC). The results of this study may enhance our understanding of the effects of wood on PF resin cure.

4.3. EXPERIMENTAL

4.3.1. Materials

Dissolving-grade softwood sulfite pulp (Temalfa 93A-A) was kindly provided by Tembec, Inc. Liquid PF resol resin (OSB core resin, 50 wt % solids content, < 0.1 wt % free formaldehyde) was kindly provided by Dynea North America, now Arclin. The resin was stored frozen in 500 mL units until use. Prior to use, the resin was thawed and thoroughly mixed. Sulfuric acid (95.9 wt %, certified) was purchased from Fisher Scientific and used as received. Deionized water (18.2 MΩ·cm) was generated from tap water with a Millipore Direct-Q 5 Ultrapure Water System.

4.3.2. Methods

4.3.2.1. Preparation of resin mixtures

Four CNC–resin mixtures with CNC contents of 0 wt % (PF0), 1 wt % (PF1), 2 wt % (PF2), and 3 wt % (PF3), based on total solids content, were prepared as described in the previous chapter. Briefly, a stable CNC suspension was prepared by hydrolysis of milled wood pulp with 64 wt % sulfuric acid for 60 min at 45.5 °C and an acid-to-pulp ratio of 10 mL/g. The suspension was concentrated to 10 wt % with a rotary evaporator (Büchi Rotavapor R-200) using a water bath temperature of 40 °C. Different amounts of the CNC suspension and deionized water were slowly added under stirring (500 rpm) to the PF resin. Stirring was continued for 10 min to ensure good mixing. The respective amounts of CNC suspension and deionized water were chosen to maintain an equal solids content of 44.64 wt % in the four resin mixtures. The pH of the resin mixtures decreased slightly with increasing CNC content from 12.30 ± 0.01 at 0 wt % to 12.27 ± 0.02 at 3 wt %. No fillers, extenders, or any other additives were added in this study.

4.3.2.2. DSC measurements

DSC measurements were performed with a TA Instruments Q100 differential scanning calorimeter that had been calibrated with indium and sapphire standards. Nitrogen, at a flow rate of 50 mL/min, was used as the purge gas. Approximately 10–12 mg of a resin sample was sealed in a stainless steel high-volume DSC pan (TA Instrument), which can suppress volatilization during resin cure up to an internal pressure of 3.8 MPa. The weight of the loaded, sealed sample pan was measured before and after the experiment. Dynamic temperature scans were performed according to ASTM E 698 – 05 over the temperature range 25–200 °C at heating rates of 2, 4, 6, 8, and 10 °C/min. Experiments were run in triplicate. Peak temperatures and areas were determined with TA Instruments' Universal Analysis 2000 software. The degree of reaction conversion at time t, $\alpha(t)$, was calculated as the partial heat of reaction at time t, $\Delta H_p(t)$, divided by the total heat of reaction, ΔH_0, and expressed in percent:

$$\alpha(t) = \frac{\Delta H_p(t)}{\Delta H_0} \cdot 100\% \qquad [1]$$

Values for the activation energy, E_a, and frequency factor, Z, were determined using the Kissinger method [14], which is based on the expression

$$\frac{E_a \beta}{RT_p^2} = Zn(1-a_p)^{n-1} \exp\left(-\frac{E_a}{RT_p}\right) \qquad [2]$$

where β is the heating rate (K/s), R is the universal gas constant (8.314 J/mol·K), T_p is the peak temperature (K), n is the reaction order, and a is the fraction reacted. Kissinger argued that the product $n(1–a_p)^{n–1}$ was very nearly equal to unity and independent of β. With $n(1–a_p)^{n–1} = 1$, rearranging eq 2 gives

$$\frac{\beta}{T_p^2} = \frac{ZR}{E_a} \exp\left(-\frac{E_a}{RT_p}\right) \qquad [3]$$

Taking the logarithm and multiplying by –1 gives a linear relationship between $-\ln(\beta/T_p^2)$ and $1/T_p$ according to

$$-\ln\left(\frac{\beta}{T_p^{\,2}}\right) = \frac{E_a}{RT_p} - \ln\left(\frac{ZR}{E_a}\right) \qquad [4]$$

E_a and Z were calculated from the slope and y-axis intercept, respectively, of a least-square regression line in a plot of $-\ln(\beta/T_p^{\,2})$ versus $1000/T_p$.

The reaction rate constant, k, was calculated from the values for E_a and Z using the Arrhenius equation,

$$k(T) = Z\exp\left(-\frac{E_a}{RT}\right) \qquad [5]$$

where $k(T)$ is the specific rate constant (1/s) at temperature T.

4.4. RESULTS AND DISCUSSION

The DSC curves of the resin mixtures all showed two well defined exotherms, a broad one at lower temperatures (first exotherm) and a narrow one at higher temperatures (second exotherm), followed by a less well defined endotherm. A typical DSC curve is shown in Figure 4.1. The figure also illustrates our method of baseline interpolation. When the two exotherms were well separated, a straight and, if necessary, slanted line was used as the baseline for the first exotherm and a horizontal line was used as the baseline for the second exotherm. When the two exotherms overlapped, a single horizontal line was used and the peak area for each exotherm was determined using the vertical drop method.

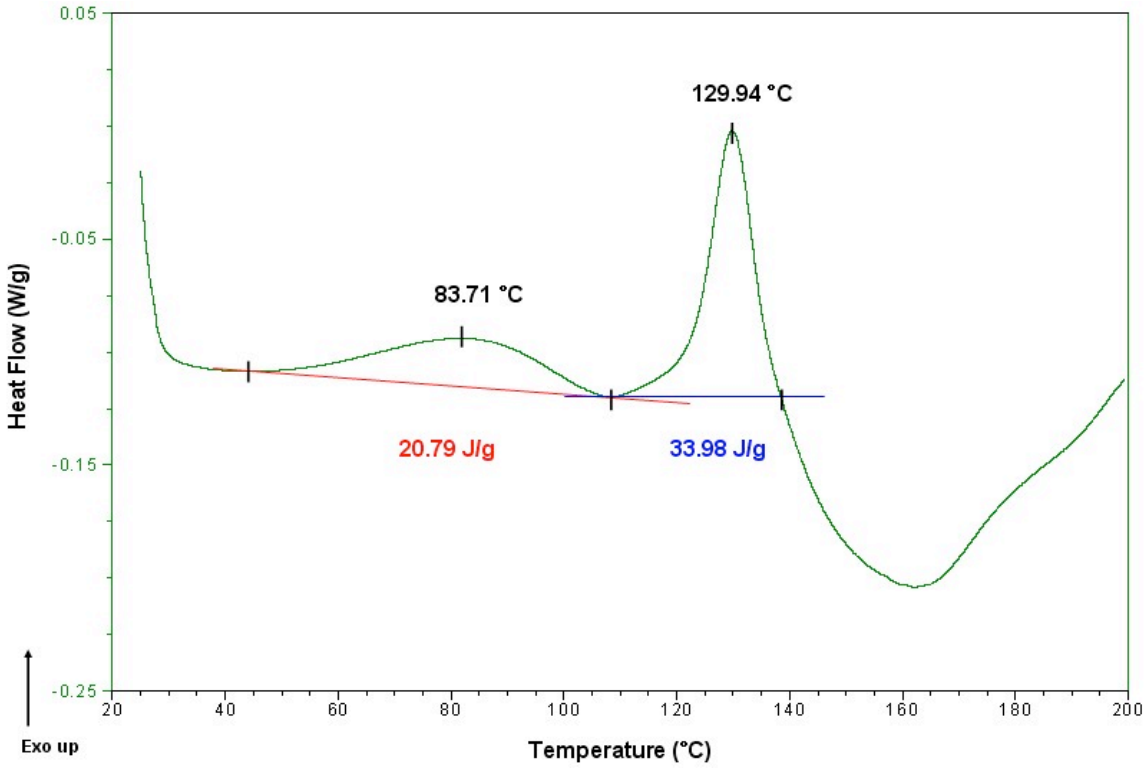

Figure 4.1. DSC curve for PF0 at a heating rate of 2 °C/min.

The synthesis and cure of PF resol resins involve two main steps: (i) the addition of formaldehyde to phenol, yielding methylolphenols, and (ii) the condensation of methylolphenols, resulting in methylene bridges (R–CH_2–R). Table 4.1 lists DSC peak temperatures from the literature for different reactions involved in PF resin synthesis and cure.

Table 4.1. DSC peak temperatures for different reactions involved in PF resin synthesis and cure

Reaction	DSC Peak Temperature(s) (°C)	Heating rate (°C/min)	Reference
Formation of *o*-methylolphenol from phenol and paraformaldehyde[a]	85–95	4	[15]
Reaction of phenol and formaldehyde[b]	85, 150	10	[16]
Condensation of methylol groups and formation of methylene bridges in the reaction of phenol and paraformaldehyde[a]	150–165	4	[15]
Self-condensation of *p*-methylolphenol	144	10	[16]
Self-condensation of *o*-methylolphenol	165	10	[16]
Self-condensation of *o*,*p*-dimethylolphenol[c]	134–163	10	[17]
Self-condensation of *o*,*o*-dimethylolphenol[c]	134–177	10	[17]
-	114, 151	10	this study

[a] F/P ratio = 1, NaOH content in the phenol–paraformaldehyde mixtures = 0–1 %

[b] alkaline, aqueous solution, F/P ratio = 1.8, NaOH/P ratio = 0.6

[c] freeze-dried mixture, NaOH/dimethylolphenol ratio = 0.15–1

For the pure resin (PF0), we obtained peak temperatures of 114 and 151 °C at a heating rate of 10 °C/min for the first and second exotherm, respectively. Comparison of our values with those from the literature (Table 4.1) revealed that our peak temperature for the first exotherm was well above the literature values for the addition reactions. Considering also the low free formaldehyde content of the resin (<0.1 wt %, manufacturer specification), the first exotherm in our DSC curves was likely not related to the formation of methylolphenols. It was, however, also not likely to be related to methylolphenol condensation reactions because those reactions, according to the literature (Table 4.1), require much higher temperatures. The second exotherm in our

DSC curves, on the other hand, could well be due to methylolphenol condensation reactions because the measured peak temperature lay within the range of the literature values for these reactions.

Endotherms are generally not observed in DSC curves of PF resins [6, 18-21]. They have, however, been reported for phenol–urea–formaldehyde resins [22, 23] and commercial PF core resins [3, 24]. Urea is often added to commercial PF resins in small quantities to control formaldehyde emission, enhance flow properties, accelerate hardening, and reduce costs [25, 26]. Depending on the time of addition, either during resin manufacture or upon its completion, urea-extended PF resins contain either unreacted urea and formaldehyde (post-addition) or methylolurea, formed by the reaction of urea and formaldehyde, and little to no unreacted formaldehyde. Co-condensation of urea or methylolurea with methylolphenol is largely suppressed under the reaction conditions of resol resin manufacture [26, 27]. The presence of the endotherm in our DSC curves indicated that the PF resin contained urea.

The curing chemistry of urea-extended PF resins is more complicated than that of traditional PF resins. Upon heating, unreacted formaldehyde in the resin may react with primary or secondary amide groups of urea, monomethylolurea, or dimethylolurea molecules, or with available ortho or para positions in the oligomeric methylolphenols. At higher temperatures, methylolureas undergo condensation reactions with other methylolureas (self-condensation), which, at the pH levels of PF resol resins, are favored over co-condensation reactions with methylolphenols [22]. The self-condensation of methylolureas can proceed by one of two ways. Condensation of methylol groups with primary or secondary amides results in the formation of methylene bridges, whereas the condensation of two methylol groups leads to methylene ether bridges ($R–CH_2–O–CH_2–R$). Contrary to the condensation of methylolphenols, which favors the formation of methylene bridges under alkaline conditions, the condensation of methylolureas favors the formation of methylene ether bridges at pH levels above 9 [28]. Methylene ether bridges are thermally unstable and decompose endothermally at elevated temperatures into methylene bridges under elimination of formaldehyde [29, 30]. The decomposition of methylene ether bridges combined with the elimination of

formaldehyde is known to cause endothermic peaks in the DSC curves of urea–formaldehyde resins [30].

Under the assumption that the commercial PF resin contained urea, based on the endotherm in the DSC curves, and considering that the methylolphenol condensation reactions require temperatures well above 130 °C (Table 4.1), the first endotherm in our DSC curves was most likely due to the condensation of methylolureas and formation of methylene ether bridges. Addition of formaldehyde to urea was ruled out as the cause for the first endotherm based on the low free formaldehyde content of the resin and the fact that urea methylolation reactions occur at much lower temperatures [31]. The second exotherm in our DSC curves could involve three closely related reactions: the condensation of methylolphenols and formation of methylene bridges under release of water and formaldehyde, the reaction of the liberated formaldehyde with unreacted or partially methylolated urea and possibly phenol, and the condensation of methylolureas and formation of methylene ether bridges. The endotherm at higher temperatures was likely due to the decomposition of methylene ether bridges between methylolureas under release of formaldehyde.

As to the potential participation of the cellulose hydroxyl groups in the curing reactions, one has to consider the ambient pH. Ample evidence exists that cellulose reacts with formaldehyde and formaldehyde adducts, such as methylolureas, under acidic conditions [32]. In fact, acid-catalyzed etherification and crosslinking reactions of cellulose with formaldehyde and formaldehyde-based N-methylol compounds have been widely studied in the textile industry for the manufacture of wrinkle-resistant or durable press cotton fabrics [33]. The literature on base-catalyzed reactions of cellulose with formaldehyde and methylol phenols has been reviewed by Myers [34]. Under basic conditions, as present in PF resol resins, cellulose hydroxyl groups may reversibly react with formaldehyde molecules to yield hemiformals (R–O–CH_2–OH). The formation of formal crosslinks (R–O–CH_2–O–R) is not favored under basic conditions. Furthermore, the condensation of methylolphenols with cellulose hydroxyl groups under basic conditions has been deemed unlikely [34]. Concerning the condensation of methylolureas with cellulose hydroxyl groups under basic conditions, Welch and Margavio have

demonstrated that only N-methylol compounds able to form α,β-unsaturated imines with CH_2=N–C=O groups react with cellulose hydroxyl groups at pH values above 7 [35]. These findings suggest that the cellulose hydroxyl groups likely did not undergo chemical reactions with the methylolurea and methylolphenol compounds during resin cure but might have reacted to some extent with the formaldehyde released in the reactions that were believed to be responsible for the second exotherm.

Figure 4.2 shows the DSC curves for the four resin mixtures at a heating rate of 6 °C/min. The peak temperature for the second exotherm was unaffected by the CNCs. In contrast, the peak temperature for the first exotherm was lower in the presence of CNCs.

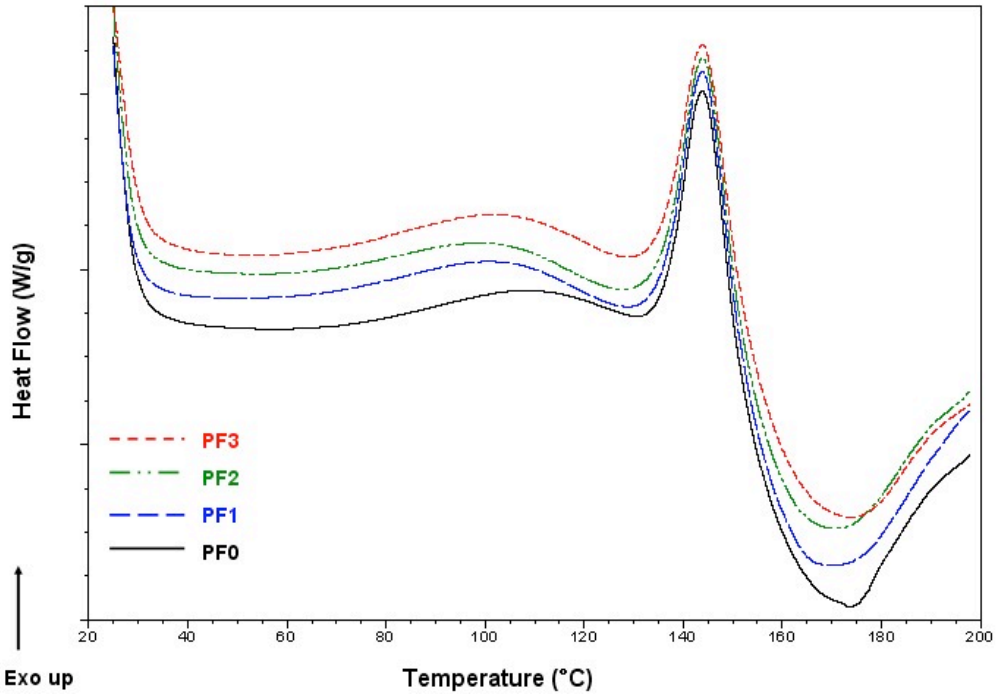

Figure 4.2. DSC dynamic scans of the four resin mixtures at a heating rate of 6 °C/min.

To analyze the effect of the CNCs on the cure kinetics of the resin, we recorded DSC curves for the resin mixtures at different heating rates. Figure 4.3 shows the DSC curves for PF0 at heating rates of 2, 4, 6, 8, and 10 °C/min.

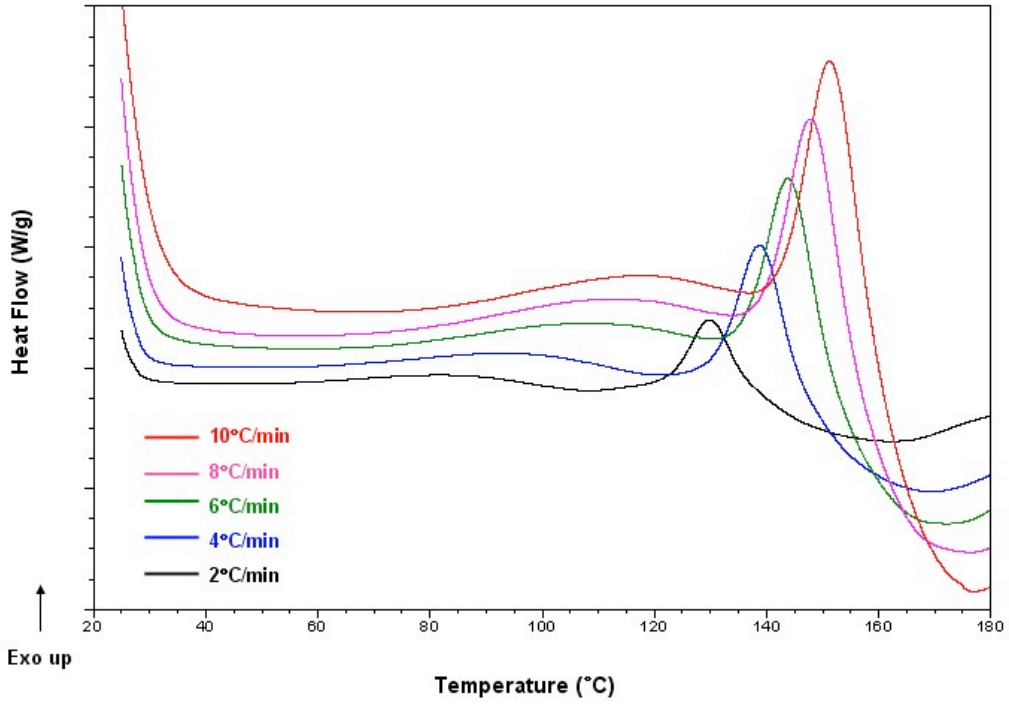

Figure 4.3. DSC scans of PF0 at different heating rates.

As expected, the peak temperatures of both exotherms increased with increasing heating rate. The shift to higher temperatures was more pronounced for the first exotherm than for the second. The peak temperatures for first and second exotherm at different heating rates, measured in triplicate, are listed in Table 4.2.

The activation energy, E_a, and frequency factor, Z, for the first and second exotherm were determined from Kissinger plots, i.e. plots of $-\ln(\beta/T_p^2)$ vs. $1000/T_p$, where β is the heating rate in K/s and T_p is the peak temperature in K. The plots for the first and second exotherms of the resin mixtures are shown in Figures 4.4 and 4.5, respectively. A linear regression model was fit to the 15 data points (three observations each at five heating rates), obtained for each resin mixture, using the least squares methods. The obtained linear regression lines are also shown in Figures 4.4 and 4.5. E_a and Z, determined from the slope and intercept of the linear regression line, respectively, are listed in Table 4.2.

Table 4.2. Peak temperature, activation energy (E_a), and frequency factor (Z) values for the first and second exotherm

Resin mixture	Peak temperature (°C)					E_a[a] (kJ/mol)	Z[a] (1/s)	$\bar{E}_a$[b] (kJ/mol)	SD
	2 °C/min	4 °C/min	6 °C/min	8 °C/min	10 °C/min				
First exotherm									
PF0	85.36	95.17	107.00	114.15	115.35	50.15	$3.5 \cdot 10^4$	50.68	3.53
	81.66	94.31	108.17	110.39	114.73				
	83.71	98.14	106.35	110.19	112.64				
PF1	77.99	92.96	101.86	108.47	113.60	46.57	$1.2 \cdot 10^4$	46.65	1.30
	79.14	93.26	101.38	108.85	114.23				
	79.20	93.37	102.00	106.83	112.23				
PF2	80.76	92.48	100.93	104.83	112.64	47.65	$1.8 \cdot 10^4$	47.92	2.08
	79.05	93.70	97.55	107.62	113.95				
	78.49	93.48	100.27	109.47	114.17				
PF3	80.86	92.59	102.44	107.34	113.09	51.17	$5.9 \cdot 10^4$	51.63	3.29
	79.14	92.44	101.42	108.07	112.14				
	82.90	92.92	103.08	108.74	109.68				
Second exotherm									
PF0	129.77	138.32	143.84	147.81	151.23	101.18	$3.3 \cdot 10^{10}$	101.18	0.74
	130.06	138.73	143.64	147.74	151.13				
	129.94	138.38	143.81	147.70	151.28				
PF1	129.93	138.68	143.69	148.05	150.96	100.73	$2.9 \cdot 10^{10}$	100.74	0.79
	129.88	138.29	143.77	147.67	151.35				
	128.81	138.23	143.65	147.87	151.22				
PF2	129.67	138.32	143.77	147.92	151.38	100.80	$2.9 \cdot 10^{10}$	99.73	1.47
	129.90	138.26	143.94	147.87	150.86				
	130.02	137.94	143.83	147.44	150.99				
PF3	129.63	138.13	143.50	147.63	151.04	100.15	$2.4 \cdot 10^{10}$	100.19	1.14
	129.79	138.30	143.82	147.26	151.00				
	129.32	138.41	143.30	147.58	151.29				

[a] obtained by least-square linear regression of all 15 data points.

[b] mean and standard deviation of 27 E_a values, obtained by statistical analysis with an orthogonal array.

As can be seen in Figures 4.4 and 4.5, the slopes and intercepts for the four resin mixtures differed in the case of the first exotherm but were nearly the same in the case of the second. Accordingly, E_a and Z for the second exotherm stayed nearly constant (Table 4.2), showing merely a slightly decrease with increasing CNC content. For the first exotherm, E_a and Z decreased from PF0 to PF1 and then increased with increasing CNC content to values above those observed at 0 wt %.

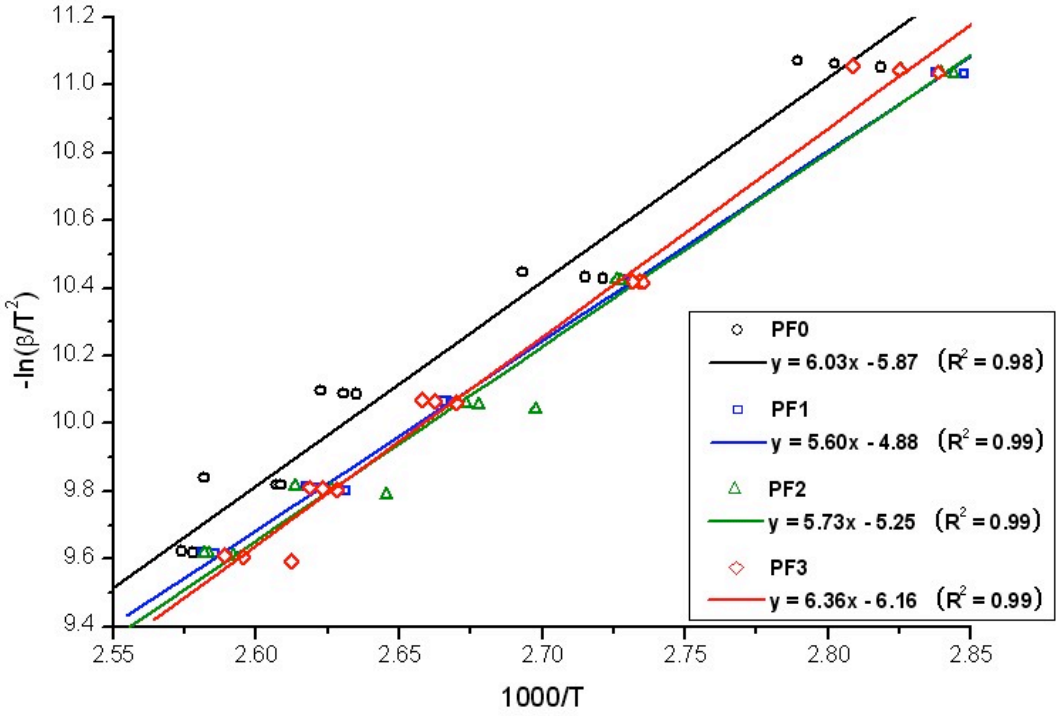

Figure 4.4. Kissinger plot with linear regression lines for the first exotherm.

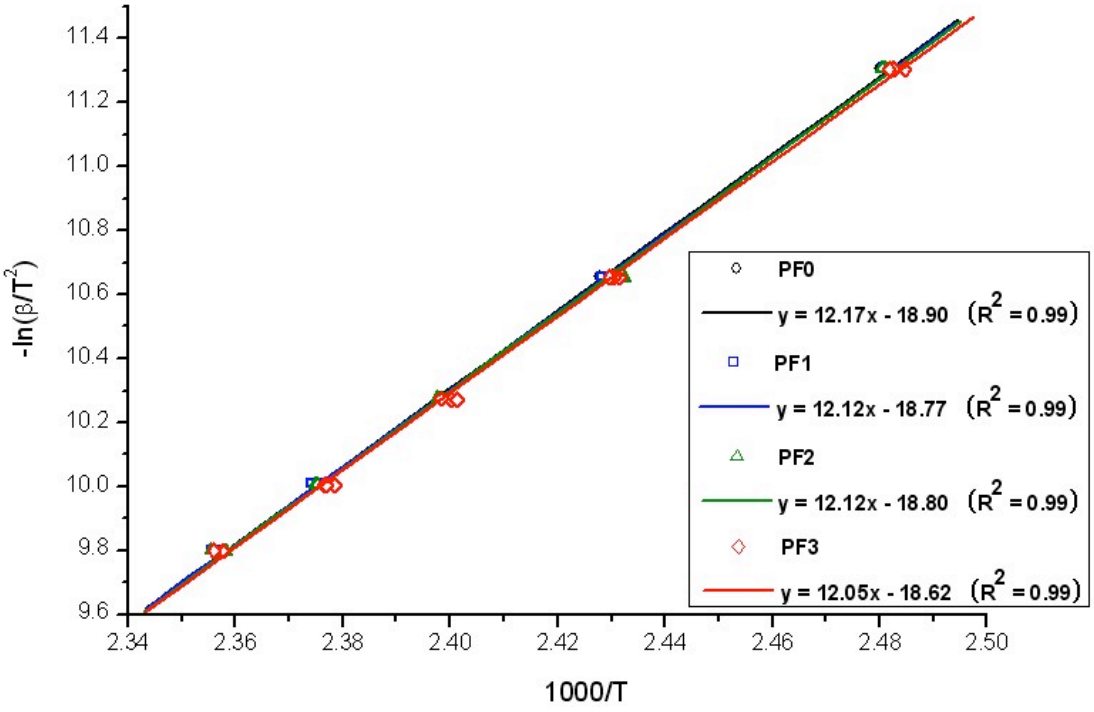

Figure 4.5. Kissinger plot with linear regression lines for the second exotherm.

To quantify the error in our E_a values, we analyzed the data using an experimental design approach. The problem can be treated as a 3^5 full factorial design, with five factors of three levels each and a total of 243 possible combinations. Instead of analyzing all 243 combinations for each resin mixture, we generated an orthogonal array with 27 combinations using the SPSS software. For each combination, E_a was determined from the slope of the Kissinger plot. Finally, the mean activation energy, $\bar{E}_a$, and standard deviation, SD, were calculated from the 27 obtained E_a values. $\bar{E}_a$ and SD for the four resin mixtures and two exotherms are listed in Table 4.2 and plotted in Figure 4.6.

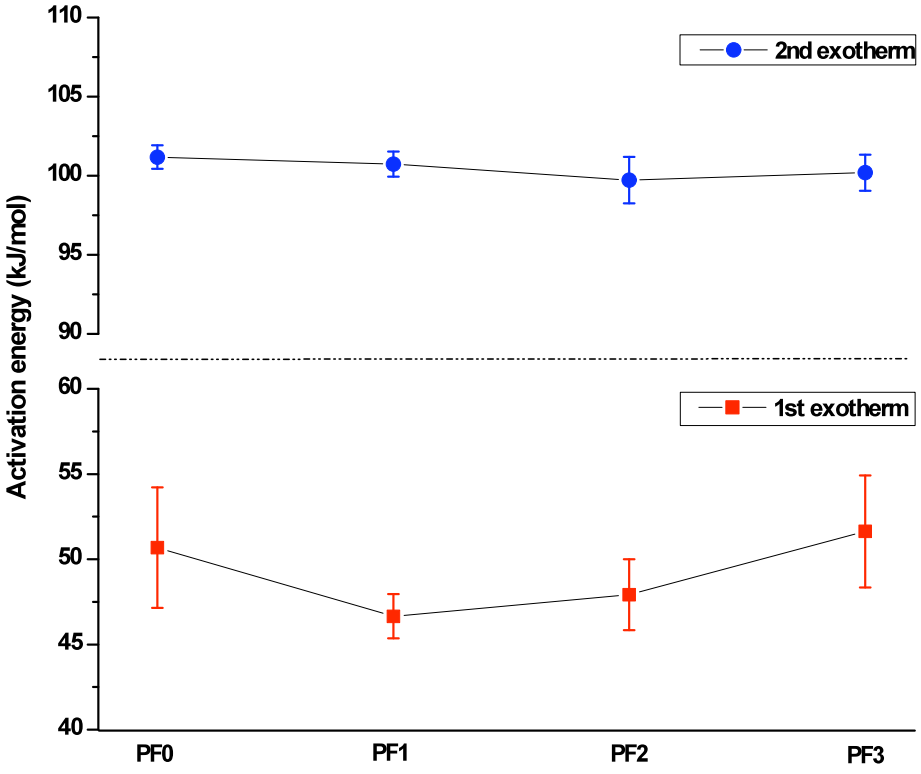

Figure 4.6. Mean activation energies ($\bar{E}_a$) for the two exotherms obtained using an orthogonal design. Error bars represent ± one standard deviation.

One-way ANOVA (Tukey's HSD, $\alpha = 0.05$) revealed that the decrease in $\bar{E}_a$ for the first exotherm for PF1 and PF2 with respect to PF0 was statistically significant, but that the difference between the values for PF3 and PF0 was not (see Appendix 4.1). For the second exotherm, $\bar{E}_a$ for PF2 and PF3 was significantly lower, in a statistical sense, than

for PF0 but $\bar{E}_a$ for PF1 and PF0 were statistically equivalent. To summarize these results, the activation energy for the first exotherm was lowered by a small amount of CNCs (1 wt %). In the presence of larger amounts of CNCs (≥ 2 wt %), the effect was less pronounced and vanished at a CNC content of 3 wt %. E_a for the second exotherm was only weakly affected by the CNCs. It was slightly lowered for CNC contents ≥ 2 wt %.

To analyze the effect of the CNCs on the rate constant, k, we calculated values for k for different temperatures using the Arrhenius equation and the determined values for E_a and Z. The values obtained for 80, 100, 120, 140 and 160 °C are listed in Table 4.3 in the appendix. Figure 4.7 shows the relative rate constant, k/k_{PF0}, for PF1, PF2, and PF3 as a function of temperature.

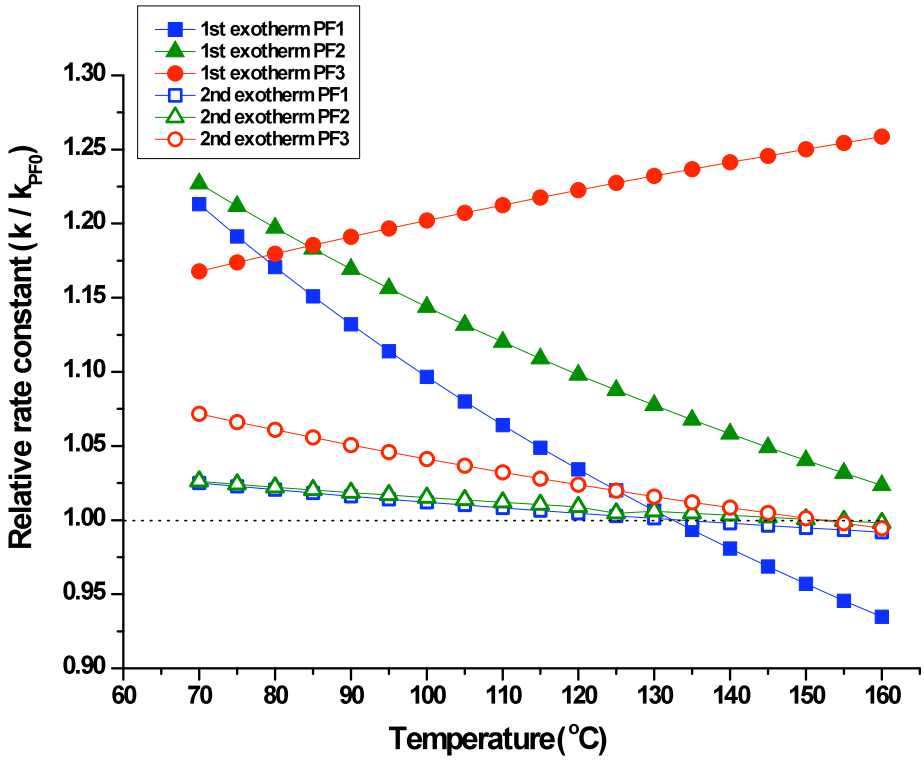

Figure 4.7. Relative rate constant, k/k_{PF0}, for the first and second exotherm as a function of temperature.

The rate constant for the second exotherm was nearly unaffected by the CNCs, as evidenced in the closeness of the relative rate constants to 1. The rate constant for the

first exotherm was elevated by the CNCs. The effect, however, was temperature dependent and diminished for the CNC contents 1 and 2 wt % with increasing temperature. The peak temperatures for the first exotherm were in the range 78–115 °C. Therefore, at most of the observed peak temperatures, a higher CNC content caused a higher reaction rate. At the lowest peak temperatures, observed at a heating rate of 2 °C/min, the rate constant was elevated by a factor of about 1.2 at any CNC content.

To verify the effect of the CNCs on the rate constants, we analyzed the DSC data according to the degree of reaction conversion. Figure 4.8 shows the average degree of reaction conversion for PF0 at different heating rates as a function of temperature.

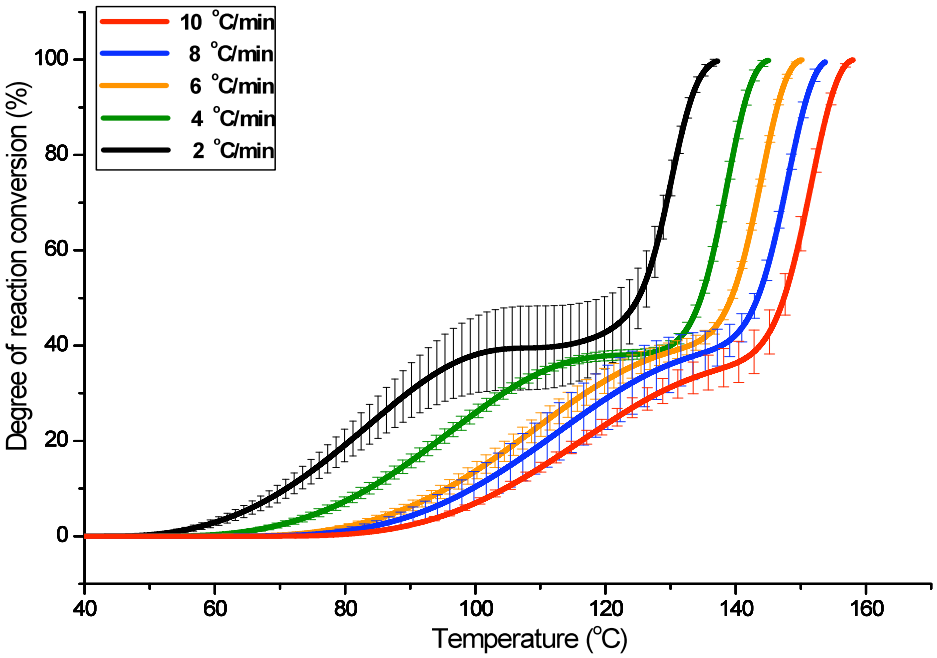

Figure 4.8. Average degree of reaction conversion for PF0 at different heating rates as a function of temperature. Error bars represent ± one standard deviation.

The first increase in degree of reaction conversion corresponds to the first exotherm in the DSC curves and the second increase to the second exotherm. With increasing heating rate, the intermediate plateau became less pronounced as a result of the larger shift to higher temperatures of the first exotherm with respect to the second. Furthermore, with increasing heating rate, the plateau moved to lower degrees of reaction conversion

indicating that at lower heating rates the reaction was more advanced after the first curing stage than at higher ones.

Figure 4.9 shows the average degree of reaction conversion for the four resin mixtures at a heating rate of 8 °C/min as a function of temperature.

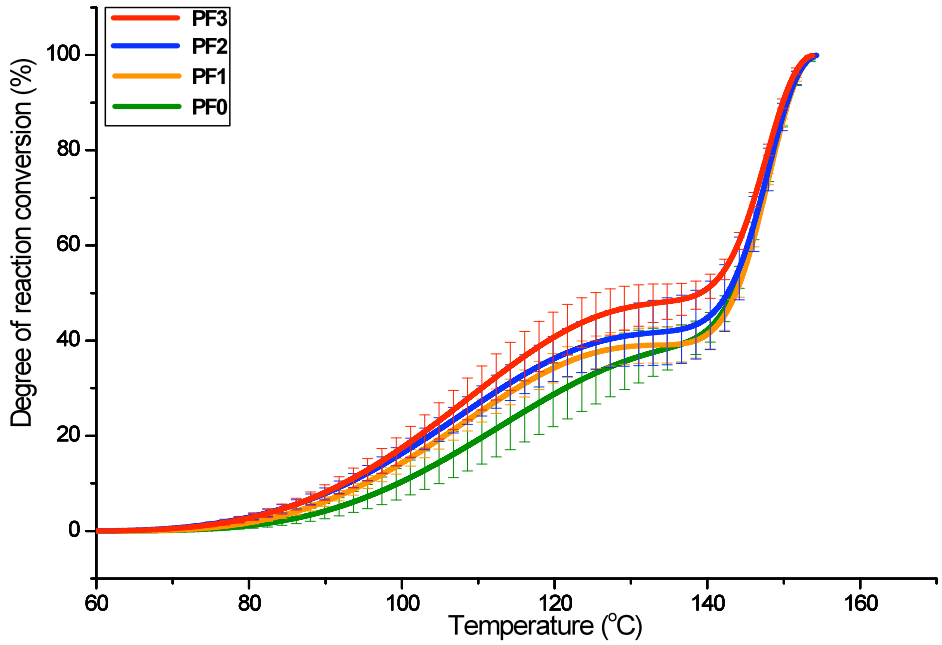

Figure 4.9. Average degree of reaction conversion for the four resin mixtures at a heating rate of 8 °C/min as a function of temperature. Error bars represent ± one standard deviation.

The CNCs noticeably affected the kinetics of the first stage of curing. The first increase in degree of reaction conversion was increasingly steep with increasing CNC content, i.e. during the first stage of curing, higher CNC contents caused a higher degree of reaction conversion at any given temperature. At a heating rate of 8 °C/min, the degree of reaction conversion for PF3 at the plateau was around 10% higher than for PF0. The second curing stage appeared to be less affected by the CNCs. The second increase in the degree of reaction conversion started and finished at approximately the same temperature for all resin mixtures.

The degree of reaction conversion at temperature *T* was derived from the partial peak area at *T*. The combined total peak area of the first and second exotherm is a measure for the total heat of reaction, or cure enthalpy, ΔH. The measured ΔH values for the four resin mixtures at different heating rates are plotted in Figure 4.10.

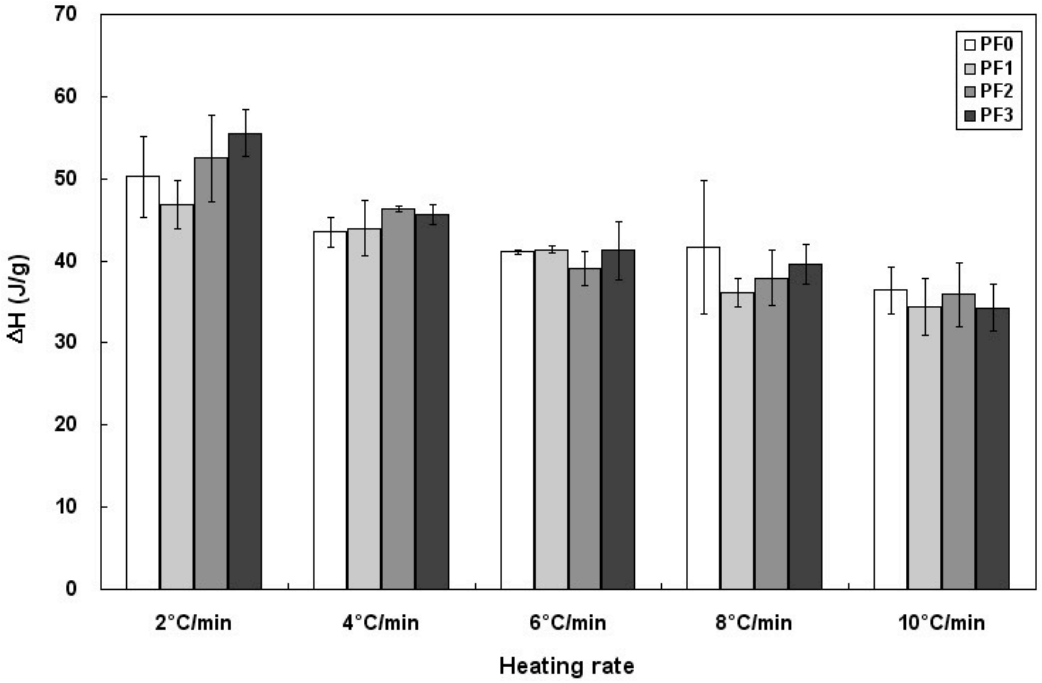

Figure 4.10. Total heat of reaction (ΔH) of dynamic DSC scans at multiple heating rates. Error bars represent ± one standard deviation.

Because the second exotherm might be partly overlapped by the adjacent endotherm, the ΔH values have to be interpreted with caution. The total heat of reaction decreased slightly with increasing heating rate and appeared to be largely unaffected by the CNCs.

Figure 4.11 shows the percentage of the total heat of reaction that was attributable to the first exotherm. The percentage seemed to increase with increasing CNC content, confirming that the degree of reaction conversion after the first curing stage was higher at higher CNC contents. The corresponding decrease in the percentage of the total heat of reaction attributable to the second exotherm may be real or may be due to a stronger overlap by the adjacent endotherm at higher CNC contents. Thus, it is possible that the

total heat of reaction increased with increasing CNC content but that the effect was obscured by an increasing number of endothermically decomposing methylene ether bridges between methylolureas formed in the accelerated first stage.

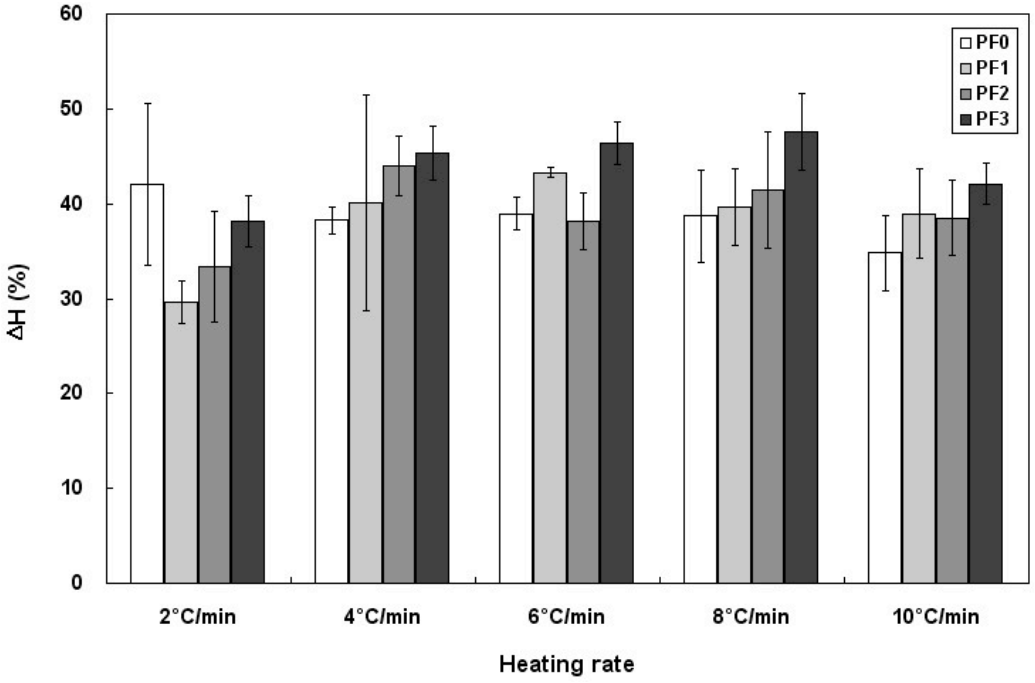

Figure 4.11. Percentage of the total heat of reaction attributable to the first exotherm. Error bars represent ± one standard deviation.

The decomposition of methylene ether bridges to methylene bridges is accompanied by the release of formaldehyde. Weighing the sample pans before and after the DSC experiments revealed a weight loss of up to 10%, depending primarily on heating rate, indicating that the internal pressure during the experiments had exceeded 3.8 MPa, the internal pressure limit for the high-volume sample pans. The observed weight losses at different heating rates are shown in Figure 4.12. As can be seen, a higher heating rate caused a smaller weight loss, suggesting that less formaldehyde was released during the experiment. Furthermore, at higher heating rates (≥ 6 °C/min) the weight loss was noticeably higher in the presence of CNCs than in the absence. The differences in the effect of CNCs on the observed weight loss at higher and lower heating rates could be explained as follows: At lower heating rates (≤ 4 °C/min), the first curing stage, i.e. the

condensation of methylolureas and formation of methylene ether bridges, had enough time to proceed to completion even in the absence of CNCs, as evidenced by the pronounced plateau in the degree of reaction conversion curves for PF0 (Figure 4.8). Thus, the accelerating effect of the CNCs on the first curing stage did not significantly affect the number of methylene ether bridges in the resin. At higher heating rates (≥ 6 °C/min), the first curing stage was not completed by the time the second curing stage started, as evidenced by the rudimentary nature of the plateau in the degree of reaction conversion curves of PF0 (Figure 4.8). However, in the resin mixtures containing CNCs, the first curing stage had, by the time the second curing stage started, progressed to a more advanced level due to the accelerating effect of the CNCs, as evidenced by the higher degrees of conversion at the plateau (Figure 4.9). Thus, the resin mixtures containing CNCs probably had a higher number of methylene ether bridges by the time the second curing stage started, resulting in a higher release of formaldehyde.

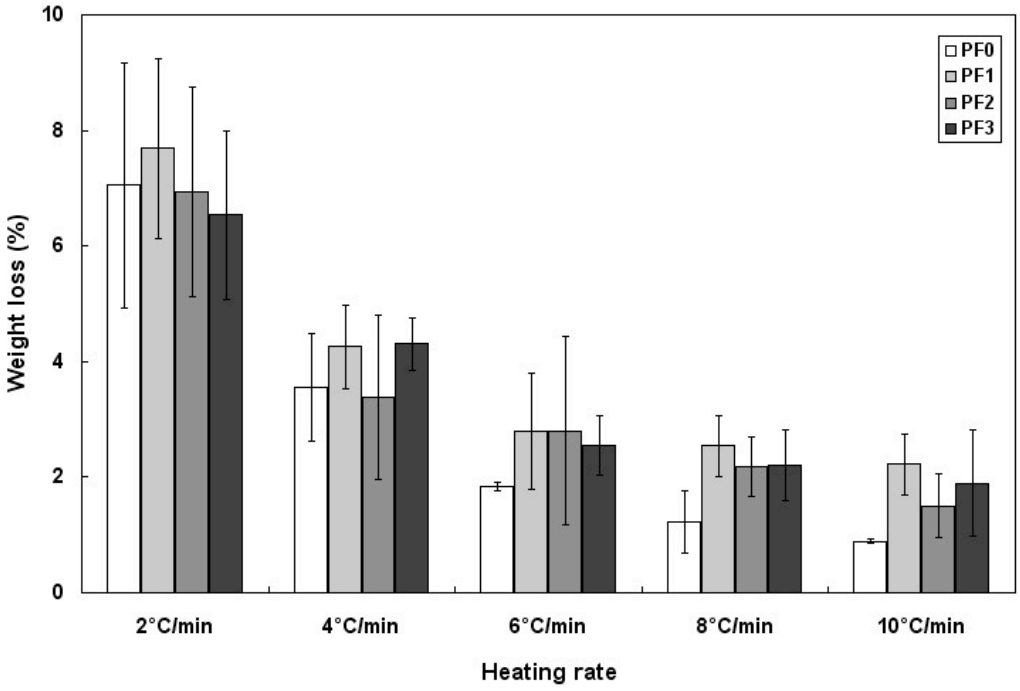

Figure 4.12. Weight loss of the DSC high volume pans during the experiment. Error bars represent ± one standard deviation.

4.5. CONCLUSIONS

With respect to the objective of this study, our conclusions are:

- CNCs accelerate the first stage of resin cure, possibly being the condensation of methylolureas, and the effect is enhanced with increasing CNC content;
- CNCs have a lesser or potentially no effect on the second stage of resin cure, possibly involving methylolphenol and methylolurea condensation and methylolation, and perhaps the formation of hemiformals through reaction of released formaldehyde with cellulose hydroxyl groups;
- Increasing CNC contents cause a greater release of formaldehyde during resin cure, possibly confirming higher condensation rates for methylolureas in the presence of CNCs, leading to a greater number of thermally labile methylene ether linkages.

4.6. REFERENCES

[1] Chow, S. Z. Kinetic study of the polymerization of phenol-formaldehyde resin in the presence of cellulosic materials. Wood Science 1969, 1, 215-221.

[2] Pizzi, A.; Mtsweni, B.; Parsons, W. Wood-induced catalytic activation of PF adhesives autopolymerization vs PF wood covalent bonding. Journal of Applied Polymer Science 1994, 52, 1847-1856.

[3] He, G.; Yan, N. Effect of wood on the curing behavior of commercial phenolic resin systems. Journal of Applied Polymer Science 2005, 95, 185-192.

[4] Lei, Y.; Wu, Q. Cure kinetics of aqueous phenol-formaldehyde resins used for oriented strandboard manufacturing: effect of wood flour. Journal of Applied Polymer Science 2006, 102, 3774-3781.

[5] Mizumachi, H.; Morita, H. Activation energy of the curing reaction of phenolic resin in the presence of woods. Wood Science 1975, 7, 256-260.

[6] He, G.; Riedl, B. Curing kinetics of phenol formaldehyde resin and wood-resin interactions in the presence of wood substrates. Wood Science and Technology 2004, 38, 69-81.

[7] Lu, X.; Pizzi, A. Curing conditions effects on the characteristics of thermosetting adhesives-bonded wood joints - Part 1: Substrate influence on TTT and CHT curing diagrams of wood adhesives. Holz als Roh- und Werkstoff 1998, 56, 339-346.

[8] Pizzi, A.; Lu, X.; Garcia, R. Lignocellulosic substrates influence on TTT and CHT curing diagrams of polycondensation resins. Journal of Applied Polymer Science 1999, 71, 915-925.

[9] Lee, S. Y.; Wu, Q. L.; Strickland, B. The influence of flake chemical properties and zinc borate on gel time of phenolic resin for oriented strandboard. Wood and Fiber Science 2001, 33, 425-436.

[10] He, G.; Yan, N. Effect of wood species and molecular weight of phenolic resins on curing behavior and bonding development. Holzforschung 2005, 59, 635-640.

[11] Johnson, A. C.; Yan, N. Characterizing local curing of liquid phenol-formaldehyde resin on wood surfaces using micro-thermal analysis. Wood Adhesives 2005, San Diego, CA, Nov. 2-4, 2005; pp 171-175.

[12] Pizzi, A. Catalytic activation of wood adhesive polycondensation by the adhesion forces to a cellulosic substrate. International Congress on Adhesion Science and Technology, Invited Papers, Festschrift in Honor of Dr. K. L. Mittal on the Occasion of his 50th Birthday, 1st, Amsterdam, Oct. 16-20, 1995 1998, 531-542.

[13] Beck-Candanedo, S.; Roman, M.; Gray, D. G. Effect of Reaction Conditions on the Properties and Behavior of Wood Cellulose Nanocrystal Suspensions. Biomacromolecules 2005, 6, 1048-1054.

[14] Kissinger, H. E. Reaction Kinetics in Differential Thermal Analysis. Analytical Chemistry 2002, 29, 1702-1706.

[15] Šebenik, A.; Vizovišek, I.; Lapanje, S. Determination of kinetic parameters for the reaction between phenol and formaldehyde by differential scanning calorimetry. European Polymer Journal 1974, 10, 273-278.

[16] Christiansen, A. W.; Gollob, L. Differential scanning calorimetry of phenol-formaldehyde resols. Journal of Applied Polymer Science 1985, 30, 2279-2289.

[17] Tonge, L. Y.; Hodgkin, J.; Blicblau, A. S.; Collins, P. J. Effects of initial phenol-formaldehyde (PF) reaction products on the curing properties of PF resin. Journal of Thermal Analysis and Calorimetry 2001, 64, 721-730.

[18] Holopainen, T.; Alvila, L.; Rainio, J.; Pakkanen, T. T. Phenol-formaldehyde resol resins studied by 13C-NMR spectroscopy, gel permeation chromatography, and differential scanning calorimetry. Journal of Applied Polymer Science 1997, 66, 1183-1193.

[19] Park, B.-D.; Riedl, B.; Bae, H.-J.; Kim, Y. S. Differential scanning calorimetry of phenol-formaldehyde (PF) adhesives. Journal of Wood Chemistry and Technology 1999, 19, 265-286.

[20] Luukko, P.; Alvila, L.; Holopainen, T.; Rainio, J.; Pakkanen, T. T. Effect of alkalinity on the structure of phenol-formaldehyde resol resins. Journal of Applied Polymer Science 2001, 82, 258-262.

[21] Monni, J.; Alvila, L.; Pakkanen, T. T. Structural and physical changes in phenol-formaldehyde resol resin, as a function of the degree of condensation of the resol solution. Industrial & Engineering Chemistry Research 2007, 46, 6916-6924.

[22] Poljansek, I.; Sebenik, U.; Krajnc, M. Characterization of phenol-urea-formaldehyde resin by infine FTIR spectroscopy. Journal of Applied Polymer Science 2006, 99, 2016-2028.

[23] He, G. B.; Yan, N. Influence of the synthesis conditions on the curing behavior of phenol-urea-formaldehyde resol resins. Journal of Applied Polymer Science 2005, 95, 1368-1375.

[24] Lei, Y.; Wu, Q.; Lian, K. Cure kinetics of aqueous phenol-formaldehyde resins used for oriented strandboard manufacturing: analytical technique. Journal of Applied Polymer Science 2006, 100, 1642-1650.

[25] Sellers, T. Plywood and Adhesive Technology. Marcel Dekker: New York, 1985.

[26] Dunky, M. Adhesives in the Wood Industry. In: Handbook of Adhesives Technology; 2nd ed.; Pizzi, A., Mittal, K. L., Eds.; Marcel Dekker: New York, 2003; pp 887-956.

[27] Lee, S. M.; Kim, M. G. Effects of urea and curing catalysts added to the strand board core-layer binder phenol-formaldehyde resin. Journal of Applied Polymer Science 2007, 105, 1144-1155.

[28] Kumlin, K.; Simonson, R. Urea-Formaldehyde Resins .4. Formation of Condensation Products during Resin Preparation. Angewandte Makromolekulare Chemie 1981, 93, 27-42.

[29] Camino, G.; Operti, L.; Trossarelli, L. Mechanism of thermal degradation of urea-formaldehyde polycondensates. Polymer Degradation and Stability 1983, 5, 161-172.

[30] Szesztay, M.; László-Hedvig, Z.; Kovacsovics, E.; Tüdös, F. DSC application for characterization of Urea/formaldehyde condensates. Holz Als Roh-Und Werkstoff 1993, 51, 297-300.

[31] Kumlin, K.; Simonson, R. Urea-Formaldehyde Resins. 3. Formation and Reactions of Monourea Methylol Compounds during Resin Preparation. Angewandte Makromolekulare Chemie 1980, 86, 143-156.

[32] Kottes Andrews, B. A.; Reinhardt, R. M.; Frick, J., J. G.; Bertoniere, N. R. Cellulose Reaction with Formaldehyde and Its Amide Derivatives. In: Formaldehyde Release from Wood Products; Meyer, B., Kottes Andrews, B. A., Reinhardt, R. M., Eds.; ACS Symposium Series 316; American Chemical Society: Washington DC, 1986.

[33] Wakelyn, P. J.; Bertoniere, N. R.; D., F. A.; Thibodeaux, D. P.; Triplett, B. A.; Rousselle, M.-A.; Goynes, J., Wilton R.; Edwards, J. V.; Hunder, L.; McAlister, D. D.; Gamble, G. R. Cotton Fiber Chemistry and Technology. Taylor & Francis: Boca Raton, FL, 2007.

[34] Myers, G. E. Resin Hydrolysis and Mechanisms of Formaldehyde Release from Bonded Wood Products. In: Wood Adhesives in 1985: Status and Needs; Christiansen, A. W., Gillespie, R., Myers, G. E., River, B. H., Eds.; Forest Products Research Society: Madison, WI, 1986.

[35] Welch, C. M.; Margavio, M. F. Activated Imines as Intermediates in Base-Catalyzed Crosslinking of Cotton by N-Methylol Agents. Textile Research Journal 1973, 43, 495-502.

4.7. APPENDIX

4.7.1. Statistical data analysis

4.7.1.1. Activation energy: First exotherm

One-Way ANOVA

Summary Statistics

Dataset	N	Mean	SD	SE
data_PF0firstpeak	27	50.6794	3.52554	0.67849
data_PF1firstpeak	27	46.65213	1.29914	0.25002
data_PF2firstpeak	27	47.91759	2.08167	0.40062
data_PF3firstpeak	27	51.63305	3.28979	0.63312

Null Hypothesis: The means of all selected datasets are equal
Alternative Hypothesis: The means of one or more selected datasets are different

ANOVA

Source	DoF	Sum of Squares	Mean Square	F Value	P Value
Model	3	438.558173	146.186058	19.97537	0.00000
Error	104	761.104850	7.31831586		

At the 0.05 level,
the population means are significantly different.

Means Comparison using Tukey Test

Dataset	Mean	Difference between Means	Simultaneous Confidence Intervals Lower Limit	Upper Limit	Significant at 0.05 Level
data_PF0firstpeak	50.6794				
data_PF1firstpeak	46.65213	4.02727	2.10482	5.94972	Yes
data_PF2firstpeak	47.91759	2.76182	0.83937	4.68427	Yes
data_PF3firstpeak	51.63305	-0.95365	-2.8761	0.96881	No
data_PF1firstpeak	46.65213				
data_PF2firstpeak	47.91759	-1.26545	-3.18791	0.657	No
data_PF3firstpeak	51.63305	-4.98092	-6.90337	-3.05846	Yes
data_PF2firstpeak	47.91759				
data_PF3firstpeak	51.63305	-3.71547	-5.63792	-1.79301	Yes

Power Analysis

Alpha	Total Sample Size	Power
0.5	108	1.00000 (actual)

4.7.1.2. Activation energy: Second exotherm

One-Way ANOVA

Summary Statistics

Dataset	N	Mean	SD	SE
data_PF0secondpeak	27	101.17522	0.7396	0.14234
data_PF1secondpeak	27	100.73858	0.78972	0.15198
data_PF2secondpeak	27	99.72828	1.47392	0.28366
data_PF3secondpeak	27	100.18863	1.13842	0.21909

Null Hypothesis: The means of all selected datasets are equal
Alternative Hypothesis: The means of one or more selected datasets are different

ANOVA

Source	DoF	Sum of Squares	Mean Square	F Value	P Value
Model	3	32.3511177	10.7837059	9.29805	0.00002
Error	104	120.617240	1.15978116		

At the 0.05 level,
the population means are significantly different.

Means Comparison using Tukey Test

Dataset	Mean	Difference between Means	Simultaneous Confidence Intervals Lower Limit	Upper Limit	Significant at 0.05 Level
data_PF0secondpeak	101.17522				
data_PF1secondpeak	100.73858	0.43664	-0.32867	1.20195	No
data_PF2secondpeak	99.72828	1.44694	0.68163	2.21226	Yes
data_PF3secondpeak	100.18863	0.98659	0.22128	1.75191	Yes
data_PF1secondpeak	100.73858				
data_PF2secondpeak	99.72828	1.0103	0.24499	1.77562	Yes
data_PF3secondpeak	100.18863	0.54996	-0.21536	1.31527	No
data_PF2secondpeak	99.72828				
data_PF3secondpeak	100.18863	-0.46035	-1.22566	0.30496	No

Power Analysis

Alpha	Total Sample Size	Power
0.5	108	0.99997 (actual)

4.7.2. Data to Figure 4.7

Table 4.3. Rate constants at different temperatures obtained from the Arrhenius equation using the determined activation energy and frequency factor

Resin mixture	Rate constant (1/s)				
	80 °C	100 °C	120 °C	140 °C	160 °C
First exotherm					
PF0	$1.356 \cdot 10^{-3}$	$3.387 \cdot 10^{-3}$	$7.708 \cdot 10^{-3}$	$1.620 \cdot 10^{-2}$	$3.178 \cdot 10^{-2}$
PF1	$1.588 \cdot 10^{-3}$	$3.715 \cdot 10^{-3}$	$7.972 \cdot 10^{-3}$	$1.589 \cdot 10^{-2}$	$2.971 \cdot 10^{-2}$
PF2	$1.623 \cdot 10^{-3}$	$3.874 \cdot 10^{-3}$	$8.464 \cdot 10^{-3}$	$1.714 \cdot 10^{-2}$	$3.253 \cdot 10^{-2}$
PF3	$1.600 \cdot 10^{-3}$	$4.072 \cdot 10^{-3}$	$9.424 \cdot 10^{-3}$	$2.011 \cdot 10^{-2}$	$4.000 \cdot 10^{-2}$
Second exotherm					
PF0	$3.536 \cdot 10^{-5}$	$2.242 \cdot 10^{-4}$	$1.178 \cdot 10^{-3}$	$5.273 \cdot 10^{-3}$	$2.055 \cdot 10^{-2}$
PF1	$3.609 \cdot 10^{-5}$	$2.269 \cdot 10^{-4}$	$1.184 \cdot 10^{-3}$	$5.262 \cdot 10^{-3}$	$2.038 \cdot 10^{-2}$
PF2	$3.615 \cdot 10^{-5}$	$2.276 \cdot 10^{-4}$	$1.189 \cdot 10^{-3}$	$5.290 \cdot 10^{-3}$	$2.051 \cdot 10^{-2}$
PF3	$3.752 \cdot 10^{-5}$	$2.335 \cdot 10^{-4}$	$1.206 \cdot 10^{-3}$	$5.317 \cdot 10^{-3}$	$2.043 \cdot 10^{-2}$

CHAPTER 5

EFFECTS OF CELLULOSE NANOCRYSTALS ON PHENOL–FORMALDEHYDE ADHESIVE RESINS—PART III: MECHANICAL CURE

5.1. ABSTRACT

The purpose of this study was to determine the effects of cellulose nanocrystals (CNCs) on the mechanical properties of phenol–formaldehyde (PF) resol resins during and after cure. Sandwich-type test specimens were prepared from southern yellow pine strips and four CNC–resin mixtures, containing 0–3 wt % CNCs. The mechanical properties of the test specimens were measured as a function of time and temperature by dynamic mechanical analysis (DMA). The time to incipient storage modulus increase decreased with increasing CNC content. The rate of relative storage modulus increase increased with increasing CNC content. The ultimate sample stiffness increased with increasing CNC content for CNC contents between 0 and 2 wt %. At a CNC content of 3 wt %, the ultimate sample stiffness was lower than at a CNC content of 2 wt % and the second tan δ maximum occurred earlier in the experiment, indicating an earlier onset of vitrification. CNCs were concluded to accelerate the incipient and relative storage modulus increase and to increase the ultimate sample stiffness by mechanical reinforcement of the resin. The lower ultimate sample stiffness at a CNC content of 3 wt % was attributed to premature quenching of the curing reactions through CNC-induced depression of the vitrification point.

5.2. INTRODUCTION

Phenol–formaldehyde (PF) resins are thermosetting adhesives, used extensively in the manufacture of exterior-grade composite wood products, such as exterior-grade plywood, particleboard, and oriented strandboard (OSB) [1, 2]. They are preferred over the less expensive urea–formaldehyde resins because of their superior water and weather resistance. One of the disadvantages of PF resins, with respect to other wood adhesives, such as urea–formaldehyde resins and isocyanate-based adhesives, is their need for longer press times [3]. Because press times are directly related to production rates, shorter press times enable the reduction of production costs.

In Chapter 4, we have shown that the curing reactions of OSB core resin can be accelerated through addition of small amounts (1–3 wt %, based on resin solids) of cellulose nanocrystals, rodlike nanoparticles of cellulose. Our findings were in accordance with previous studies that showed a catalytic effect of cellulose on PF resin curing reactions [4-6]. Their catalytic activity makes cellulose nanocrystals promising candidates as additives for PF adhesive resins. However, because of their large specific surface area, nanoparticles in nanocomposites are known affect many properties of the matrix material [7]. In Chapter 3, we reported on the effect of CNCs on the resin rheology. The addition of CNCs caused a change from Newtonian to non-Newtonian flow behavior and greatly increased the low shear viscosity of the resin.

The purpose of this study was to determine the effects of CNCs on the mechanical properties of PF resol resins during and after cure. To this end, changes in the mechanical properties during cure of four CNC–resin mixtures, containing 0–3 wt % CNCs, based on solids content, were analyzed by dynamic mechanical analysis (DMA). The course of the mechanical property changes during cure contains information about cure progression. Thus, studying the effect of CNCs on the mechanical property changes during cure may enhance our understanding of the mechanisms by which cellulose affects PF resin cure. The resin's mechanical properties after cure are important for the performance of the adhesive. An effect of CNCs on the final mechanical properties of the resin may, therefore, translate into an effect on resin performance.

5.3. EXPERIMENTAL

5.3.1. Materials

Dissolving-grade softwood sulfite pulp (Temalfa 93A-A) was kindly provided by Tembec, Inc. Liquid phenol–formaldehyde resol resin (OSB core resin, 50 wt % solids content, < 0.1 wt % free formaldehyde) was kindly provided by Dynea North America, now Arclin. The resin was stored frozen in 500 mL units until use. Prior to use, the resin was thawed and thoroughly mixed. Sulfuric acid (95.9 wt %, certified) was purchased from Fisher Scientific and used as received. Deionized water (18.2 MΩ·cm) was generated from tap water with a Millipore Direct-Q 5 Ultrapure Water System. Flat sawn southern yellow pine (*Pinus spp.*) boards were purchased from a local wood supplier.

5.3.2. Methods

5.3.2.1. Preparation of resin mixtures

Four CNC–resin mixtures with CNC contents of 0 wt % (PF0), 1 wt % (PF1), 2 wt % (PF2), and 3 wt % (PF3), based on total solids content, were prepared as described in Chapter 3. Briefly, a stable CNC suspension was prepared by hydrolysis of milled wood pulp with 64 wt % sulfuric acid for 60 min at 45.5 °C and an acid-to-pulp ratio of 10 mL/g. The suspension was concentrated to 10 wt % with a rotary evaporator (Büchi Rotavapor R-200) using a water bath temperature of 40 °C. Different amounts of the CNC suspension and deionized water were slowly added under stirring (500 rpm) to the PF resin. Stirring was continued for 10 min to ensure good mixing. The respective amounts of CNC suspension and deionized water were chosen to maintain an equal solids content of 44.64 wt % in the four resin mixtures. The pH of the resin mixtures decreased slightly with increasing CNC content from 12.30 ± 0.01 at 0 wt % to 12.27 ± 0.02 at 3 wt %. No fillers, extenders, or any other additives were added in this study.

5.3.2.2. Preparation of test specimens

Sandwich-type DMA specimens were prepared from planed southern yellow pine strips with dimensions of 35 × 6 × 0.6 mm (L × T × R), conditioned at 20 °C and 65% relative humidity for a minimum of 2 weeks (estimated moisture content: ~10%). The conditioned wood strips were stored in sealed plastic bags prior to specimen assembly. Approximately 40–45 mg of resin mixture was applied with a syringe to the bonding surfaces of two strips and spread uniformly. Immediately thereafter, the two bonding surfaces were mated under application of light pressure and mounted in the DMA sample holder. The instrument had been programmed prior to specimen preparation so that the time between application of the resin and start of the measurement was less than 3 min.

5.3.2.3. Dynamic mechanical analysis

DMA measurements were performed in three-point bending mode (Figure 5.1) using a TA Instruments DMA 2980. The oscillation frequency was 1 Hz and the preload force was 0.02 N. An oscillation amplitude of 20 µm was chosen based on prior strain sweep test. The temperature was ramped from 25 to 150 °C at a rate of 25 °C/min and then held isothermal at 150 °C for 30 min. The upper temperature limit was chosen based on the thermal degradation behavior of the CNCs, discussed in Chapter 3. Each measurement was performed in quintuplicate.

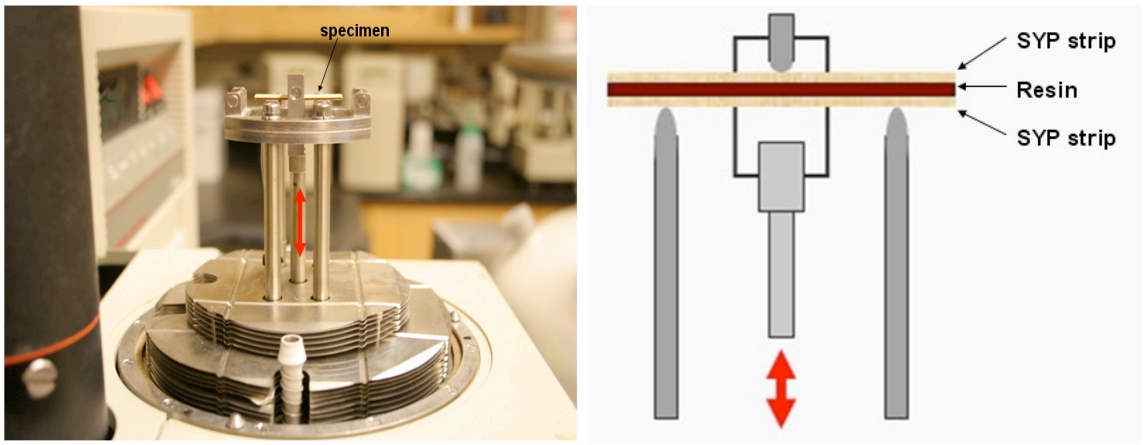

Figure 5.1. Set-up of the three point bending test using sandwich-type specimen.

5.4. RESULTS AND DISCUSSION

Figure 5.2 shows the changes in storage modulus and tan δ during cure for the neat resin sample (PF0) as well as the temperature profile of the DMA experiment. In the first five minutes of the experiment, the temperature increased linearly to approximately 130 °C. During this time, the sample softened slightly, as indicated by the decrease in storage modulus.

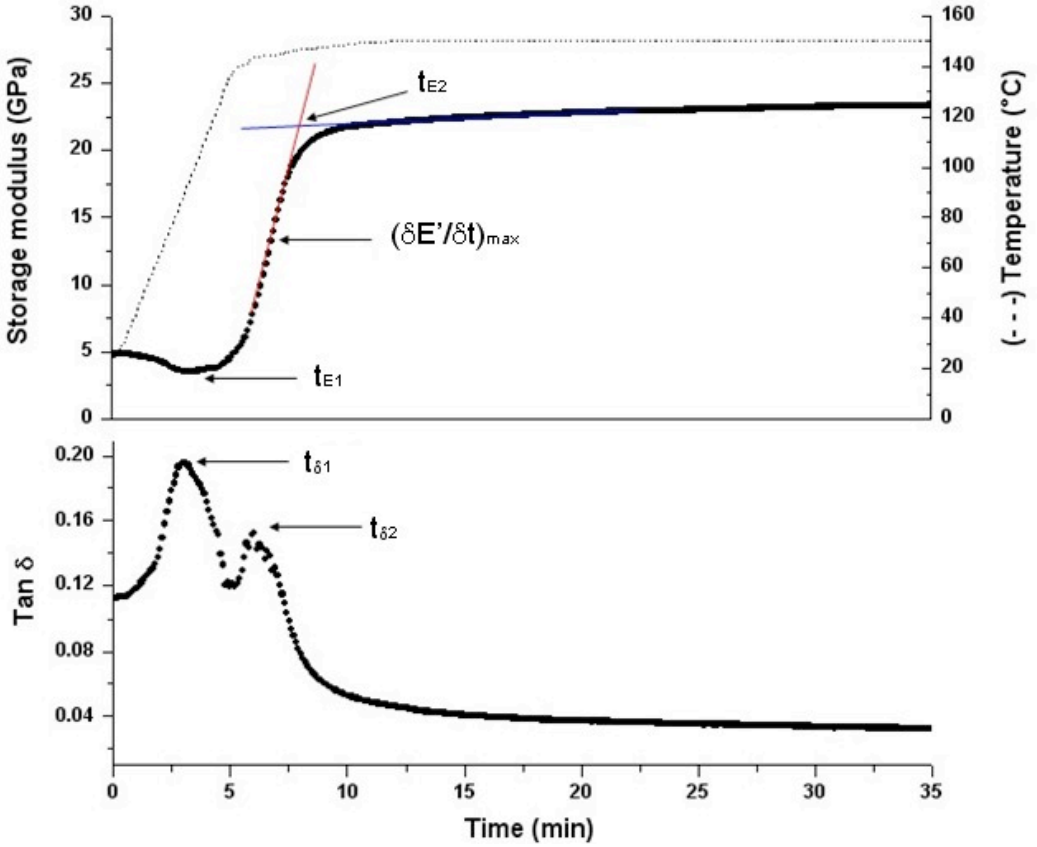

Figure 5.2. Storage modulus and tan δ values for PF0 as a function of time, and temperature profile of the DMA experiment.

This initial softening could have several reasons. The wood strips might have softened because of thermal transitions in the polymeric wood components. However, when tested, a wood strip twice as thick as those used in the sandwich-type samples, and conditioned in the same way, showed only a very small decrease in storage modulus

below 130 °C upon heating. Therefore, thermal transitions of the wood components most likely played a minor role in the initial sample softening. Another possible reason could be a decrease in resin viscosity upon heating, which would lower the sample's resistance to bending. A third and possibly related reason could be a softening of the wood strips upon penetration of the resin into the wood, possibly promoted by a decrease in resin viscosity.

Upon reaching a temperature of about 130 °C, the heating rate decreased. The hold temperature of 150 °C was reached approximately twelve minutes into the experiment. After the initial decrease in storage modulus, the storage modulus of the sample increased rapidly upon further heating and then leveled off shortly before the hold temperature was reached. During the isothermal period of the experiment, the storage modulus increased only slightly. Thus, resin crosslinking occurred primarily in the temperature range 130–150 °C. For a quantitative comparison of storage modulus curves, three curve characteristics were selected as proposed by Lee and Kim [8] (Figure 5.2): the time at which the storage modulus starts to increase, t_{E1}, the maximum slope of the storage modulus curve, $(\delta E'/\delta t)_{max}$, and the time at which the inflection tangent intersects the tangent to the plateau, t_{E2}.

The tan δ curve for PF0 (Figure 5.2, bottom) exhibited two maxima, as frequently observed for thermosetting resins [9-11]. In early studies of the isothermal cure behavior of thermosetting resins by dynamic mechanical techniques, the first maximum in damping curves was interpreted as the gel point [9, 12], i.e. the instance of formation of an infinitely large three-dimensional network. The gel point marks a critical extent of reaction and depends only on the functionality, reactivity, and stoichiometry of the reactive species, but not on temperature, amount of catalyst, etc. [13, 14]. A study by Stutz and Mertes [10], however, challenged this interpretation of the first tan δ maximum by showing that the glass transition temperature, T_g, of the resin at that maximum depended on the cure temperature, which should not be the case if the maximum represented gelation of the resin. The study further showed that the viscosity at the first damping maximum was the same for resin samples cured at different temperatures. The first damping maximum was therefore attributed to an isoviscous state at which the

relaxation time for viscous flow becomes equal to half the period of oscillation. It was argued that, at this point, viscous flow of the resin ceases and the system changes its damping characteristics. In accordance with these findings, it is now commonly accepted that gelation during an isothermal cure experiment is marked by a frequency independence of tan δ [15, 16]. The second tan δ maximum during isothermal cure of thermosetting resins, or more generally the tan δ maximum that coincides with the inflection of the storage modulus curve, is commonly attributed to resin vitrification [12, 17], i.e. the transition from a rubbery to a glassy state as the T_g of the reacting system reaches the cure temperature. By measuring the T_g of resins cured to the second tan δ maximum, Stutz and Mertes confirmed the close association of the tan δ maximum with resin vitrification [10]. The maximum was, however, found to indicate vitrification somewhat too early. In accordance with Stutz and Mertes's findings, Lange et al. [18, 19] observed that the tan δ maximum marked the onset of a change in specific heat capacity, indicative of a change in molecular mobility and, thus, vitrification [20]. In light of these studies, we attributed the first tan δ maximum to a state at which the viscosity of the resin mixture reaches a critical level and the second to the onset of vitrification.

Figure 5.3 shows the storage modulus and tan δ curves for the four resin mixtures. Each curve is an average of five observations. The initial storage modulus was noticeably higher for PF3 than for PF0. PF1 and PF2 showed intermediate values. In Chapter 3, we reported that the steady-state shear viscosity of the resin increased strongly with increasing CNC content. The steady-state shear viscosity of PF3 at a shear rate of 1 s^{-1} was approximately 15 times higher than that of PF0. The higher initial storage modulus values at higher CNC contents could, therefore, be due to the higher viscosities of the resin mixtures. All resin mixtures showed the initial sample softening followed by a rapid increase in storage modulus and a leveling off before the hold temperature was reached. The start of the storage modulus increase and the leveling off of the storage modulus occurred progressively earlier as the CNC content of the resin increased.

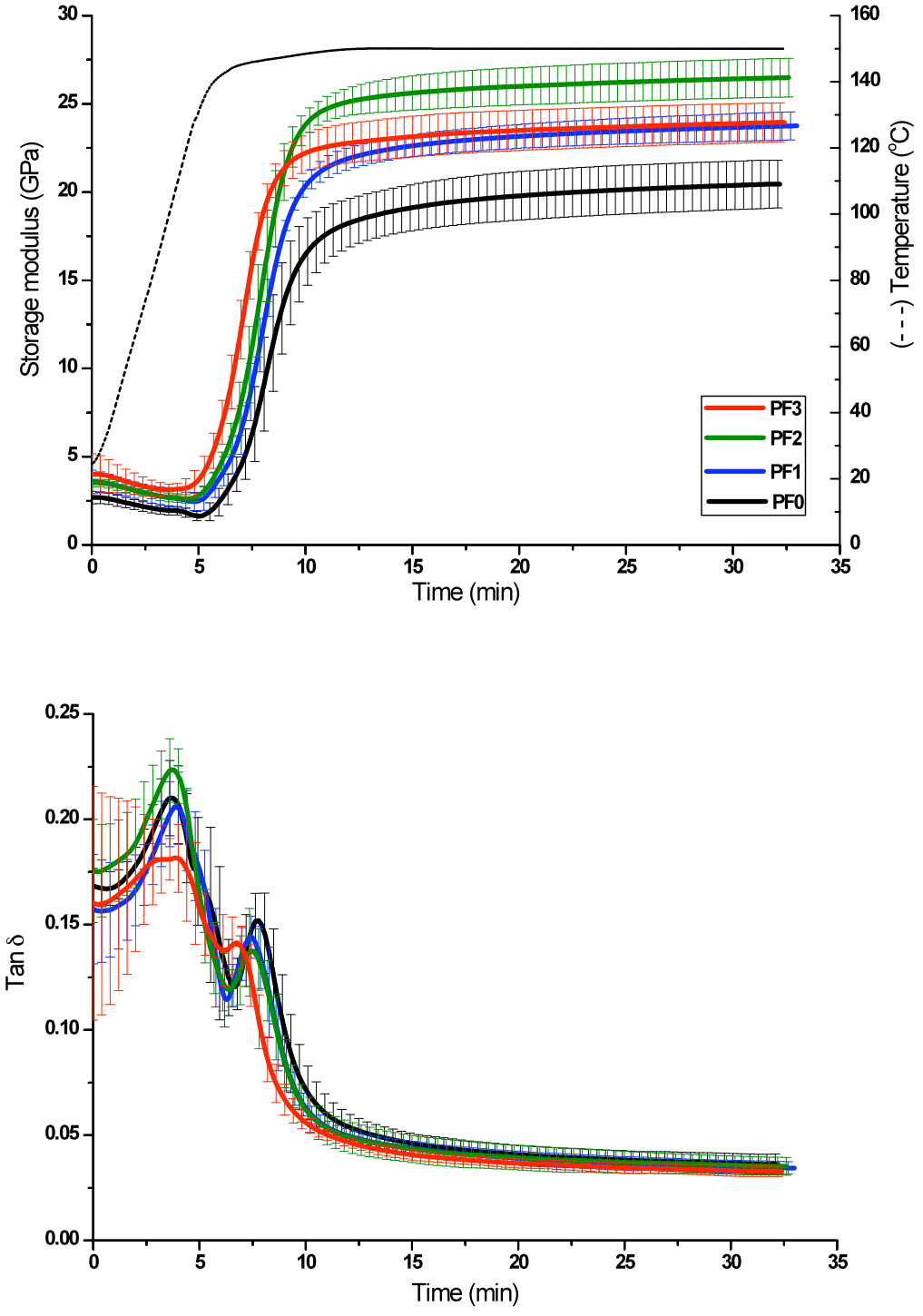

Figure 5.3. Mean values of the storage modulus and tan δ, from five observations, for the four resin mixtures as a function of time. The top figure also shows a typical temperature profile. Error bars represent ± one standard deviation.

This trend is more apparent in Figure 5.4, which compares the mean values of t_{E1} and t_{E2} for the four resin mixtures (for the statistical analysis results of the data see Appendices 5.6.1. and 5.6.2). Both, t_{E1} and t_{E2}, decreased with increasing CNC content. t_{E1} and t_{E2} of PF3 were 23 and 15% lower, respectively, than t_{E1} and t_{E2} of PF0. The absolute decrease of t_{E1} was nearly the same as that of t_{E2}, namely 1.2 and 1.4 min, respectively, indicating that the decrease in t_{E2} was mainly due to the decrease in t_{E1}. In other words, the CNCs reduced the time to the incipient storage modulus increase but had a minor effect on the duration of cure, i.e. the time period from t_{E1} to t_{E2}.

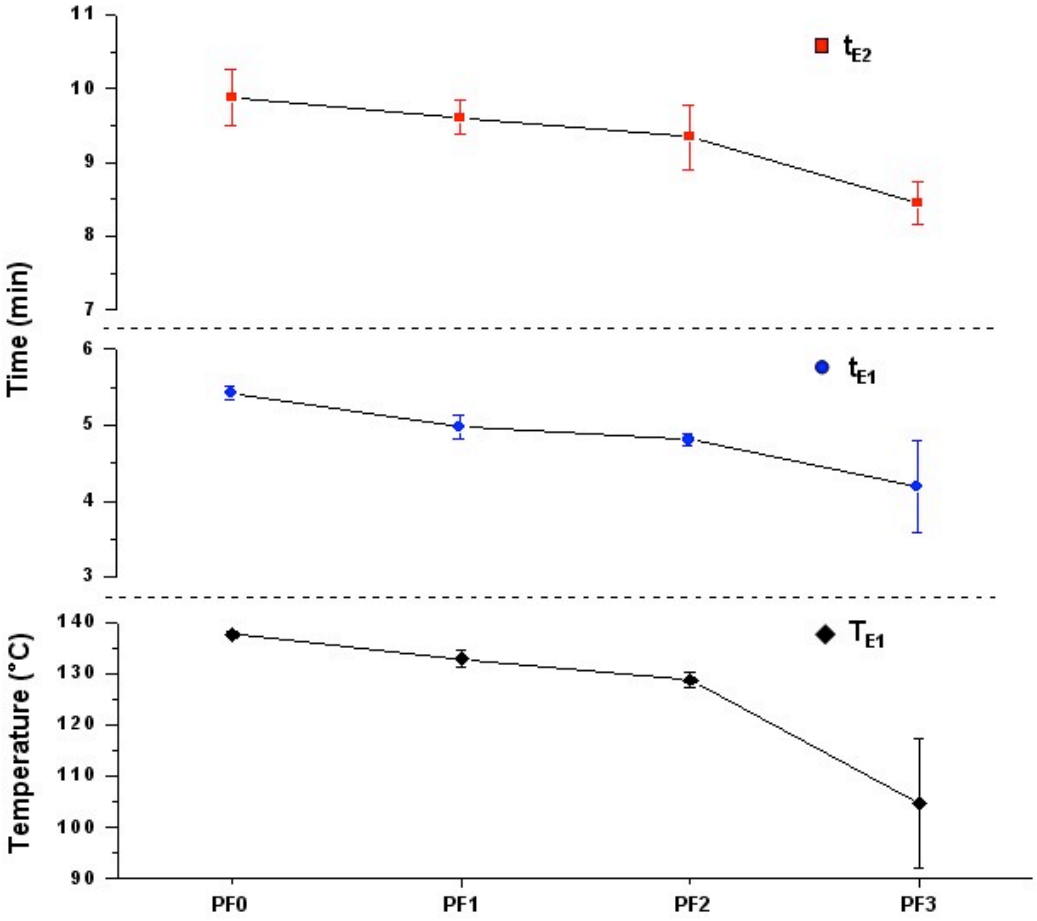

Figure 5.4. t_{E1}, t_{E2}, and T_{E1} values for the four resin mixtures. Error bars represent ± one standard deviation.

Figure 5.4 also shows the mean values of the temperatures at t_{E1}, T_{E1} (for the statistical analysis results of the data see Appendix 5.6.3). T_{E1} decreased from 138 °C for PF0 to 105 °C for PF3. The value for PF3, however, was unexpectedly low. In a previous study of the cure kinetics of the resin mixtures by DSC (Chapter 4), we observed the first exothermic event during PF3 cure at a peak temperature of 112 °C, using a heating rate of 10 °C/min. It is therefore surprising that the PF3 storage modulus started to increase already at a temperature of 105 °C, in particular that the heating rate in the DMA experiments at t_{E1} was 2.5 times higher than in the previous DSC experiments and should therefore cause a greater thermal lag. A possible reason for the early onset of the storage modulus increase could be the evaporation of water, which was largely suppressed in the DSC experiments through the use of sealed high-volume sample pans was not suppressed in the DMA experiments.

Figure 5.5 compares the mean values of $(\delta E'/\delta t)_{max}$ and the maximum storage modulus, E'_{max}, for the four resin mixtures (for the statistical analysis results of the data see Appendices 5.6.4 and 5.6.5).

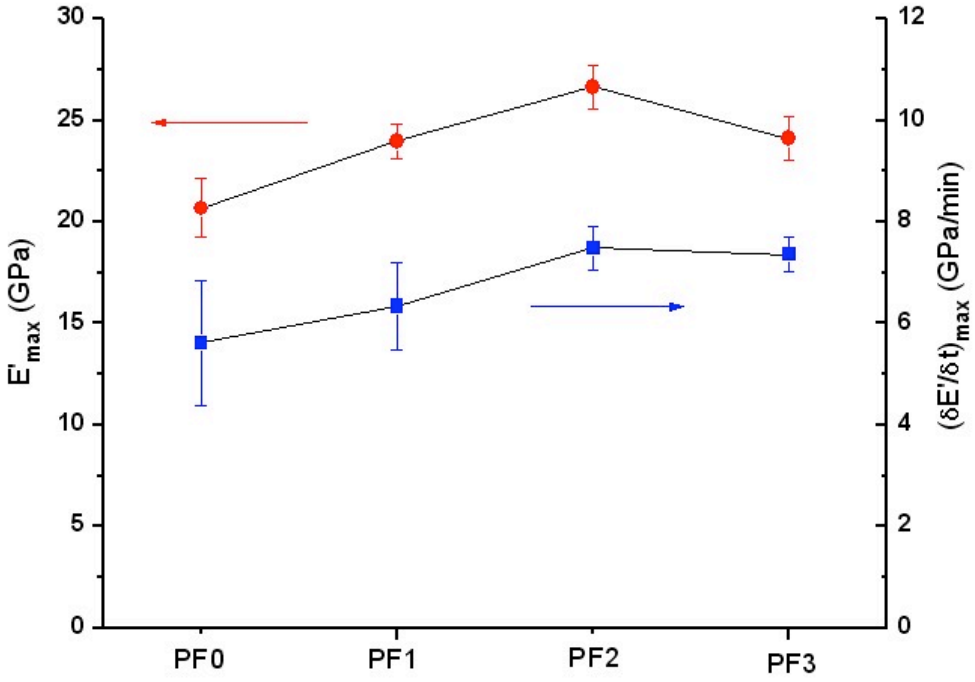

Figure 5.5. E'_{max} and $(\delta E'/\delta t)_{max}$ values for the four resin mixtures. Error bars represent ± one standard deviation.

Both, $(\delta E'/\delta t)_{max}$ and E'_{max}, increased from PF0 to PF2. Thus, up to a CNC content of 2 wt %, increasing amounts of CNCs caused a more rapid stiffness increase and a higher ultimate sample stiffness. The trend did not, however, extend to PF3, which showed a $(\delta E'/\delta t)_{max}$ comparable to that obtained for PF2 and an E'_{max} comparable to that obtained for PF1. In relative terms, however, PF3 showed the fastest storage modulus increase of the four resin mixtures. Figure 5.6 shows the storage modulus curves for the four resin mixtures normalized according to

$$E'_{rel}(t) = \frac{E'(t) - E'_{max}}{E'_{max} - E'_{min}} \qquad [5.1]$$

where $E'(t)$ is the storage modulus at time t and E'_{min} is the minimum storage modulus [21]. At a cure time of 8 min, PF3 was at 75% of its final stiffness whereas PF0 had only reached 38%. PF1 and PF2 were at 45 and 52%, respectively. Thus, a higher CNC content caused a more rapid relative storage modulus increase.

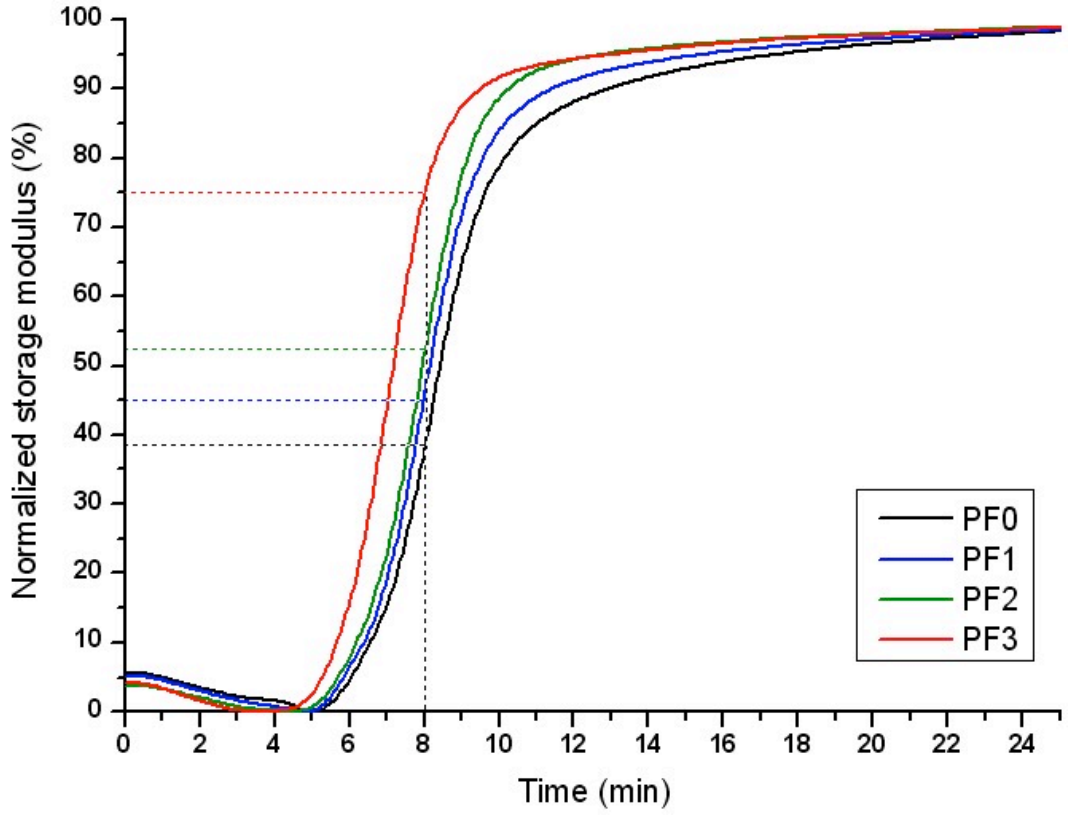

Figure 5.6. Relative storage modulus for the four resin mixtures as a function of time.

The E'_{max} values for the four resin mixtures (Figure 5.5) were likely governed by two factors: the CNC content and the degree of crosslinking in the resin. CNCs are immensely rigid, possessing an elastic modulus in excess of 100 GPa [22]. Provided that the surface of the CNCs was wetted by the resin, i.e. that there was intimate contact between the resin and the CNCs at the interface, the rod-like nanoparticles likely increased the flexural stiffness of the resin mixtures. Wetting of the CNC surface by the resin was assumed based on results of molecular mechanics simulations by Pizzi et al. [23-26]. The authors demonstrated that PF dimers [23] and oligomers [24] and urea–formaldehyde oligomers [25, 26] adsorbed onto cellulose surfaces and interacted with these surfaces through van der Waals forces and hydrogen bonding. That the CNCs caused an increase in the degree of resin crosslinking and thereby affected an increase in E'_{max} was less likely. As discussed in Chapter 4, the cellulose hydroxyl groups did likely not undergo any chemical reactions with the resin components other than the reversible formation of hemiformals with formaldehyde, released in the curing process. An increase in the degree of resin crosslinking by the CNCs would therefore have to rely on catalytic effects and be restricted to areas in the resin near the CNC surface. Because an increase in the degree of resin crosslinking by the CNCs is less likely, the observed increase in E'_{max} from PF0 to PF2 was attributed to a mechanical reinforcing effect of the CNCs.

However, since there was no obvious reason for a weakening of the reinforcing effect upon further increase of the CNC content from 2 to 3 wt %, the sudden decrease in E'_{max} from PF2 to PF3 must be due to a lower degree of crosslinking in PF3 with respect to PF2. The rate of crosslinking during resin cure depends on the rates of the individual chemical reactions and the rates of diffusion of the chemical species to the reaction sites. Before vitrification, the rates of diffusion are higher than the reaction rates, making the chemical reactions the rate-limiting step. After vitrification, the rates of diffusion are much lower than the reaction rates, making diffusion through the glassy network the rate-limiting step. Thus, cure proceeds much slower in a vitrified resin than in a resin of liquid or rubbery state. A lower ultimate degree of crosslinking could therefore be the result of an earlier onset of vitrification and premature quenching of the crosslinking reactions. For further discussion of this possibility, we turn our attention to the tan δ maxima.

Figure 5.7 compares the mean cure times at the first and second tan δ maximum, $t_{\delta 1}$ and $t_{\delta 2}$, respectively, for the four resin mixtures. As discussed above, $t_{\delta 1}$ is taken to indicate a state at which the viscosity of the resin reaches a critical level and $t_{\delta 2}$ the onset of vitrification.

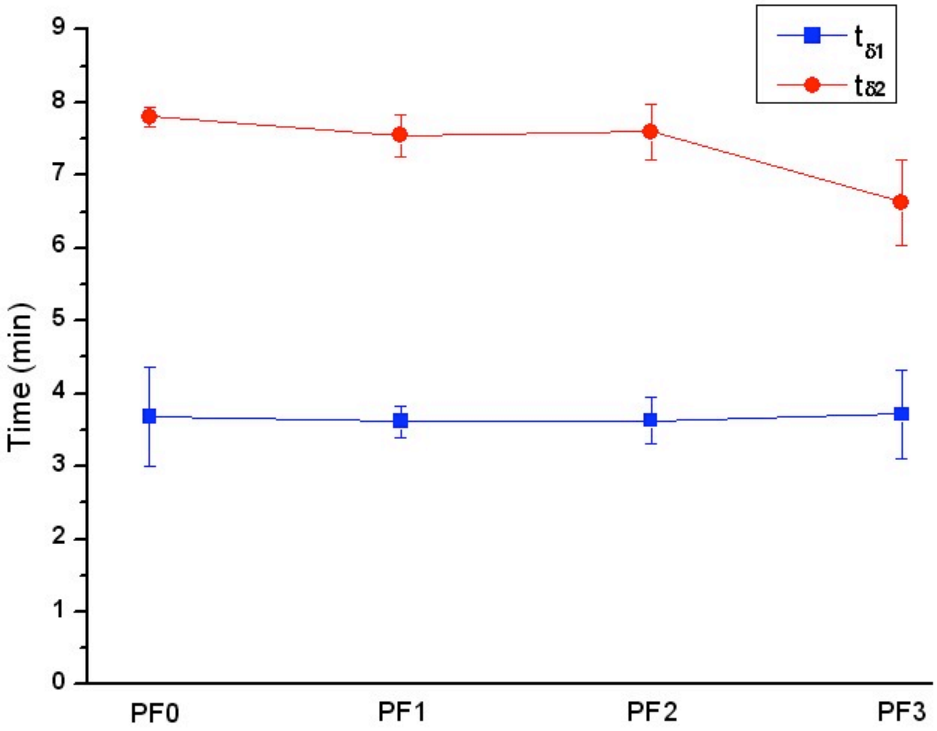

Figure 5.7. $t_{\delta 1}$ and $t_{\delta 2}$ values for the four resin mixtures. Error bars represent ± one standard deviation.

$t_{\delta 1}$ appeared to be unaffected by the CNCs. This result is surprising considering the increase in resin viscosity with increasing CNC content (Chapter 3). The effect of the CNCs on $t_{\delta 1}$ might have been obscured by the mechanical properties of the substrate or the large variation in the tan δ data for each sample, particularly during the initial period of the experiment, possibly due to the evaporation of water. $t_{\delta 2}$ was unaffected by the CNCs up to a CNC content of 2 wt %. The $t_{\delta 2}$ value for PF3, however, was noticeably lower, confirming an earlier onset of vitrification.

There are two possible ways by which the CNCs could lower $t_{\delta 2}$: (a) the nanoparticles could accelerate the cure reactions so that T_g rises more rapidly and

therefore reaches the rising cure temperature earlier or (b) the nanoparticles could restrict the molecular motions in the resin so that the glassy region in time–temperature diagrams [27-30] expands to lower temperatures. Nanoparticles are known to either raise or lower the T_g of thermoplastic polymers or leave it unchanged, depending on the polymer–nanoparticle interactions [7, 31]. A decrease in T_g is observed when the polymer shows poor wetting of the nanoparticle surface, resulting in free volume at the polymer–nanoparticle interface. When the polymer does wet the nanoparticle surface, T_g is increased if attractive polymer–nanoparticles interactions exist that restrict the molecular motions of the polymer molecules. As mentioned above, molecular mechanics simulations by Pizzi et al. have indicated attractive van der Waals and hydrogen bonding forces between a crystalline cellulose surface and PF and urea–formaldehyde dimers and oligomers [23-26]. Thus, it is conceivable that the molecular mobility of the resin molecules was affected by interactions at the CNC surface. Concerning the alternative possibility, i.e. that the CNCs accelerated the cure reactions in the resin, we showed in a prior study of the cure of the resin mixtures by DSC (Chapter 4) that the CNCs accelerated the first exothermic event, attributed to the condensation of methylolurea species in the commercial resol resin, but had little effect on the second one, attributed to the condensation of methylolphenols, the reaction of the liberated formaldehyde with unreacted or partially methylolated urea, and the condensation of the newly formed methylolureas. Though the final degree of reaction conversion, as measured by the total heat of reaction, appeared to be unaffected by the CNCs, the study nevertheless provided evidence for an accelerating effect of the CNCs on some of the curing reactions. Therefore, either of the two mechanisms or a combination of both might have caused the observed decrease in $t_{\delta 2}$.

Table 5.1 lists the mean temperatures at t_{E2} and $t_{\delta 2}$, denoted T_{E2} and $T_{\delta 2}$, respectively, for the four resin mixtures.

Table 5.1. T_{E2} and $T_{\delta 2}$ for the four resin mixtures

	PF0	PF1	PF2	PF3
T_{E2} (°C)	148.4 ± 0.5	148.0 ± 0.3	147.9 ± 0.7	146.5 ± 0.8
$T_{\delta 2}$ (°C)	146.1 ± 0.4	145.6 ± 0.5	145.9 ± 0.5	143.5 ± 1.1

T_{E2} stayed at ~148 °C and $T_{\delta 2}$ at ~146 °C for PF0, PF1, and PF2 and dropped to 146.5 and 143.5 °C, respectively, for PF3. Assuming a close correlation of these values with the vitrification temperature, the vitrification temperature of PF3 was lower than that of PF0 by ~2 °C. The vitrification point might have been affected also in PF1 and PF2 but the reinforcing effect of the CNCs might have dominated the effect of the CNCs on E'_{max}, resulting in a net increase with respect to the value for PF0. The E'_{max} of PF3 was higher than that of PF0, supporting a reinforcing effect of the CNCs, but lower than that of PF2, indicating a lower degree of resin crosslinking.

5.5. CONCLUSIONS

With respect to the objective of this study, our conclusions are:

- CNCs accelerate the incipient and relative storage modulus increase, and these effects strengthen with increasing CNC content;
- Increasing CNC contents cause an increase in ultimate sample stiffness through mechanical reinforcement of the resin by the CNCs;
- At high enough CNC contents, CNCs lower the vitrification point, resulting in reduced ultimate sample stiffness, possibly due to premature quenching of the curing reactions, leading to lower crosslinking densities.

5.6. REFERENCES

[1] Pizzi, A. Phenolic Resin Adhesives. In: Handbook of Adhesives Technology; 2nd ed.; Pizzi, A., Mittal, K. L., Eds.; Marcel Dekker: New York, 2003; pp 541-571.

[2] Gardziella, A.; Pilato, L.; Knop, A. Phenolic Resins: Chemistry, Applications, Standardization, Safety and Ecology. 2nd ed.; Springer: Heidelberg, Germany, 1999.

[3] Dunky, M. Adhesives in the Wood Industry. In: Handbook of Adhesives Technology; 2nd ed.; Pizzi, A., Mittal, K. L., Eds.; Marcel Dekker: New York, 2003; pp 887-956.

[4] Chow, S. Z. Kinetic study of the polymerization of phenol-formaldehyde resin in the presence of cellulosic materials. Wood Science 1969, 1, 215-221.

[5] Pizzi, A. Catalytic activation of wood adhesive polycondensation by the adhesion forces to a cellulosic substrate. International Congress on Adhesion Science and Technology, Invited Papers, Festschrift in Honor of Dr. K. L. Mittal on the Occasion of his 50th Birthday, 1st, Amsterdam, Oct. 16-20, 1995 1998, 531-542.

[6] Pizzi, A.; Mtsweni, B.; Parsons, W. Wood-induced catalytic activation of PF adhesives autopolymerization vs PF wood covalent bonding. Journal of Applied Polymer Science 1994, 52, 1847-1856.

[7] Paul, D. R.; Robeson, L. M. Polymer nanotechnology: Nanocomposites. Polymer 2008, 49, 3187-3204.

[8] Lee, S. M.; Kim, M. G. Effects of urea and curing catalysts added to the strand board core-layer binder phenol-formaldehyde resin. Journal of Applied Polymer Science 2007, 105, 1144-1155.

[9] Babayevsky, P. G.; Gillham, J. K. Epoxy thermosetting systems. Dynamic mechanical analysis of the reactions of aromatic diamines with the diglycidyl ether of bisphenol A. Journal of Applied Polymer Science 1973, 17, 2067-88.

[10] Stutz, H.; Mertes, J. Torsional Braid Analysis and Gelation in Thermoset Resins. Journal of Applied Polymer Science 1989, 38, 781-787.

[11] Bilyeu, B.; Brostow, W. Separation of gelation from vitrification in curing of a fiber-reinforced epoxy composite. Polymer Composites 2002, 23, 1111-1119.

[12] Lewis, A. F. Dynamic Mechanical Behavior During the Thermosetting Curing Process. SPE Transactions 1963, 7, 201-209.

[13] Flory, P. J. Molecular Size Distribution in Three Dimensional Polymers. I. Gelation. Journal of the American Chemical Society 1941, 63, 3083-3090.

[14] Flory, P. J. Principles of polymer chemistry. Cornell University Press: Ithaca, NY, 1953; pp. 351-???

[15] Winter, H. H.; Mours, M. Rheology of polymers near liquid-solid transitions. In: Neutron Spin Echo Spectroscopy Viscoelasticity Rheology; Advances in Polymer Science 134; Springer-Verlag: Berlin, 1997; pp 165-234.

[16] Muller, R.; Gérard, E.; Dugand, P.; Rempp, P.; Gnanou, Y. Rheological Characterization of the Gel Point: A New Interpretation. Macromolecules 1991, 24, 1321-1326.

[17] Kim, M. G.; Nieh, W. L. S.; Meacham, R. M. Study on the Curing of Phenol-Formaldhehyde Resol Resins by Dynamic Mechanical Analysis. Industrial & Engineering Chemistry Research 1991, 30, 798-803.

[18] Lange, J.; Altmann, N.; Kelly, C. T.; Halley, P. J. Understanding vitrification during cure of epoxy resins using dynamic scanning calorimetry and rheological techniques. Polymer 2000, 41, 5949-5955.

[19] Lange, J.; Ekelöf, R.; St. John, N. A.; George, G. A. Transitions, Properties, and Molecular Mobility During Cure of Thermosetting Resins. In: Structure and Properties of Glassy Polymers; Tant, M. R., Hill, A. J., Eds.; ACS Symposium Series 710; American Chemical Society: Washington, DC, 1998.

[20] VanAssche, G.; VanHemelrijck, A.; Rahier, H.; VanMele, B. Modulated differential scanning calorimetry: Isothermal cure and vitrification of thermosetting systems. Thermochimica Acta 1995, 268, 121-142.

[21] Vazquez, G.; Lopez-Suevos, F.; Gonzalez-Alvarez, J.; Antorrena, G. Curing process of phenol-urea-formaldehyde-tannin (PUFT) adhesives - Kinetic studies by DSC and DMA. Journal of Thermal Analysis and Calorimetry 2005, 82, 143-149.

[22] Iwamoto, S.; Kai, W. H.; Isogai, A.; Iwata, T. Elastic Modulus of Single Cellulose Microfibrils from Tunicate Measured by Atomic Force Microscopy. Biomacromolecules 2009, 10, 2571-2576.

[23] Pizzi, A.; Eaton, N. J. A conformational analysis approach to phenol-formaldehyde resins adhesion to wood cellulose. Journal of Adhesion Science and Technology 1987, 1, 191-200.

[24] Pizzi, A.; Maboka, S. Calculated values of the adhesion of phenol formaldehyde oligomers to crystalline cellulose-II. Journal of Adhesion Science and Technology 1993, 7, 81-93.

[25] Pizzi, A. A molecular mechanics approach to the adhesion of urea-formaldehyde resins to cellulose. 1. Crystalline Cellulose-I. Journal of Adhesion Science and Technology 1990, 4, 573-588.

[26] Pizzi, A. A Molecular Mechanics Approach to the Adhesion of Urea Formaldehyde Resins to Cellulose. 2. Amorphous vs Crystalline Cellulose-I. Journal of Adhesion Science and Technology 1990, 4, 589-595.

[27] Gillham, J. K. The TBA torsion pendulum: a technique for characterizing the cure and properties of thermosetting systems. Polymer International 1997, 44, 262-276.

[28] Pizzi, A.; Zhao, C.; Kamoun, C.; Heinrich, H. TTT and CHT curing diagrams of water-borne polycondensation resins on lignocellulosic substrates. Journal of Applied Polymer Science 2001, 80, 2128-2139.

[29] Lu, X.; Pizzi, A. Curing conditions effects on the characteristics of thermosetting adhesives-bonded wood joints - Part 1: Substrate influence on TTT and CHT curing diagrams of wood adhesives. Holz als Roh- und Werkstoff 1998, 56, 339-346.

[30] Pizzi, A.; Lu, X.; Garcia, R. Lignocellulosic substrates influence on TTT and CHT curing diagrams of polycondensation resins. Journal of Applied Polymer Science 1999, 71, 915-925.

[31] Rittigstein, P.; Torkelson, J. M. Polymer-nanoparticle interfacial interactions in polymer nanocomposites: Confinement effects on glass transition temperature and suppression of physical aging. Journal of Polymer Science Part B-Polymer Physics 2006, 44, 2935-2943.

5.7. APPENDIX

5.7.1. Statistical analysis of the t_{E1} values

One-Way ANOVA

Summary Statistics

Dataset	N	Mean	SD	SE
geltime_PF0	5	5.42	0.09192	0.04111
geltime_PF1	5	4.976	0.15356	0.06867
geltime_PF2	5	4.808	0.06834	0.03056
geltime_PF3	5	4.194	0.61272	0.27402

Null Hypothesis: The means of all selected datasets are equal
Alternative Hypothesis: The means of one or more selected datasets are different

ANOVA

Source	DoF	Sum of Squares	Mean Square	F Value	P Value
Model	3	3.86437500	1.28812500	12.50212	0.00018
Error	16	1.64852000	0.103032500		

At the 0.05 level,
the population means are significantly different.

Means Comparison using Tukey Test

Dataset	Mean	Difference between Means	Simultaneous Confidence Intervals Lower Limit	Upper Limit	Significant at 0.05 Level
geltime_PF0	5.42				
geltime_PF1	4.976	0.444	-0.13681	1.02481	No
geltime_PF2	4.808	0.612	0.03119	1.19281	Yes
geltime_PF3	4.194	1.226	0.64519	1.80681	Yes
geltime_PF1	4.976				
geltime_PF2	4.808	0.168	-0.41281	0.74881	No
geltime_PF3	4.194	0.782	0.20119	1.36281	Yes
geltime_PF2	4.808				
geltime_PF3	4.194	0.614	0.03319	1.19481	Yes

Power Analysis

Alpha	Total Sample Size	Power
0.5	20	1.00000 (actual)

5.7.2. Statistical analysis of the t_{E2} values

One-Way ANOVA

Summary Statistics

Dataset	N	Mean	SD	SE
curetime_PF0	5	9.886	0.38436	0.17189
curetime_PF1	5	9.614	0.22843	0.10216
curetime_PF2	5	9.35	0.43744	0.19563
curetime_PF3	5	8.446	0.28112	0.12572

Null Hypothesis: The means of all selected datasets are equal
Alternative Hypothesis: The means of one or more selected datasets are different

ANOVA

Source	DoF	Sum of Squares	Mean Square	F Value	P Value
Model	3	5.85752000	1.95250667	16.60683	0.00004
Error	16	1.88116000	0.117572500		

At the 0.05 level,
the population means are significantly different.

Means Comparison using Tukey Test

Dataset	Mean	Difference between Means	Simultaneous Confidence Intervals Lower Limit	Upper Limit	Significant at 0.05 Level
curetime_PF0	9.886				
curetime_PF1	9.614	0.272	-0.34843	0.89243	No
curetime_PF2	9.35	0.536	-0.08443	1.15643	No
curetime_PF3	8.446	1.44	0.81957	2.06043	Yes
curetime_PF1	9.614				
curetime_PF2	9.35	0.264	-0.35643	0.88443	No
curetime_PF3	8.446	1.168	0.54757	1.78843	Yes
curetime_PF2	9.35				
curetime_PF3	8.446	0.904	0.28357	1.52443	Yes

Power Analysis

Alpha	Total Sample Size	Power
0.5	20	1.00000 (actual)

5.7.3. Statistical analysis of the T_{E1} values

One-Way ANOVA

Summary Statistics

Dataset	N	Mean	SD	SE
geltemp_PF0	5	137.74964	0.48823	0.21834
geltemp_PF1	5	132.93058	1.72677	0.77224
geltemp_PF2	5	128.88016	1.56211	0.6986
geltemp_PF3	5	104.77646	12.48629	5.58404

Null Hypothesis: The means of all selected datasets are equal
Alternative Hypothesis: The means of one or more selected datasets are different

ANOVA

Source	DoF	Sum of Squares	Mean Square	F Value	P Value
Model	3	3223.96378	1074.65459	26.60565	0.00000
Error	16	646.271431	40.3919645		

At the 0.05 level,
the population means are significantly different.

Means Comparison using Tukey Test

Dataset	Mean	Difference between Means	Simultaneous Confidence Intervals Lower Limit	Upper Limit	Significant at 0.05 Level
geltemp_PF0	137.74964				
geltemp_PF1	132.93058	4.81906	-6.68075	16.31887	No
geltemp_PF2	128.88016	8.86948	-2.63033	20.36929	No
geltemp_PF3	104.77646	32.97318	21.47337	44.473	Yes
geltemp_PF1	132.93058				
geltemp_PF2	128.88016	4.05042	-7.44939	15.55023	No
geltemp_PF3	104.77646	28.15412	16.65431	39.65394	Yes
geltemp_PF2	128.88016				
geltemp_PF3	104.77646	24.1037	12.60389	35.60352	Yes

Power Analysis

Alpha	Total Sample Size	Power
0.5	20	1.00000 (actual)

5.7.4. Statistical analysis of the $(\delta E'/\delta t)_{max}$ values

One-Way ANOVA

Summary Statistics

Dataset	N	Mean	SD	SE
curerate_PF0	5	5.62	1.22607	0.54832
curerate_PF1	5	6.336	0.85527	0.38249
curerate_PF2	5	7.494	0.42741	0.19114
curerate_PF3	5	7.352	0.34172	0.15282

Null Hypothesis: The means of all selected datasets are equal
Alternative Hypothesis: The means of one or more selected datasets are different

ANOVA

Source	DoF	Sum of Squares	Mean Square	F Value	P Value
Model	3	11.7721750	3.92405833	6.19381	0.00538
Error	16	10.1367200	0.633545000		

At the 0.05 level,
the population means are significantly different.

Means Comparison using Tukey Test

Dataset	Mean	Difference between Means	Simultaneous Confidence Intervals Lower Limit	Upper Limit	Significant at 0.05 Level
curerate_PF0	5.62				
curerate_PF1	6.336	-0.716	-2.15623	0.72423	No
curerate_PF2	7.494	-1.874	-3.31423	-0.43377	Yes
curerate_PF3	7.352	-1.732	-3.17223	-0.29177	Yes
curerate_PF1	6.336				
curerate_PF2	7.494	-1.158	-2.59823	0.28223	No
curerate_PF3	7.352	-1.016	-2.45623	0.42423	No
curerate_PF2	7.494				
curerate_PF3	7.352	0.142	-1.29823	1.58223	No

Power Analysis

Alpha	Total Sample Size	Power
0.5	20	0.99868 (actual)

5.7.5. Statistical analysis of the E'_{max} values

One-Way ANOVA

Summary Statistics

Dataset	N	Mean	SD	SE
rigidity_PF0	5	20.668	1.45049	0.64868
rigidity_PF1	5	23.968	0.84642	0.37853
rigidity_PF2	5	26.644	1.08871	0.48688
rigidity_PF3	5	24.108	1.07876	0.48244

Null Hypothesis: The means of all selected datasets are equal
Alternative Hypothesis: The means of one or more selected datasets are different

ANOVA

Source	DoF	Sum of Squares	Mean Square	F Value	P Value
Model	3	90.0600600	30.0200200	23.22929	0.00000
Error	16	20.6773600	1.29233500		

At the 0.05 level,
the population means are significantly different.

Means Comparison using Tukey Test

Dataset	Mean	Difference between Means	Simultaneous Confidence Intervals Lower Limit	Upper Limit	Significant at 0.05 Level
rigidity_PF0	20.668				
rigidity_PF1	23.968	-3.3	-5.35698	-1.24302	Yes
rigidity_PF2	26.644	-5.976	-8.03298	-3.91902	Yes
rigidity_PF3	24.108	-3.44	-5.49698	-1.38302	Yes
rigidity_PF1	23.968				
rigidity_PF2	26.644	-2.676	-4.73298	-0.61902	Yes
rigidity_PF3	24.108	-0.14	-2.19698	1.91698	No
rigidity_PF2	26.644				
rigidity_PF3	24.108	2.536	0.47902	4.59298	Yes

Power Analysis

Alpha	Total Sample Size	Power
0.5	20	1.00000 (actual)

CHAPTER 6

EFFECTS OF CELLULOSE NANOCRYSTALS ON PHENOL–FORMALDEHYDE ADHESIVE RESINS—PART IV: FRACTUTRE PERFORMANCE

6.1. ABSTRACT

The purpose of this study was to determine the effects of cellulose nanocrystals (CNCs) on the fracture performance of phenol–formaldehyde (PF) resol resins. Double cantilever beam test specimens were prepared from southern yellow pine beams and four CNC–resin mixtures, containing 0–3 wt % CNCs, using different hot-pressing times. Fracture energies were measured by mode I cleavage tests. Bondline characteristics were analyzed by light microscopy. For CNC contents of 0 and 3 wt %, a decrease in fracture energy was observed when the hot-pressing time exceeded 15 and 8 min, respectively. At hot-pressing times of 8 and 10 min, the fracture energy for CNC contents of 1, 2, and 3 wt % was lower than for 0 wt %. At a hot-pressing time of 10 min, the fracture energy decreased with increasing CNC content, whereas it stayed constant for CNC contents between 1 and 3 wt % at a hot-pressing time of 8 min. The bondlines of resin mixtures containing CNCs exhibited voids, whereas those of the pure resin did not. Under the experimental conditions examined, the CNCs were concluded to have detrimental effects on PF resin fracture performance.

6.2. INTRODUCTION

Increasing competition in the adhesives industry has been spurring efforts toward the advancement of adhesion technologies. Such efforts have primarily been aimed at reducing adhesive cost while maintaining quality and performance as well as the development of new and specialty adhesives [1]. Nanoparticles, added in small amounts (< 10%), have been shown to achieve simultaneous increases in adhesive stiffness, strength, and fracture toughness [2-5] and, therefore, have the potential to bring about significant advances in adhesive technology.

This study is part of a larger investigation of the effects of cellulose nanocrystals (CNCs) on the properties and performance of phenol–formaldehyde (PF) adhesive resins. PF resins are among the most widely used adhesives in the wood composites industry. CNCs are promising candidates as additives for PF adhesive resins based on the demonstrated catalytic effect of cellulose on PF resin cure reactions [6-8]. In prior studies (Chapters 4 and 5), we have demonstrated that, under certain conditions, CNCs accelerate PF resin cure and increase the post-cure storage modulus of PF resol resins.

The objective of this study was to determine the effects of CNCs on the fracture performance of PF resins. Assessing the performance of wood adhesive joints is challenging in that, under shear loading, the strength of the joint often exceeds that of the wood adherend, and, consequently, the load values for joint failure may depend more on the strength of the wood than on the adhesive or cohesive strength of the adhesive. The shortcomings of strength tests under shear loading for the evaluation of wood adhesive joints were recognized as early as 1965 by Stanger and Blomquist [9], who showed in a comparison of the conventional block shear test, the cross-lap tension test, and a cleavage test that the latter produced a lower percentage of wood failure and was therefore more sensitive to bondline properties. In the mid and late 1970s, cleavage testing of wood adhesive joints was further advanced by several groups through the application of linear elastic fracture mechanics [10-18]. In 1979, Ebewele *et al.* [16, 17] reported a method for the determination of fracture energy of wood adhesive joints that was based on the contoured double cantilever beam specimen geometry. More recently, Gagliano and Frazier have evaluated a method that uses the simpler double cantilever beam geometry

and the compliance method in combination with the corrected beam theory for data analysis [19-21]. The method was found to be sensitive to adhesive parameters and a simplification with respect to the method by Ebewele *et al.* [16, 17].

In the present study, we measured the fracture energies of single cantilever beam specimens from four CNC–resin mixtures, containing 0–3 wt % CNCs, following the method of Gagliano and Frazier [19-21].

6.3. EXPERIMENTAL

6.3.1. Materials

Dissolving-grade softwood sulfite pulp (Temalfa 93A-A) was kindly provided by Tembec, Inc. Liquid phenol–formaldehyde resol resin (OSB core resin, 50 wt % solids content, < 0.1 wt % free formaldehyde) was kindly provided by Dynea North America, now Arclin. The resin was stored frozen in 500 mL units until use. Prior to use, the resin was thawed and thoroughly mixed. Sulfuric acid (95.9 wt %, certified) was purchased from Fisher Scientific and used as received. Deionized water (18.2 MΩ·cm) was generated from tap water with a Millipore Direct-Q 5 Ultrapure Water System. Flat sawn southern yellow pine (*Pinus spp.*) boards were purchased from a local wood supplier.

6.3.2. Methods

6.3.2.1. Preparation of resin mixtures

Four CNC–resin mixtures with CNC contents of 0 wt % (PF0), 1 wt % (PF1), 2 wt % (PF2), and 3 wt % (PF3), based on total solids content, were prepared as described in Chapter 3. Briefly, a stable CNC suspension was prepared by hydrolysis of milled wood pulp with 64 wt % sulfuric acid for 60 min at 45.5 °C and an acid-to-pulp ratio of 10 mL/g. The suspension was concentrated to 10 wt % with a rotary evaporator (Büchi Rotavapor R-200) using a water bath temperature of 40 °C. Different amounts of the CNC suspension and deionized water were slowly added under stirring (500 rpm) to the PF resin. Stirring was continued for 10 min to ensure good mixing. The respective amounts of CNC suspension and deionized water were chosen to maintain an equal solids content of 44.64 wt % in the four resin mixtures. The pH of the resin mixtures decreased slightly with increasing CNC content from 12.30 ± 0.01 at 0 wt % to 12.27 ± 0.02 at 3 wt %. No fillers, extenders, or any other additives were added in this study.

6.3.2.2. Preparation of fracture specimens

Fracture specimens were prepared according to the method by Gagliano and Frazier [19], with minor modifications. Southern yellow pine boards were jointed, planed, and sawn into laminae of 250 × 140 × 10 mm (L × T × R) with a grain angle of 3–5° with respect to the tangential bonding surface (Figure 6.1). Prior to bonding, the laminae were conditioned at 20 °C and 65% relative humidity for a minimum of two weeks (estimated moisture content: ~10%). The bonding surfaces were hand sanded with 120 grit sandpaper and subsequently cleaned with an air gun. Approximately 50 g/m^2 of resin mixture was applied with a hard rubber roller to each bonding surface. After the two bonding surfaces were mated, the laminates were placed in a hot-press with a platen temperature of 180 °C and an initial pressure of 0.69 MPa (100 psi) and bonded for different amounts of time, ranging from 8 to 20 min. The pressure during hot-pressing was not controlled and dropped over time as a result of wood softening. The temperature at the bondline was monitored with a thermocouple inserted between the two laminae.

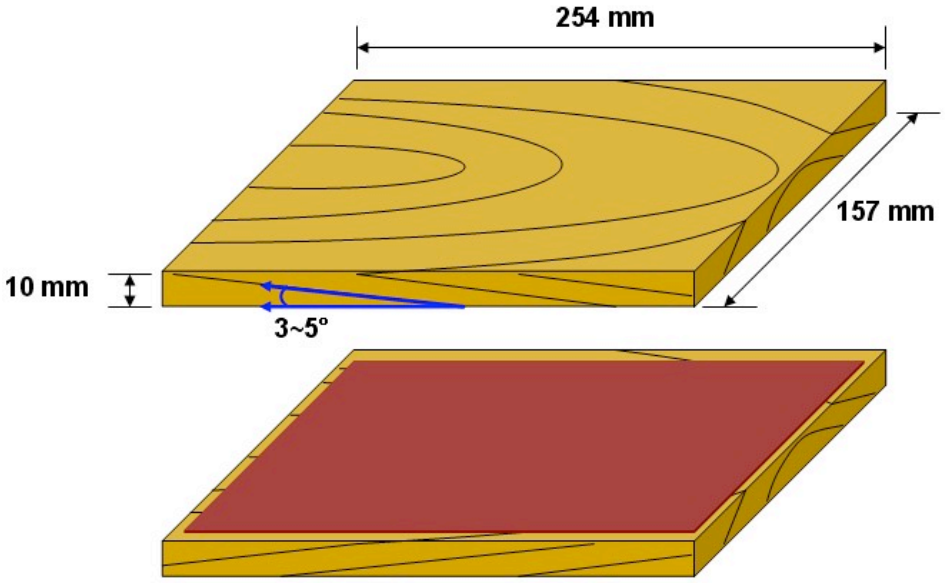

Figure 6.1. Geometry and dimensions of the flat-sawn southern yellow pine laminae and illustration of laminate assembly.

After hot-pressing and cooling to room temperature, the bonded laminates were cut into fracture specimens of 20 mm width and 220 mm length, as illustrated in Figure 6.2. Four to five specimens were obtained from each bonded laminate. At least two bonded laminates were prepared for each resin mixture for a minimum of eight fracture specimens. Prior to the test, white typographic correction fluid was painted onto the bondline and a paper ruler with millimeter divisions was glued below the bondline for easier crack length measuring (Figure 6.2). Finally, a 4.5 mm hole was drilled into each beam for attachment of the test grips.

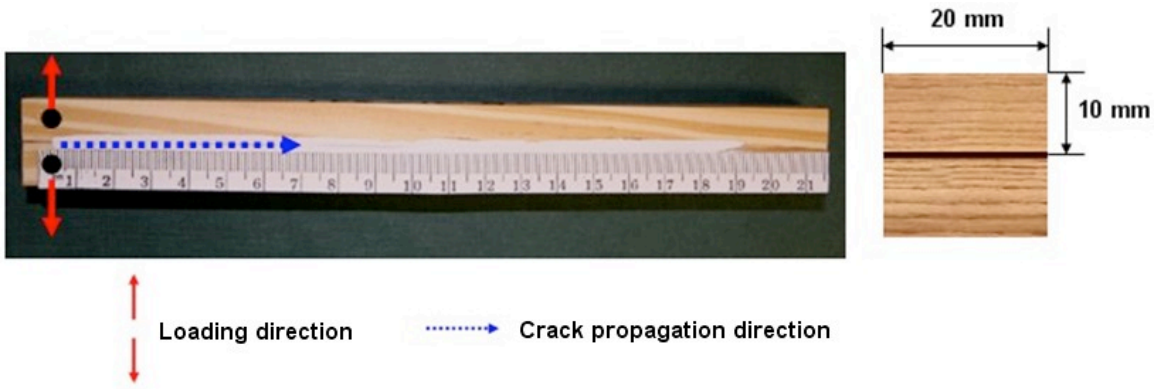

Figure 6.2. Geometry and dimensions of the DCB fracture specimens.

6.3.2.3. Mode-I fracture testing

Prior to the test, the fracture specimen was notched in the bondline using an in-house notching blade. The specimen was fixed to the grips of an MTS Sintech 10/GL screw driven load frame, controlled with TestWorks software, and the free end of the specimen was supported to maintain a horizontal specimen orientation. Prior to the measurement, a 5–10 N preload was applied and the crosshead displacement was set to zero. Then, the crosshead was displaced at a speed of 1 mm/min until the crack tip reached the 50 mm mark (initial crack length). Measurements were performed under displacement control with an initial crosshead speed of 1 mm/min. Movement of the

crosshead was halted manually as soon as crack propagation was detected. After a 45 s stationary period, the crosshead returned to the zero position and a new load cycle was initiated until catastrophic failure of the specimen occurred or until the crack length exceeded 150 mm. Before each load cycle, the crosshead speed was adjusted to the crosshead displacement value at crack propagation of the previous cycle. Crack lengths were measured manually using real-time images from a CCD camera with 10 × magnification, mounted onto a horizontal track parallel to the specimen. Specimens yielded up to 15 crack extensions within the crack length range 50–150 mm. Data recorded for crack lengths outside of this range were disregarded as they might have been subject to end effects.

6.3.2.4. Data analysis

Data analysis was performed using the compliance method in combination with the corrected beam theory [19-21]. Briefly, the cube root of the compliance was plotted against the crack length and fitted with a linear regression model, yielding a slope m and a y-intercept b. The strain energy release rates for crack initiation, G_{Ic}, and crack arrest, G_{Ia}, were calculated using the equations

$$G_{\mathrm{Ic}} = \frac{P_{\mathrm{c}}^2 \left(a_{\mathrm{i}} + x\right)^2}{B(EI)_{\mathrm{eff}}} \qquad [6.1]$$

$$G_{\mathrm{Ia}} = \frac{P_{\mathrm{a}}^2 \left(a_{\mathrm{a}} + x\right)^2}{B(EI)_{\mathrm{eff}}} \qquad [6.2]$$

where P_{c} and a_{i} are the load and crack length at crack initiation, respectively, P_{a} and a_{a} are the load and crack length at crack arrest, respectively, B is the specimen width, $(EI)_{\mathrm{eff}}$ is the effective flexural stiffness of the specimen, and x is a correction factor accounting for rotation of the loaded cantilever beams at the crack tip. x and $(EI)_{\mathrm{eff}}$ are obtained from m and b as $x = b/m$ and $(EI)_{\mathrm{eff}} = 2/(3\mathrm{m}^3)$, respectively.

6.3.2.5. Light microscopy

The intact ends of tested fracture specimens that did not exhibit catastrophic failure were cut into blocks of approximately 20 × 20 × 10 mm (L × T × R) and vacuum soaked in deionized water for approximately 30 min. Sections of approximately 50 μm thickness were microtomed off the transverse (cross-sectional) surface of the saturated blocks using a sliding microtome (Model 860, American Optical Company). The microtomed sections were placed on regular microscopy glass slides, wetted with one or two drops of deionized water, and covered with a cover glass. Light microscopy images were recorded with a Canon EOS 20D digital single-lens reflex camera (8.2 megapixels) mounted onto a Zeiss Axioskop 40 A POL microscope.

6.4. RESULTS AND DISCUSSION

Figure 6.3 shows the changes in temperature at the bondline in the PF0 laminate during hot-pressing with a platen temperature of 180 °C (± 5 °C). Initially, the bondline temperature increased linearly at a rate of approximately 16 °C/min until it reached about 100 °C. Above 100 °C, the bondline temperature continued to increase linearly but at a much reduced rate (~2.5 °C/min). The decrease in the rate of temperature increase was most likely due to the evaporation of water from the system. At a hot-pressing time of 20 min, the bondline temperature was 148 °C. According to prior thermal degradation studies by thermogravimetric analysis, reported in Chapter 3, the CNCs added to the PF resin start to degrade at around 150 °C. Therefore, 20 min was the maximum hot-pressing time investigated. The bondline temperature profiles during hot-pressing for PF1, PF2, and PF3 were statistically equivalent (t-test, $\alpha = 0.05$) to that for PF0.

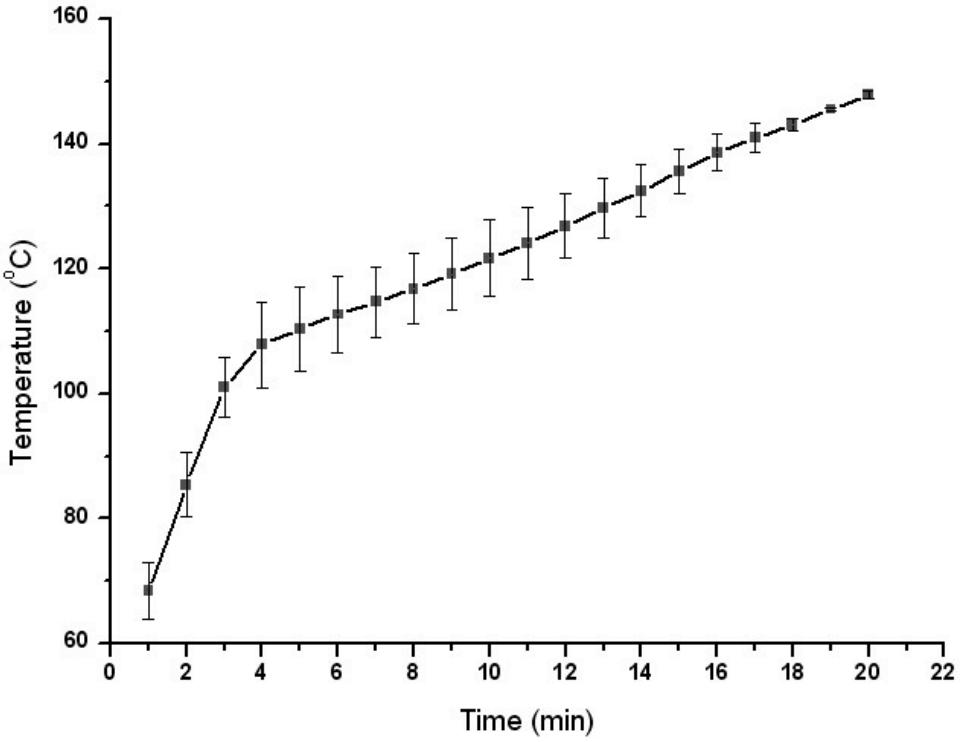

Figure 6.3. Temperature at the bondline in the PF0 laminate during hot-pressing at 180 °C (± 5 °C) as a function of time. Error bars represent ± one standard deviation.

Four different hot-pressing times were investigated: 8, 10, 15, and 20 min. With hot-pressing times of 15 and 20 min, however, the PF1, PF2, and PF3 laminates debonded either immediately after hot-pressing or during cutting of the fracture specimens. Furthermore, several PF1, PF2, and PF3 fracture specimens prepared with an 8 or 10 min hot-pressing time exhibited partial debonding before the fracture test. Thus, only a fraction of the prepared laminates and specimens could be used. Furthermore, a few fracture tests yielded fewer than three load cycles, due to premature catastrophic failure of the specimen, or excessively low (< 0.980) coefficients of determination (R^2-values) for the linear fit of the compliance data. The data from these fracture tests were disregarded. Table 6.1 shows the fraction of valid fracture tests and the number of data points obtained for each hot-pressing time–resin mixture combination.

Table 6.1. Fraction of valid fracture tests and number of data points obtained for each hot-pressing time–resin mixture combination

Pressing time	Resin mixture	Fraction of valid fracture tests[1]	Number of data points
8 min	PF0	8/8[2]	84
	PF1	3/8	18
	PF2	4/8	33
	PF3	3/8	35
10 min	PF0	8/10	86
	PF1	8/9	57
	PF2	5/10	37
	PF3	3/8	19
15 min	PF0	9/9	106
	PF1	0	0
	PF2	0	0
	PF3	0	0
20 min	PF0	6/6	61
	PF1	0	0
	PF2	0	0
	PF3	0	0

[1] Specimens or tests were excluded for any of the following reasons: (1) specimen debonded during preparation, (2) specimen did not sustain a minimum of 3 load cycles, (3) measurement's R^2-value was below 0.980

[2] Number of valid fracture tests/number of fracture specimens produced

Representative load–displacement curves for PF0 and PF3 fracture specimens are shown in Figure 6.4. For PF0 fracture specimens, the difference between critical and arrest load was fairly constant from cycle to cycle and the critical load values decreased relatively uniformly throughout the test. For PF3 fracture specimens, on the other hand, the difference between critical and arrest load and the step size for the critical load decrease varied greatly between cycles. The difference between critical and arrest load is related to crack growth. Thus, crack growth was uniform or predictable in PF0 fracture specimens and variable or unpredictable in PF3 fracture specimens. Furthermore, most PF1, PF2, and PF3 specimens failed catastrophically during the test whereas PF0 fracture specimens did not. As a consequence of the unpredictable crack growth and catastrophic failure of the specimens, PF1, PF2, and PF3 specimens sustained fewer load cycles and yielded fewer fracture energy values than PF0 fracture specimens.

Figure 6.5 shows plots of the cube root of compliance and the critical and arrest strain energy release rates versus crack length for the data from Figure 6.4. (The plots for the other valid fracture tests are shown in Appendix 6.6.1). For most fracture tests, the coefficient of determination of the linear fit of the compliance data exceeded 0.980. The fracture tests that yielded R^2-values below 0.980 were considered invalid and the data was disregarded. Most fracture tests yielded fracture energies for both crack initiation and arrest that were independent of crack length.

Figure 6.6 is a box plot of the critical strain energy release rates for the four resin mixtures and hot-pressing times. A box plot was chosen instead of a bar graph for the presentation of the data because statistical analysis of the data using the Shapiro–Wilk and Kolmogorov–Smirnov tests revealed a non-normal distribution for some of the data sets. The numerical summaries for both the critical and arrest strain energy release rate data are given in Table 6.2. A non-normal data distribution with respect to G_{Ic} was observed for PF0, PF2, and PF3 at a hot-pressing time of 8 min, and for PF1, PF2, and PF3 at a hot-pressing time of 10 min. With respect to G_{Ia}, a non-normal data distribution was observed for PF0 and PF2 at a hot-pressing time of 8 min, and for PF1 and PF2 at a hot-pressing time of 10 min. The data distribution for PF2 at a hot-pressing time of 10 min was bimodal.

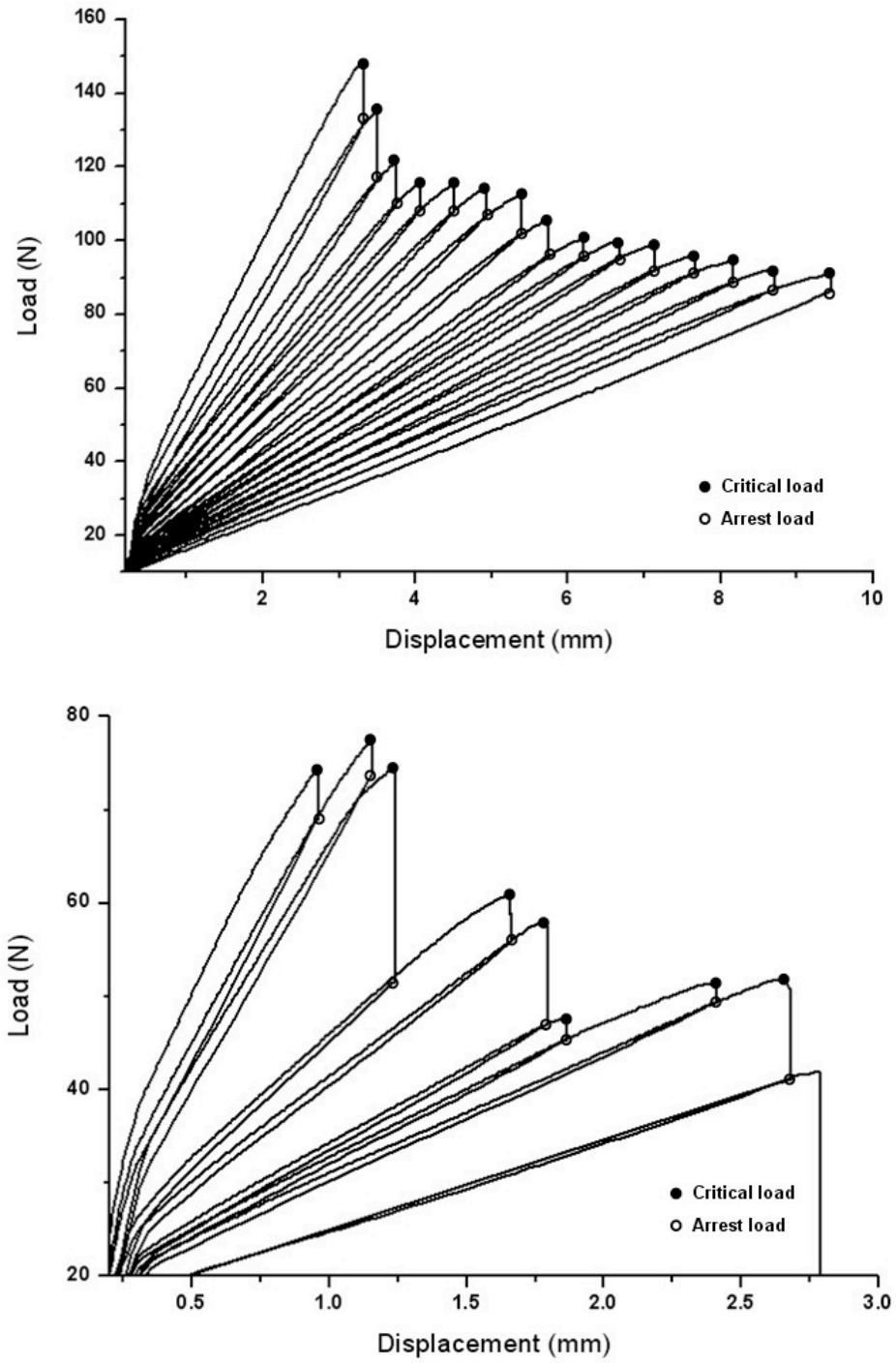

Figure 6.4. Representative load vs. displacement curves for a PF0 fracture specimen (top) and a PF3 fracture specimen (bottom).

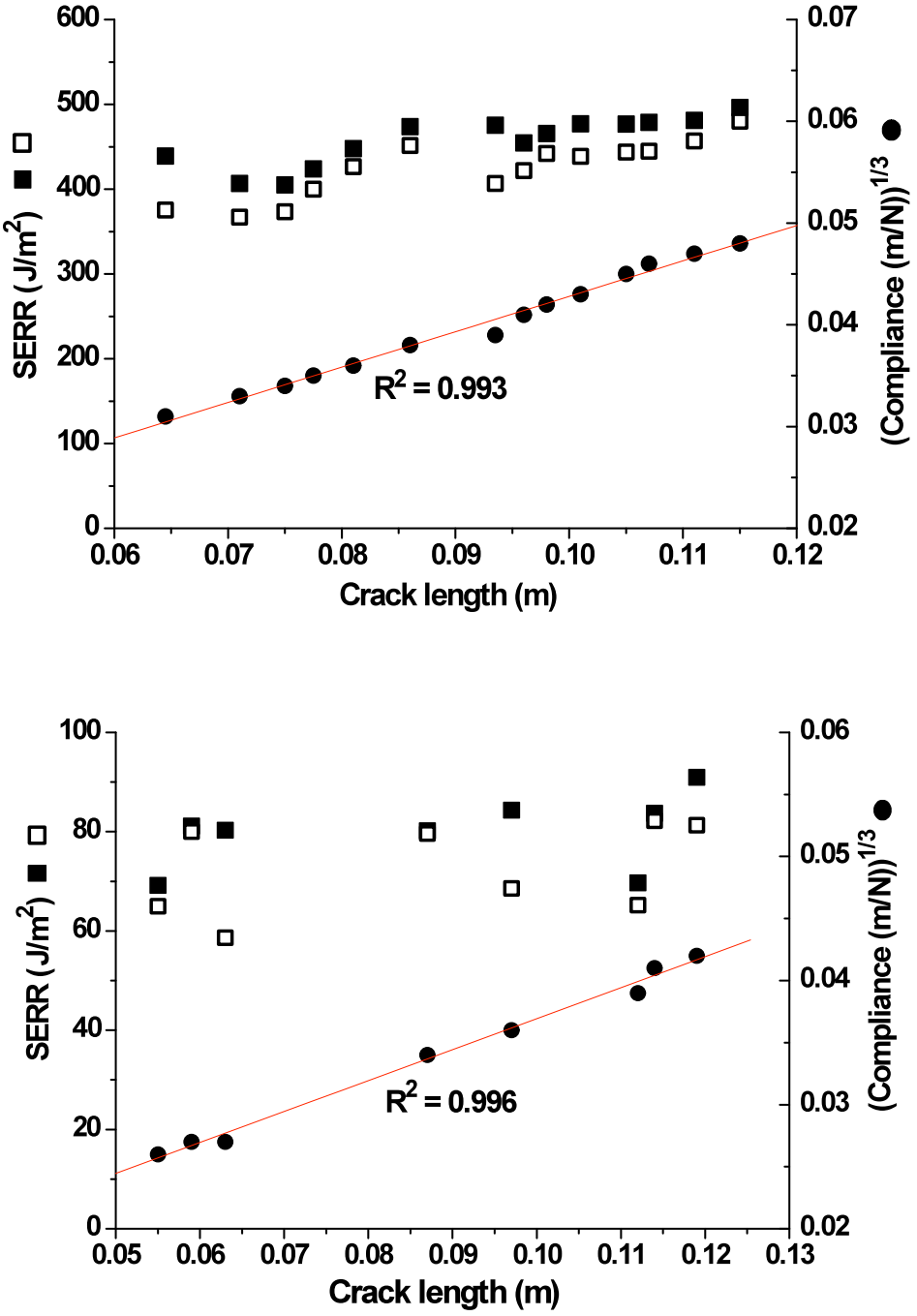

Figure 6.5. Plots of the cube root of compliance (●) and the critical (G_{Ic} ■) and arrest (G_{Ia} □) strain energy release rate versus crack length for the data from Figure 6.4 for a PF0 fracture specimen (top) and PF3 fracture specimen (bottom). The R^2-values are for the linear fit of the compliance data.

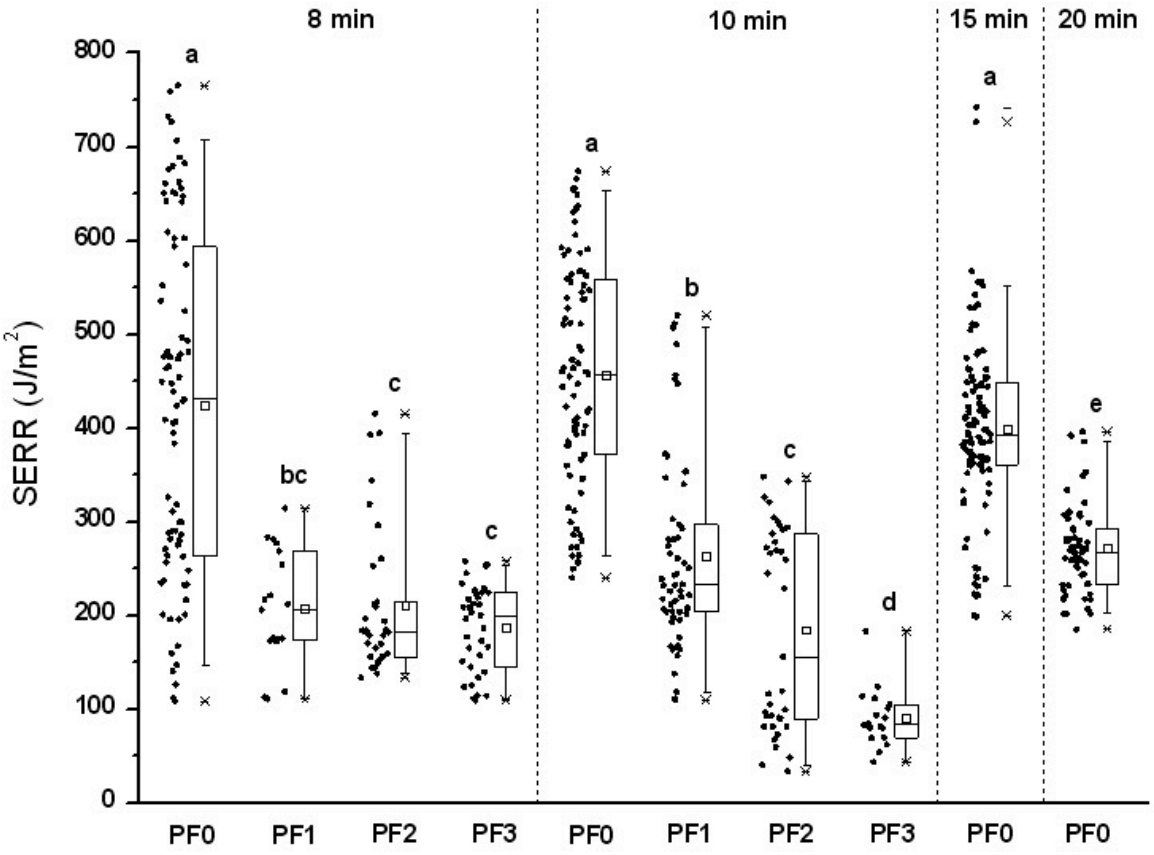

Figure 6.6. Box plot of the critical strain energy release rates (G_{Ic}) for the four resin mixtures and hot-pressing times. The square inside the box represents the mean of the data set. The individual data points are shown for illustration of distributional differences. Data sets connected by the same letter may represent the same population (Mann-Whitney U test, $p \geq 0.05$).

For PF1, PF2, and PF3, the deviation from normality of the distribution of the data could be a result of the heterogeneity of the resin mixture, discussed in Chapter 3. The reason for the deviation of the distribution for PF0 at a hot-pressing time of 8 min is not clear. The G_{Ic} data sets for the four resin mixtures and hot-pressing times were compared pair-wise using the non-parametric Mann–Whitney U test. The results of the significance test are expressed in Figure 6.6 as lowercase letters. Data sets connected by the same letter may represent the same population ($p \geq 0.05$). (The p-values for the different group comparisons are listed in Table 6.4 in Appendix 6.6.2.)

Table 6.2. Numerical summaries for the measured critical (G_{Ic}) and arrest (G_{Ia}) strain energy release rate data

	8 min				10 min				15 min	20 min
	PF0	PF1	PF2	PF3	PF0	PF1	PF2	PF3	PF0	PF0
G_{Ic}										
Distribution[1]	–	+	–	–	+	–	–	–	+	+
Mean (J/m^2)	425	208	211	187	457	264	185	90	398	271
STDEV	184	62	79	46	121	103	107	31	96	49
Median (J/m^2)	435	209	183	200	459	233	156	84	393	267
Interquartile range (J/m^2)	334	98	217	80	261	97	204	36	202	62
1st Quartile (J/m^2)	266	173	156	145	371	203	86	70	248	234
3rd Quartile (J/m^2)	600	271	373	225	631	300	289	105	449	296
G_{Ia}										
Distribution[1]	–	+	–	+	+	–	–	+	+	+
Mean (J/m^2)	392	186	184	176	423	232	170	74	368	248
STDEV	171	72	66	44	117	102	106	22	85	43
Median (J/m^2)	396	183	166	186	425	206	116	80	370	249
Interquartile range (J/m^2)	306	89	51	64	171	111	203	34	86	77
1st Quartile (J/m^2)	250	149	142	142	342	161	73	59	333	222
3rd Quartile (J/m^2)	555	238	193	206	513	273	277	92	419	299

[1] "+" indicates a normal distribution, "–" indicates a non-normal distribution

The fracture energy for crack initiation of PF0 was not significantly affected by the hot-pressing time up to a hot-pressing time of 15 min. The mean fracture energy ranged from approximately 400 to 460 J/m^2. At a hot-pressing time of 20 min, the fracture energy of PF0 was significantly decreased (mean of 271 J/m^2). A decrease in G_{Ic} with longer cure times has previously been observed by others. Mijovic and Koutsky [22] observed the phenomenon for post-cured wood–epoxy joints and attributed it to an increase in crosslink density and embrittlement of the adhesive. Ebewele *et al.* [23] attributed the observed decrease for wood–phenol/resorcinol resin joints to the decomposition of methylene ether bridges into less flexible methylene bridges or scission products. River *et al.* [24] studied wood–urea/formaldehyde resin joints and attributed the observed decrease in fracture energy with longer setting times to an increase in the degree of crosslinking at constant molecular weight and the related decrease in the difference

between the tensile strength and yield stress of the resin. The authors further pointed out that crosslinking causes shrinkage and internal stresses in the adhesive layer, which may lower its fracture energy. Any of these processes, or a combination thereof, may be responsible for the observed decrease in the fracture energy of PF0.

The obtained value of 271 J/m^2 was much lower than that measured by Zheng *et al.* [25] of approximately 430 J/m^2 for apparently the same resin. The higher fracture energy measured by Zheng *et al.* is even more surprising when considering the 20 °C higher platen temperature used, which should result in a more advanced cure state and therefore a lower fracture energy, as per the discussion above. The difference may be due to differences in resin composition and/or experimental conditions. Specifically, Zhen *et al.* used yellow poplar (*Liriodendron tulipifera*) wood and prepared the wood surface by planing whereas we used southern yellow pine (*Pinus* spp.) wood and hand sanding. Compact tension tests of wood–polyvinylacetate joints have shown that yellow poplar gives a higher fracture toughness than southern yellow pine [18]. Furthermore, surface preparation by planing has been shown to result in higher fracture toughness values than surface preparation by sanding [13, 15].

The fracture energies of the resin mixtures containing CNCs were significantly lower than the fracture energy of PF0 at both hot-pressing times investigated (8 min and 10 min). At a hot-pressing time of 8 min, a significant difference between PF1, PF2, and PF3 was not observed. At a hot-pressing time of 10 min, on the other hand, the fracture energy decreased with increasing CNC content. The fracture energy of PF1 at a hot-pressing time of 8 min did not differ significantly from that at 10 min. The same was true for PF2. The fracture energy of PF3, on the other hand, was significantly lower at a hot-pressing time of 10 min than at 8 min.

The fracture properties of an adhesive joint are governed by the bulk properties of the adherend and adhesive and by the properties of the interphase. Assuming that any variations in the wood properties are averaged out, the observed differences in the fracture energies must arise from differences in the properties of the resin or the wood–resin interphase. We will first consider the bulk properties of the resin.

If fracture occurred in the resin and not at the wood–resin interface, a lower fracture energy would indicate a more brittle and less ductile state of the resin. A brittle system offers less resistance to crack propagation than a ductile system. Consequently, for the same initiation fracture energy, G_{Ic}, a brittle system exhibits a lower arrest fracture energy, G_{Ia}, than a ductile system. Thus, the difference between the initiation and arrest fracture energies, $G_{Ic} - G_{Ia} = \Delta G_I$, is a measure for the brittleness of the system [17]. The relative difference, $\Delta G_I / G_{Ic}$, i.e. the difference normalized to the same strain (potential) energy, stored in the system, has been termed the brittleness index I [26]. Table 6.3 lists the brittleness index values for the four resin mixtures and hot-pressing times calculated using both the fracture energy means and medians.

Table 6.3. Brittleness indices, I, for the four resin mixtures and hot-pressing times calculated using the fracture energy means and medians

	8 min				10 min				15 min	20 min
	PF0	PF1	PF2	PF3	PF0	PF1	PF2	PF3	PF0	PF0
I using means (%)	8	11	13	6	7	12	8	18	8	9
I using medians (%)	9	12	9	7	7	11	26	5	6	7

An increase in brittleness index with increasing hot-pressing time or CNC content was not apparent. PF3 exhibited a higher mean-derived brittleness index at a hot-pressing time of 10 min than at a hot-pressing time of 8 min. However, the trend was not observed and perhaps even reversed for the median-derived brittleness index. Similarly, PF2 exhibited a much higher median-derived brittleness index at a hot-pressing time of 10 min than at a hot-pressing time of 8 min, but the trend was reversed for the mean-derived brittleness index. Thus, the brittleness index did not provide an explanation for the observed differences in fracture energies at different hot-pressing times or CNC contents.

Nevertheless, for the decrease in fracture energy of PF0 and PF3 with increasing hot-pressing time, embrittlement of the resin is still a more probable explanation than weakening of the interphase. The interphase is formed through penetration of the resin

into the wood, which occurs during the initial stages of bonding when the resin is still liquid. Thus, the properties of the interphase should not be much affected by hot-pressing time after the resin has solidified. The fact that the brittleness index did not indicate a higher brittleness for PF0 at a hot-pressing time of 20 min and for PF3 at a hot-pressing time of 10 min than at 8 min led us to question the sensitivity of the brittleness index.

Regarding the decrease in fracture energy with increasing CNC content, embrittlement of the resin and weakening of the interphase are equally possible reasons. In Chapters 4 and 5, we have shown that CNCs accelerate resin cure and hardening, and may cause an earlier onset of vitrification. Thus, the lower fracture energies of the resins containing CNCs might have been due to a higher degree of resin vitrification. To detect potential effects of the CNCs on the wood–resin interphase, we inspected the bondlines of tested fracture specimens with a light microscope. Figure 6.7 shows typical bondline images for the four resin mixtures. The images were obtained from microtomed sections of the intact ends of the specimens. The bondlines of PF1, PF2, and PF3 fracture specimens exhibited voids, whereas no voids were observed in the bondline of PF0 fracture specimens. Furthermore, resin penetration appeared to be less deep and less symmetric in the fracture specimens bonded by the CNC containing resins. In Chapter 3, we have shown that addition of CNCs changes the flow behavior of the resin from Newtonian to shear-thinning and causes a strong increase in resin viscosity at low shear rates. The viscosity at low shear rate has a strong influence on the spreading of liquids on solid surfaces [27-29] and the penetration of liquids into porous substrates, such as wood [30-32]. A higher low-shear viscosity results in lower rates of spreading and penetration. Furthermore, air bubbles trapped between the liquid and the substrate rise more slowly to the surface in a spread liquid of high viscosity than in a liquid of low viscosity. Thus, through their effect on resin viscosity, CNCs might have promoted the formation of a mechanical weak boundary layer, as defined by Stehr and Johansson [33]. The voids might have been caused by entrapped air bubbles or incomplete spreading of the resin mixture on the wood surface, leaving some areas devoid of resin.

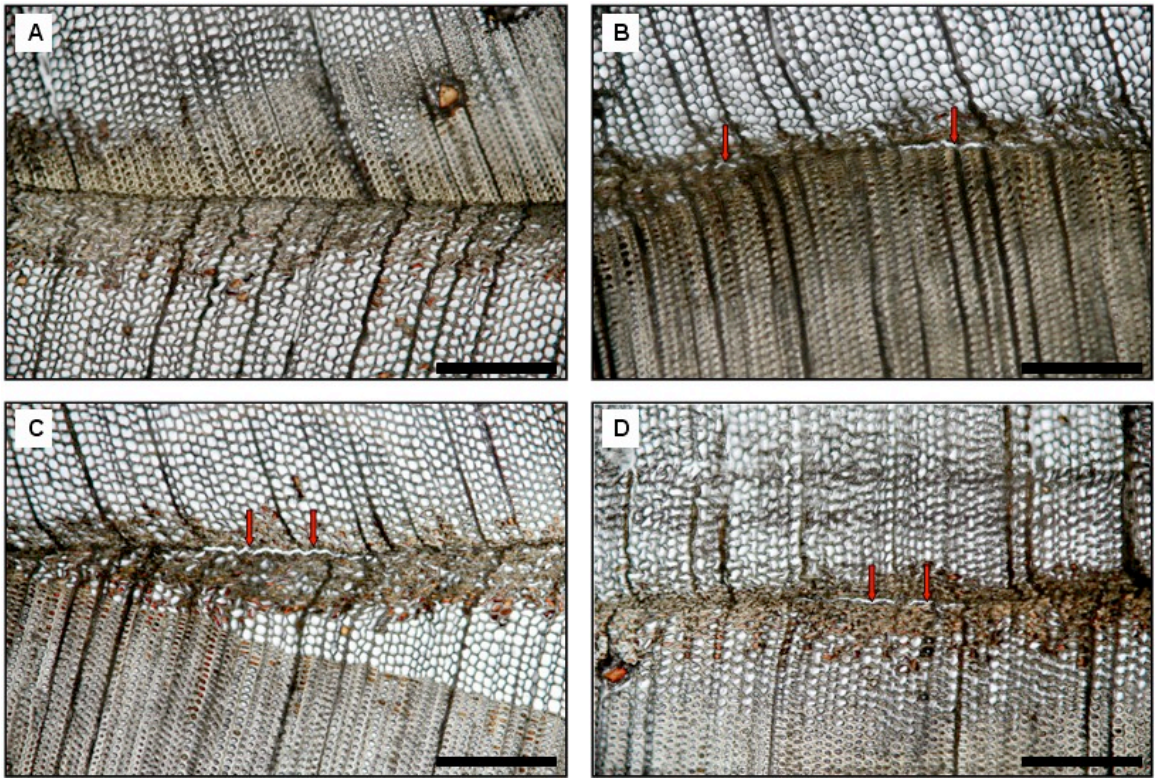

Figure 6.7. Bondline images (transverse surface) for the four resin mixtures: (a) PF0, (b) PF1, (c) PF2, (d) PF3. Arrows indicate voids in the bondline. (Scale bar: 0.5 mm)

Furthermore, we have shown in Chapter 3 that the CNC-containing resin mixtures were non-homogeneous in nature and contained loose CNC aggregates. These aggregates might have been broken up by shear forces during application of the resin with the roller. It is possible, however, that regions of high CNC density still existed in the resin after laminate assembly. Those regions would be deficient in resin and could therefore also be responsible for voids in the bondline. Whatever the reason, the bondline images, shown in Figure 6.7, provided clear evidence for a detrimental effect of the CNCs on the wood–resin interphase, which was likely the cause for the reduced fracture performance of the CNC-containing resin mixtures. Additionally, a detrimental effect of the CNCs on resin brittleness through vitrification point depression and restriction of molecular motions of the resin molecules might have played a role but could not be proven.

6.5. CONCLUSIONS

With respect to the objective of this study, our conclusions are:

- CNCs diminish the fracture energy of PF resins;
- At short hot-pressing times, the effect is independent of CNC content;
- At longer hot-pressing times, higher CNC contents cause greater fracture energy reductions;
- CNCs cause voids in the bondline;
- The detrimental effect of CNCs on the fracture energy may be due to an acceleration of resin cure and depression of the vitrification point by the CNCs;
- The detrimental effect of CNCs on bondline quality may be due to the increasing effect of CNCs on resin viscosity.
- Effects different from the ones observed here may be observed if the resin mixtures are subjected to a homogenization treatment for better dispersion of the CNCs.

6.6. REFERENCES

[1] Dunky, M. Adhesives in the Wood Industry. In: Handbook of Adhesives Technology; 2nd ed.; Pizzi, A., Mittal, K. L., Eds.; Marcel Dekker: New York, 2003; pp 887-956.

[2] Wetzel, B.; Rosso, P.; Haupert, F.; Friedrich, K. Epoxy nanocomposites - fracture and toughening mechanisms. Les Diablerets, SWITZERLAND, Sep 11-14, 2005; pp 2375-2398.

[3] Dodiuk, H.; Kenig, S.; Blinsky, I.; Dotan, A.; Buchman, A. Nanotailoring of epoxy adhesives by polyhedral- oligomeric-sil-sesquioxane (POSS). International Journal of Adhesion and Adhesives 2005, 25, 211-218.

[4] Johnsen, B. B.; Kinloch, A. J.; Mohammed, R. D.; Taylor, A. C.; Sprenger, S. Toughening mechanisms of nanoparticle-modified epoxy polymers. Polymer 2007, 48, 530-541.

[5] Buchman, A.; Dodiuk-Kenig, H.; Dotan, A.; Tenne, R.; Kenig, S. Toughening of Epoxy Adhesives by Nanoparticles. Journal of Adhesion Science and Technology 2009, 23, 753-768.

[6] Chow, S. Z. Kinetic study of the polymerization of phenol-formaldehyde resin in the presence of cellulosic materials. Wood Science 1969, 1, 215-221.

[7] Pizzi, A. Catalytic activation of wood adhesive polycondensation by the adhesion forces to a cellulosic substrate. International Congress on Adhesion Science and Technology, Invited Papers, Festschrift in Honor of Dr. K. L. Mittal on the Occasion of his 50th Birthday, 1st, Amsterdam, Oct. 16-20, 1995 1998, 531-542.

[8] Pizzi, A.; Mtsweni, B.; Parsons, W. Wood-induced catalytic activation of PF adhesives autopolymerization vs PF wood covalent bonding. Journal of Applied Polymer Science 1994, 52, 1847-1856.

[9] Stanger, A. G.; Blomquist, R. F. Block shear, cross-lap tension, and glueline cleavage methods of testing glued joints. Forest Products Journal 1965, 15, 468-474.

[10] Komatsu, K.; Sasaki, H.; Maku, T. Evaluation of Fracture Toughness for Wood-Epoxy Adhesive System under External Shear Force. Wood Research: Bulletin of the Wood Research Institute, Kyoto University 1974, 57, 10-22.

[11] Komatsu, K.; Sasaki, H.; Maku, T. Strain Energy Release Rate of Double Cantilever Beam Specimen with Finite Thickness of Adhesive Layer. Wood Research: Bulletin of the Wood Research Institute, Kyoto University 1976, 59/60, 80-92.

[12] Komatsu, K.; Sasaki, H.; Maku, T. Estimating Fracture Toughness from Nonlinear Load-Deflection Relation. Wood Research: Bulletin of the Wood Research Institute, Kyoto University 1976, 61, 25-43.

[13] White, M. S. Influence of resin penetration on the fracture toughness of wood-adhesive bonds. Ph.D. dissertation, Virginia Polytechnic Institute and State University, Blacksburg, VA, 1975.

[14] White, M. S. Influence of resin penetration on the fracture toughness of wood adhesive bonds. Wood Science 1977, 10, 6-14.

[15] White, M. S.; Green, D. W. Effect of Substrate on the Fracture-Toughness of Wood-Adhesive Bonds. Wood Science 1980, 12, 149-153.

[16] Ebewele, R.; River, B.; Koutsky, J. Tapered Double Cantilever Beam Fracture Tests of Phenolic-Wood Adhesive Joints. Part I. Development of Specimen Geometry; Effects of Bondline Thickness, Wood Anisotropy and Cure Time on Fracture Energy. Wood and Fiber 1979, 11, 197-213.

[17] Ebewele, R. O.; River, B. H.; Koutsky, J. A. Tapered Double Cantilever Beam Fracture Tests of Phenolic-Wood Adhesive Joints. Part II. Effects of Surface Roughness, the Nature of Surface Roughness, and Surface Aging on Joint Fracture Energy. Wood and Fiber 1980, 12, 40-65.

[18] Ruedy, T. C. The effect of grain angle orientation on the fracture toughness of wood-adhesive systems. M.S. thesis, Virginia Polytechnic Institute and State University, Blacksburg, VA, 1977.

[19] Gagliano, J. M.; Frazier, C. E. Improvements in the fracture cleavage testing of adhesively-bonded wood. Wood and Fiber Science 2001, 33, 377-385.

[20] Conrad, M. P. C.; Smith, G. D.; Fernlund, G. Fracture of discontinuous wood-adhesive bonds. International Journal of Adhesion and Adhesives 2003, 23, 39-47.

[21] Blackman, B. R. K.; Kinloch, A. J. Protocol for the determination of the Mode I adhesive fracture energy, GIc, of structural adhesives using the double cantilever beam (DCB) and tapered double cantilever beam (TDCB) specimens. In: Fracture mechanics testing methods for polymers, adhesives and composites; Pavan, A., Moore, D. R., G., W. J., Eds.; Elsevier: Amsterdam, 2001.

[22] Mijovic, J. S.; Koutsky, J. A. Effect of Wood Grain Angle on Fracture Properties and Fracture Morphology of Wood-Epoxy Joints. Wood Science 1979, 11, 164-168.

[23] Ebewele, R. O.; River, B. H.; Koutsky, J. A. Relationship between Phenolic Adhesive Chemistry, Cure and Joint Performance. Part I. Effects of Base Resin Constitution and Hardener on Fracture Energy and Thermal Effects During Cure. Journal of Adhesion 1982, 14, 189-217.

[24] River, B. H.; Scott, C. T.; Koutsky, J. A. Adhesive joint fracture behaviour during setting and aging. Forest Products Journal 1989, 39, 23-28.

[25] Zheng, J.; Fox, S. C.; Frazier, C. E. Rheological, wood penetration, and fracture performance studies of PF/pMDI hybrid resins. Forest Products Journal 2004, 54, 74-81.

[26] Ebewele, R. O.; River, B. H.; Koutsky, J. A. Relationship between Phenolic Adhesive Chemistry and Adhesive Joint Performance: Effect of Filler Type on Fraction Energy. Journal of Applied Polymer Science 1986, 31, 2275-2302.

[27] Lopez, J.; Miller, C. A.; Ruckenstein, E. Spreading Kinetics of Liquid Drops on Solids. Journal of Colloid and Interface Science 1976, 56, 460-468.

[28] Sauer, B. B.; Kampert, W. C. Influence of viscosity on forced and spontaneous spreading: Wilhelmy fiber studies including practical methods for rapid viscosity measurement. Journal of Colloid and Interface Science 1998, 199, 28-37.

[29] Bonn, D.; Eggers, J.; Indekeu, J.; Meunier, J.; Rolley, E. Wetting and spreading. Reviews of Modern Physics 2009, 81, 739-805.

[30] Scheikl, M.; Dunky, M. Measurement of dynamic and static contact angles on wood for the determination of its surface tension and the penetration of liquids into the wood surface. Holzforschung 1998, 52, 89-94.

[31] de Meijer, M.; Thurich, K.; Militz, H. Quantitative measurements of capillary coating penetration in relation to wood and coating properties. Holz Als Roh-Und Werkstoff 2001, 59, 35-45.

[32] Kamke, F. A.; Lee, J. N. Adhesive penetration in wood - A review. Wood and Fiber Science 2007, 39, 205-220.

[33] Stehr, M.; Johansson, I. Weak boundary layers on wood surfaces. Journal of Adhesion Science and Technology 2000, 14, 1211-1224.

6.7. APPENDIX

6.7.1. SERR and cube root of the compliance plots for all valid fracture tests

Crack length dependencies of the cube root of the compliance (●) and critical SERR (G_{Ic} ■) and arrest SERR (G_{Ia} □) for all fracture specimen. The R^2 values are for the linear fit of the compliance data.

6.7.1.1. PF0 – 8 min

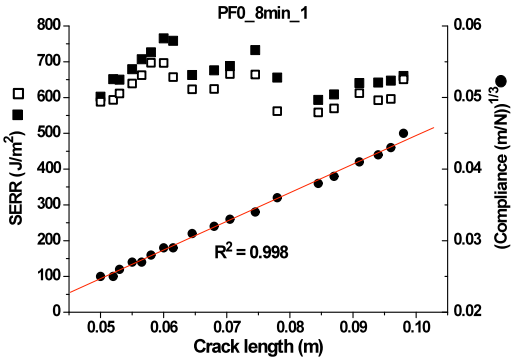

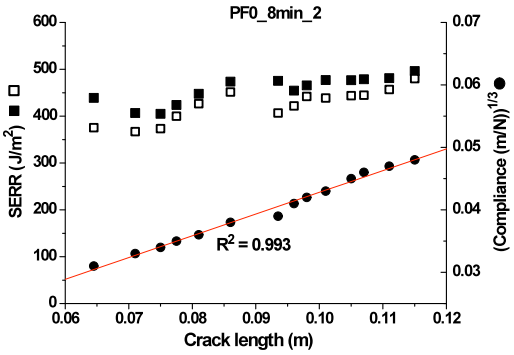

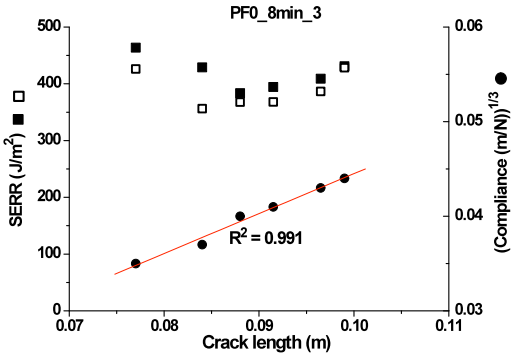

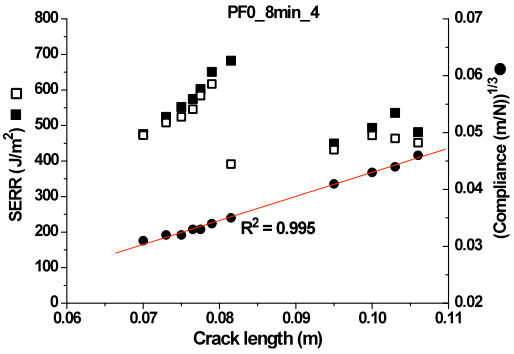

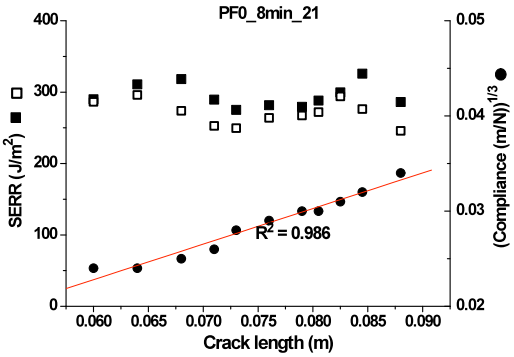

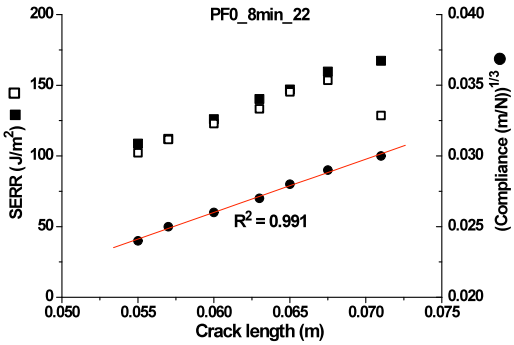

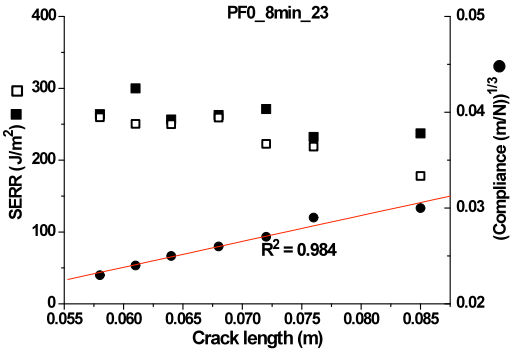

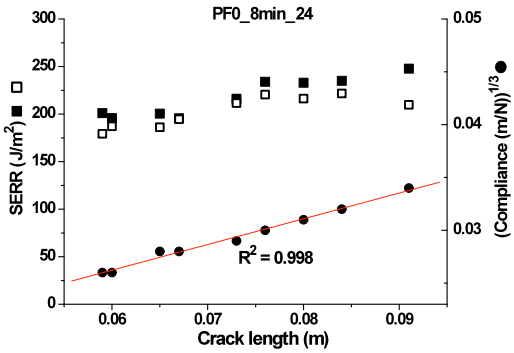

6.7.1.2. PF0 – 10 min

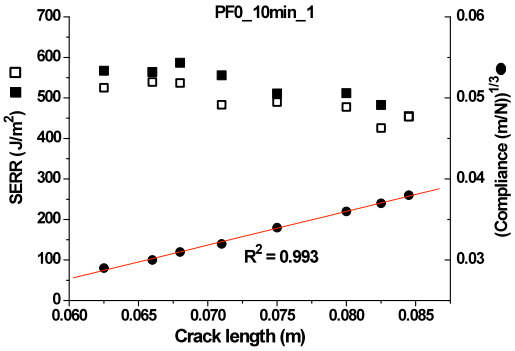

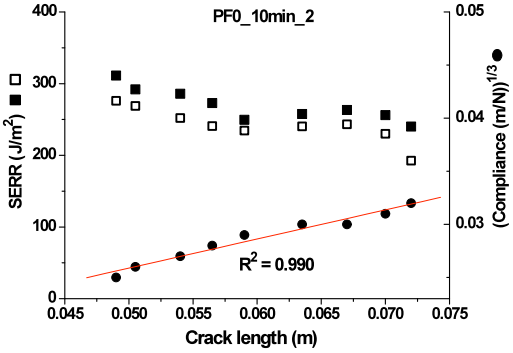

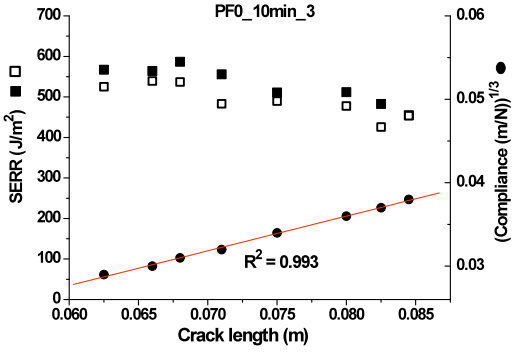

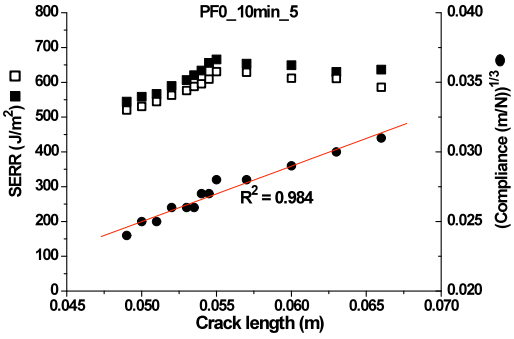

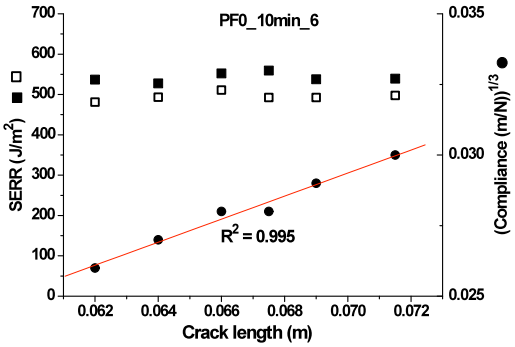

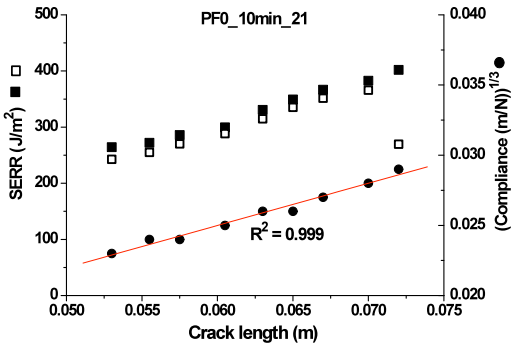

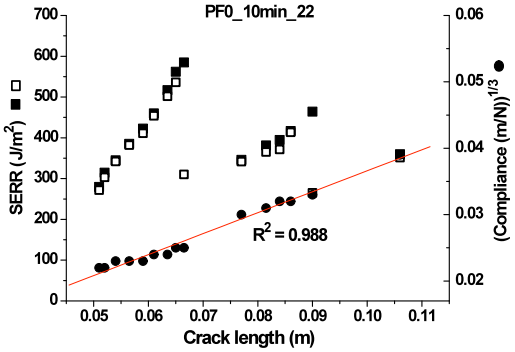

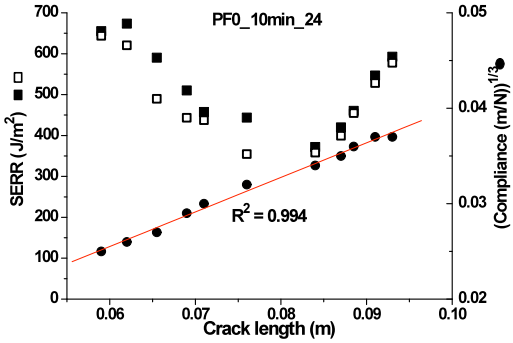

6.7.1.3. PF0 – 15 min

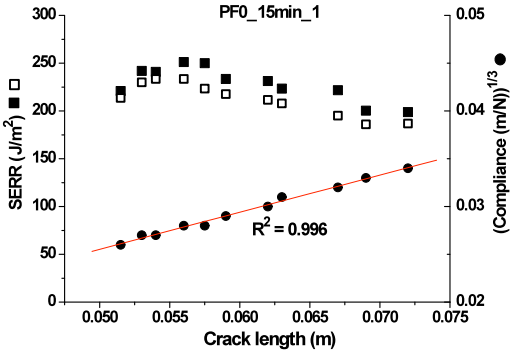

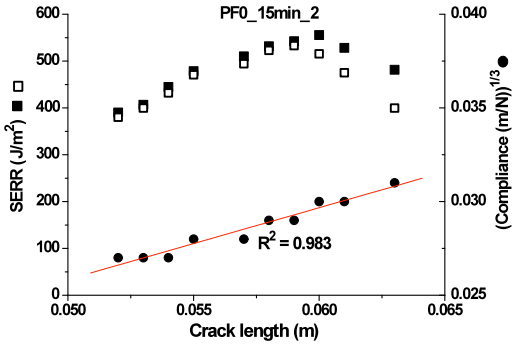

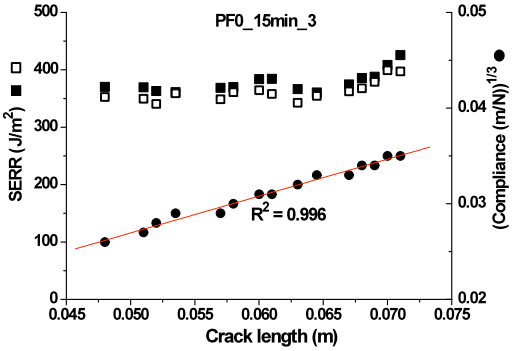
PF0_15min_3
SERR (J/m²)
(Compliance (m/N))^1/3
Crack length (m)
R² = 0.996

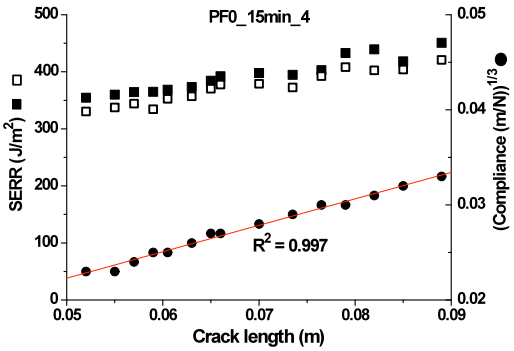
PF0_15min_4
SERR (J/m²)
(Compliance (m/N))^1/3
Crack length (m)
R² = 0.997

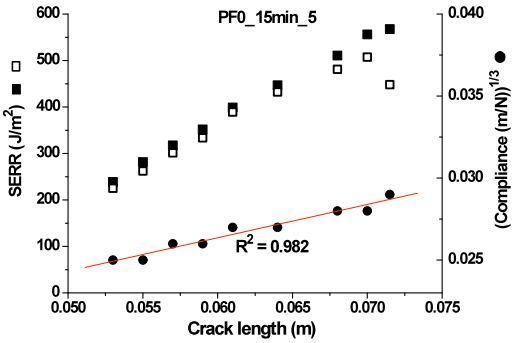
PF0_15min_5
SERR (J/m²)
(Compliance (m/N))^1/3
Crack length (m)
R² = 0.982

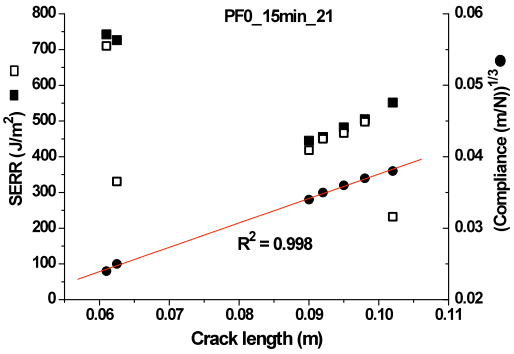
PF0_15min_21
SERR (J/m²)
(Compliance (m/N))^1/3
Crack length (m)
R² = 0.998

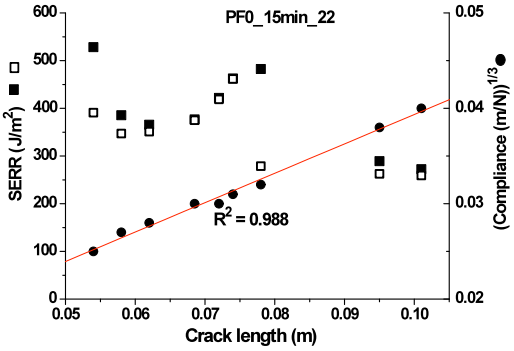
PF0_15min_22
SERR (J/m²)
(Compliance (m/N))^1/3
Crack length (m)
R² = 0.988

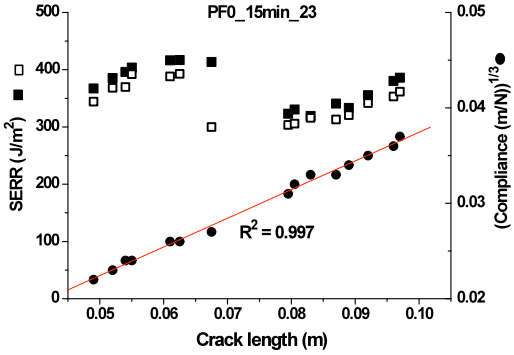
PF0_15min_23
SERR (J/m²)
(Compliance (m/N))^1/3
Crack length (m)
R² = 0.997

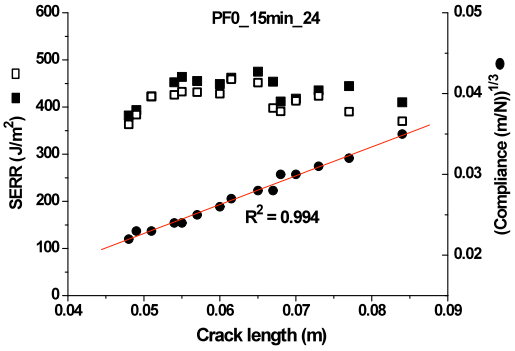
PF0_15min_24
SERR (J/m²)
(Compliance (m/N))^1/3
Crack length (m)
R² = 0.994

6.7.1.4. PF0 – 20 min

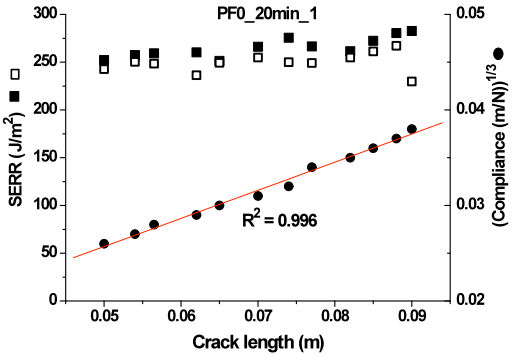

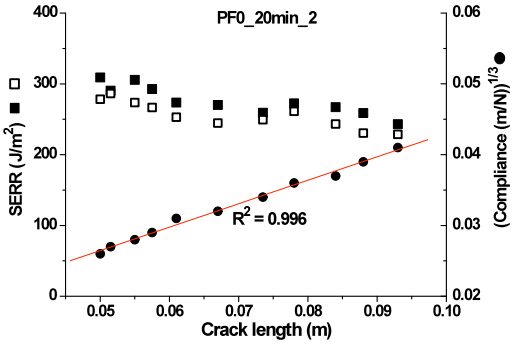

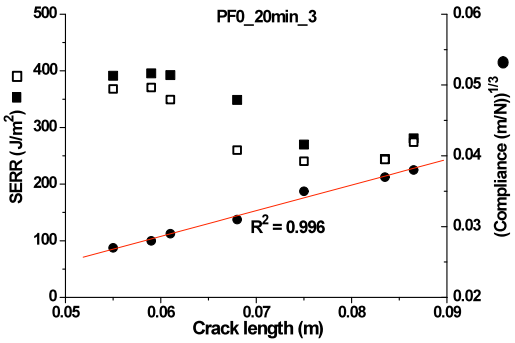

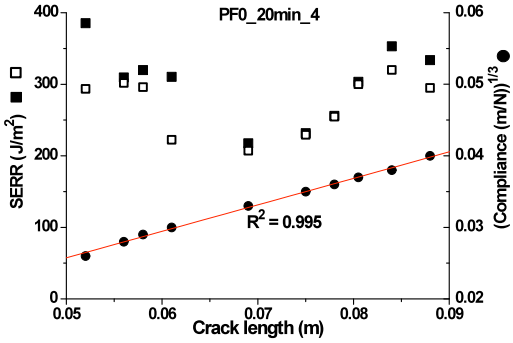

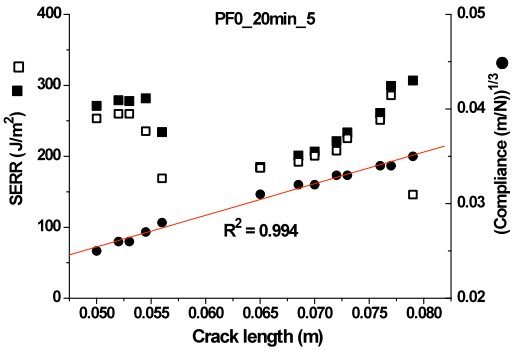

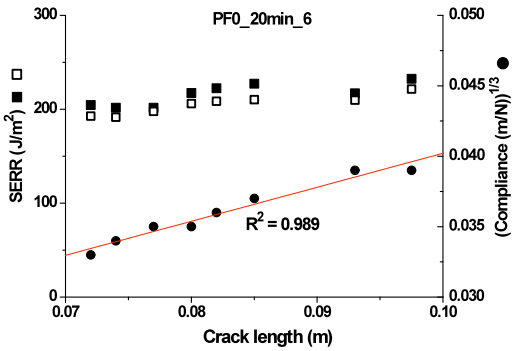

6.7.1.5. PF1 – 8 min

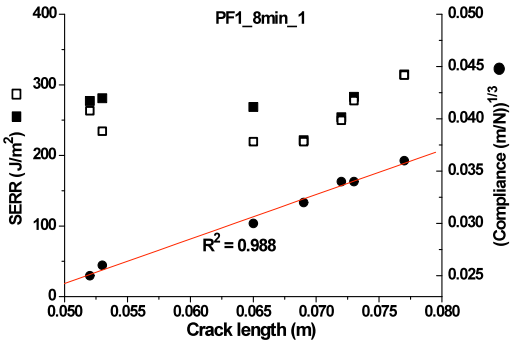

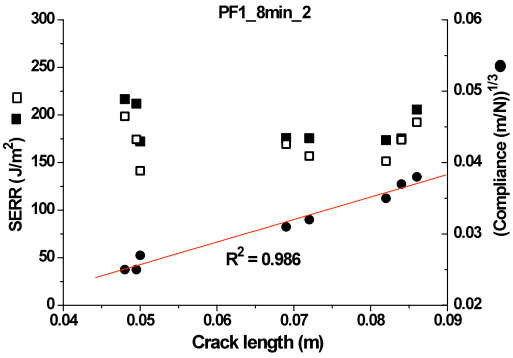

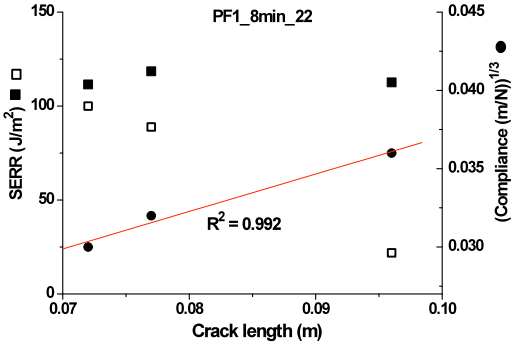

6.7.1.6. PF0 – 10 min

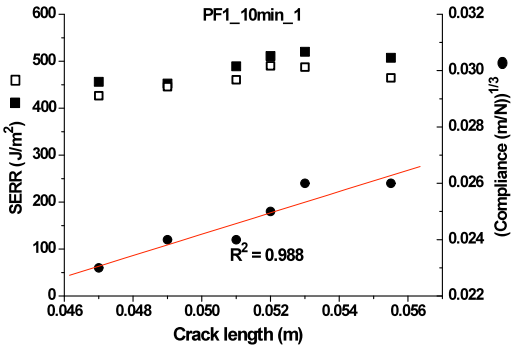

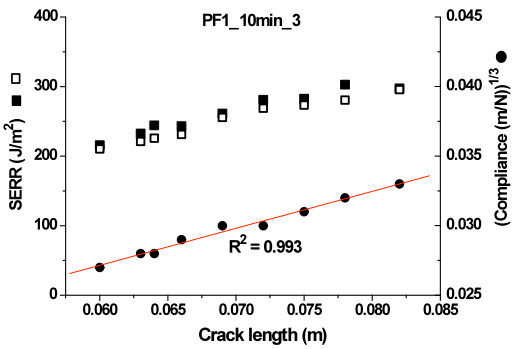

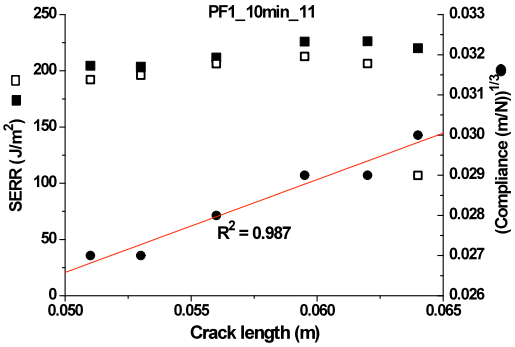
PF1_10min_11
SERR (J/m²)
(Compliance (m/N))^1/3
Crack length (m)
R² = 0.987

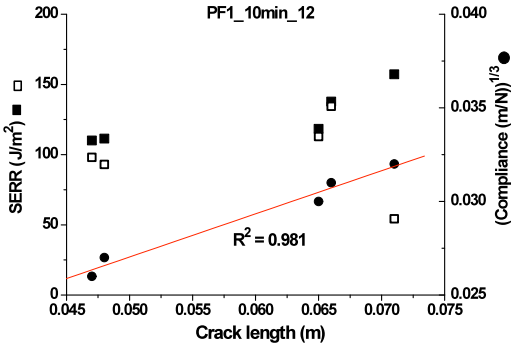
PF1_10min_12
SERR (J/m²)
(Compliance (m/N))^1/3
Crack length (m)
R² = 0.981

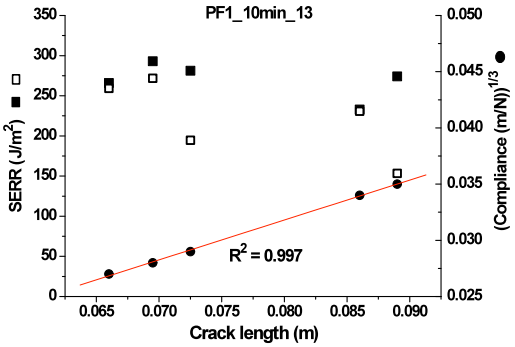
PF1_10min_13
SERR (J/m²)
(Compliance (m/N))^1/3
Crack length (m)
R² = 0.997

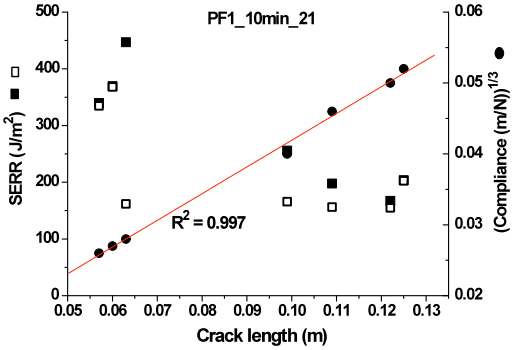
PF1_10min_21
SERR (J/m²)
(Compliance (m/N))^1/3
Crack length (m)
R² = 0.997

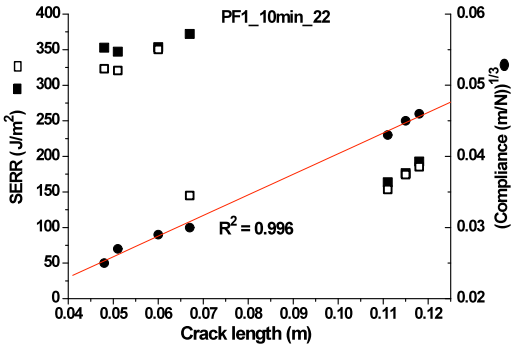
PF1_10min_22
SERR (J/m²)
(Compliance (m/N))^1/3
Crack length (m)
R² = 0.996

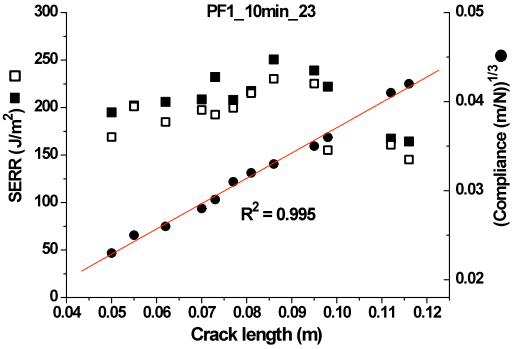
PF1_10min_23
SERR (J/m²)
(Compliance (m/N))^1/3
Crack length (m)
R² = 0.995

6.7.1.7. PF2 – 8 min

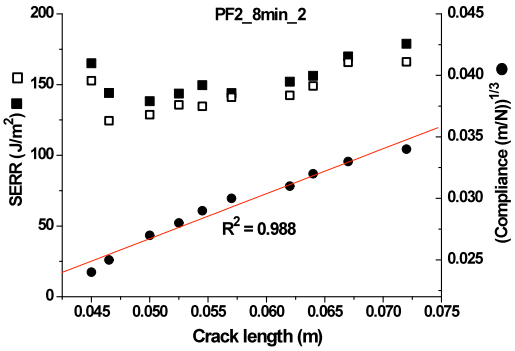

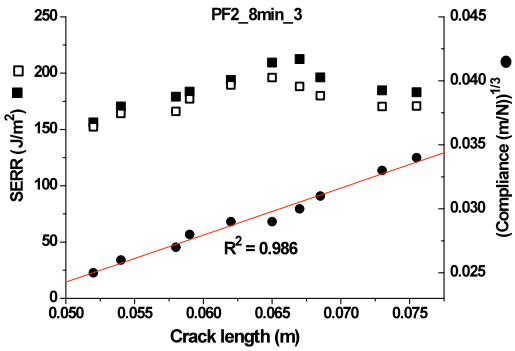

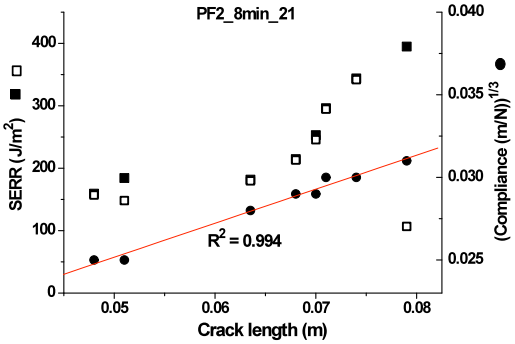

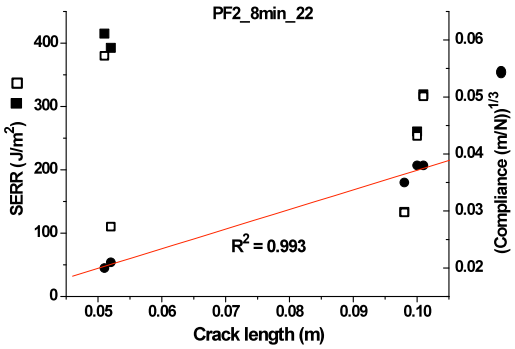

6.7.1.8. PF2 – 10 min

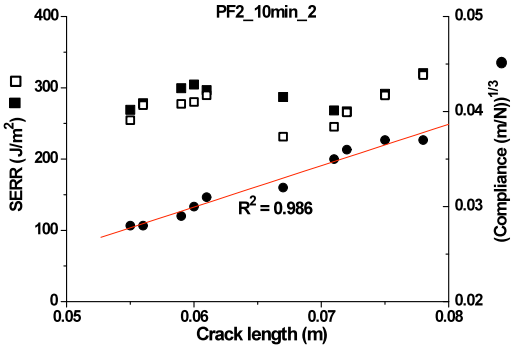

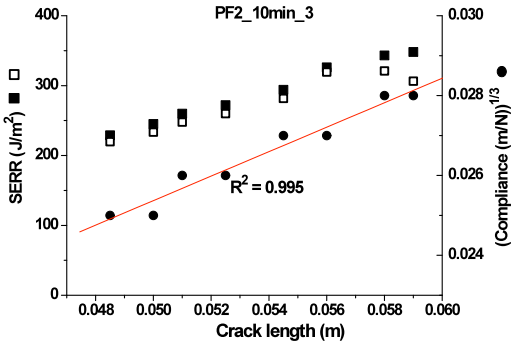

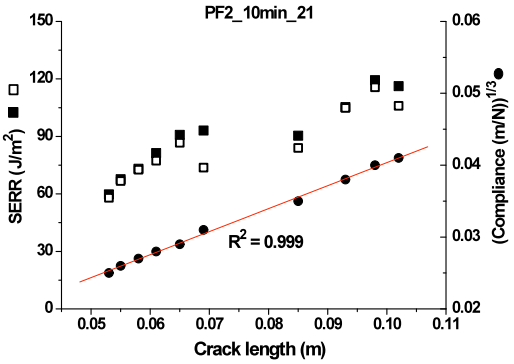

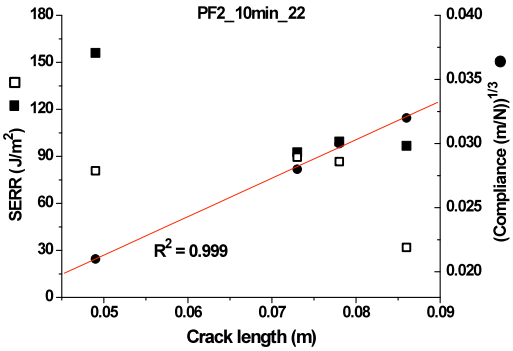

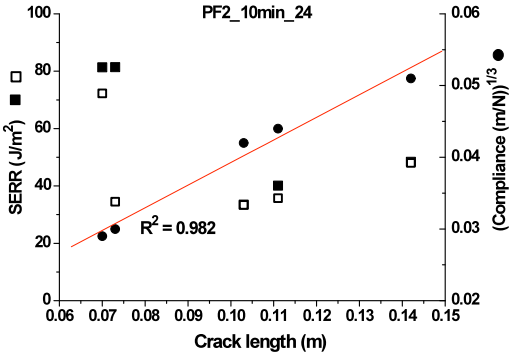

6.7.1.9. PF3 – 8 min

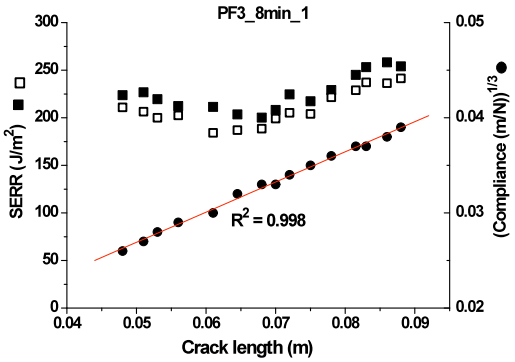

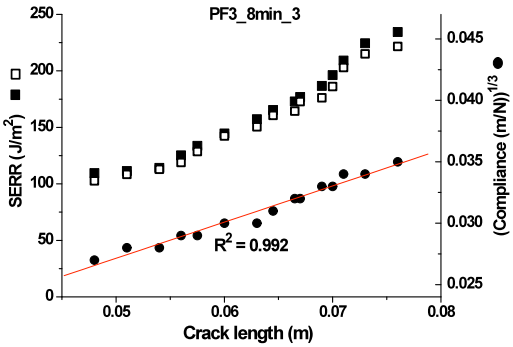

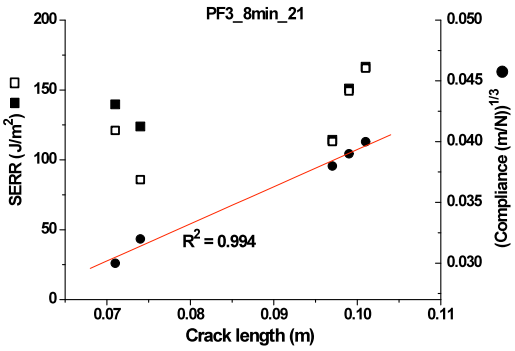

6.7.1.10. PF3 – 10 min

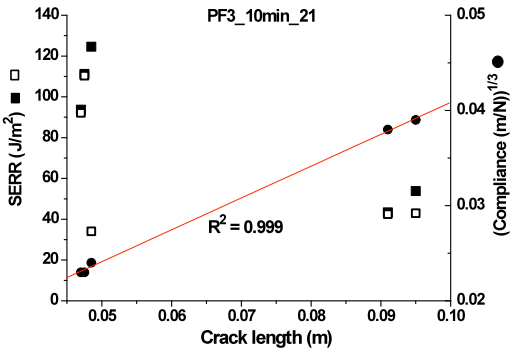

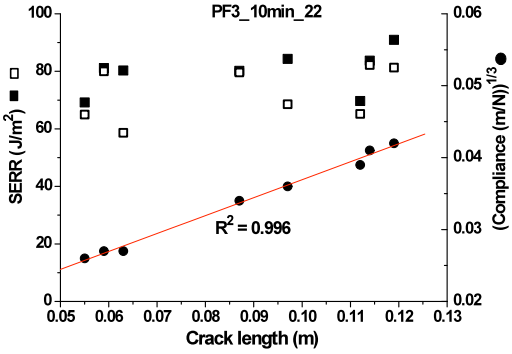

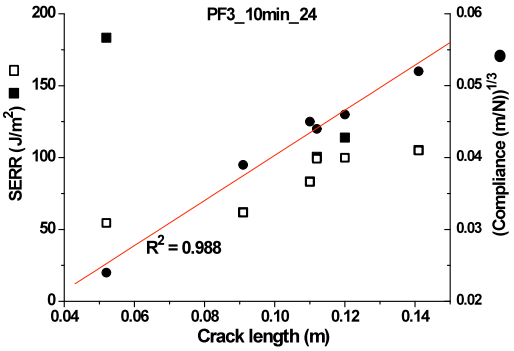

6.7.2. Results of the Mann–Whitney U significance test

Table 6.4. p-Values for the comparisons of critical SERR (G_{Ic}) values between two groups based on the Mann-Whitney U test in SPSS

Resin		PF0				PF1		PF2		PF3	
	Press time	8 min	10 min	15 min	20 min	8 min	10 min	8 min	10 min	8 min	10 min
PF0	8 min	•	0. 238	0.286	0.000	0.000	0.000	0.000	0.000	0.000	0.000
	10 min	0.238	•	0.000	0.000	0.000	0.000	0.000	0.000	0.000	0.000
	15 min	0.286	0.000	•	0.000	0.000	0.000	0.000	0.000	0.000	0.000
	20 min	0.000	0.000	0.000	•	0.001	0.036	0.000	0.002	0.000	0.000
PF1	8 min	0.000	0.000	0.000	0.001	•	0.074	0.622	0.420	0.260	0.000
	10 min	0.000	0.000	0.000	0.036	0.074	•	0.002	0.010	0.000	0.000
PF2	8 min	0.000	0.000	0.000	0.000	0.622	0.002	•	0.194	0.727	0.000
	10 min	0.000	0.000	0.000	0.002	0.420	0.010	0.194	•	0.915	0.004
PF3	8 min	0.000	0.000	0.000	0.000	0.260	0.000	0.727	0.915	•	0.000
	10 min	0.000	0.000	0.000	0.000	0.000	0.000	0.000	0.004	0.000	•

CHAPTER 7

CONCLUSIONS

The conclusions that can be drawn from this research are:

1. Addition of CNCs changes the flow behavior of PF resins from Newtonian to shear-thinning and causes a strong increase in low-shear-rate viscosity;
2. CNCs accelerate the first stage of resin cure, possibly being the condensation of methylolureas, but have a lesser or potentially no effect on the second stage of resin cure, possibly involving methylolphenol and methylolurea condensation and methylolation, and perhaps the formation of hemiformals through reaction of released formaldehyde with cellulose hydroxyl groups;
3. CNCs accelerate the incipient and relative storage modulus increase and cause an increase in ultimate sample stiffness through mechanical reinforcement of the resin by the CNCs;
4. At high enough CNC contents, CNCs lower the vitrification point, resulting in reduced ultimate sample stiffness, possibly due to premature quenching of the curing reactions, leading to lower crosslinking densities.
5. CNCs diminish the fracture energy of PF resins and cause voids in the bondline;
6. The detrimental effect of CNCs on the fracture energy may be due to an acceleration of resin cure and depression of the vitrification point by the CNCs;

7. The detrimental effect of CNCs on bondline quality may be due to the increasing effect of CNCs on resin viscosity.